Structural and Magnetic Characterisation of Heusler Alloy Thin Films under Optimised Growth Condition for Spintronic Devices

Wu Haokaifeng

DOCTOR OF PHILOSOPHY

UNIVERSITY OF YORK

PHYSICS

APRIL 2018

Abstract

Spintronic devices have been playing an important role in magnetic storage and memory applications for the last 20 years. For such a trend to continue, it is critical to develop new magnetic materials, in particular, in the context of antiferromagnetic spintronics, materials with high Curie temperatures, large spin polarisations, and low saturation magnetisations. In this study, three Heusler alloys, Mn_2VSi, Mn_3Ga and Mn_3Ge have been investigated and experimental results have been carried out.

80 nm thick polycrystalline Mn_2VSi films have been deposited on silicon substrates with an 18 nm silver seed layer and a 3 nm aluminium capping layer using a sputtering system. The best quality film is obtained for 723 K growth. The Mn_2VSi thin film is verified to be antiferromagnetic, where an exchange bias is found when a 3 nm ferromagnetic CoFe layer has been deposited on the top of the Mn_2VSi layer. The exchange bias is measured to be 34 Oe at 100 K. The blocking and thermal activation temperature of Mn_2VSi is estimated to be below 100 K and within a range between 100 K and 448 K, respectively.

Polycrystalline Mn_3Ga layers with thickness in the range from 3-20 nm were deposited at room temperature. To investigate the onset of exchange-bias, a ferromagnetic $Co_{0.6}Fe_{0.4}$ layer (3.3-9 nm thick) capped with 5 nm Ta, were subsequently deposited. X-ray diffraction measurements confirm the presence of Mn_3Ga (0002) and (0004) peaks characteristic of the $D0_{19}$ antiferromagnetic structure. The 6 nm thick Mn_3Ga film shows the largest exchange bias of 430 Oe at 120 K with a blocking temperature of 225 K. The blocking temperature is found to decrease with increasing Mn_3Ga thickness. These results in combination with X-ray reflectivity measurements confirm that the quality of the $Mn_3Ga/Co_{0.6}Fe_{0.4}$ interface controls the exchange bias, with the sharp interface with the 6-nm-thick Mn_3Ga inducing the largest exchange bias. The magneto-crystalline anisotropy for 6 nm thick Mn_3Ga thin film sample is calculated to be $9 \times 10^4 J/m^3$.

Polycrystalline Mn_3Ge samples with same stack layer structure as Mn_3Ga films were also studied. A growth temperature of 773 K promotes the crystallisation of the 100 nm thick Mn_3Ge layer showing a $D0_{19}$ antiferromagnetic structure. The exchange bias cannot be observed due to the potential interlayer diffusion during high temperature sputtering.

Contents

Abstract 2

Contents 3

List of Figures 7

List of Table 12

Acknowledgement 13

Declaration 14

Chapter 1 15

Introduction 15

1.1 Units and Errors 17

Chapter 2 18

Spintronic Devices and Magnetoresistance 18

2.1 Magnetoresistance 18

2.1.1 Giant Magnetoresistance 19

2.1.2 Applications of GMR 23

2.2 Current Induced Magnetisation Switching 24

2.3 Tunnelling Magnetoresistance 25

2.4 Magnetic Random Access Memory 29

Chapter 3 32

Heusler Alloy 32

3.1 Heusler Alloy Structure 33

3.2 Slater-Pauling Behaviour of the Heusler alloys 36

3.3 Antiferromagnetic Heusler Alloys 38

3.4 Mn2VSi 42

3.5 Mn3Ga 45

3.6 Mn3Ge 48

Chapter 4 49

Magnetic Properties in Thin Films 49

4.1 Magnetic Anisotropy 49

4.1.1 Magnetocrystalline Anisotropy 50

4.1.2 Exchange Anisotropy 53

4.1.3 Texture in Polycrystalline Antiferromagnetic Films 55

4.2 Domain Structures in Thin Films 55

4.3 Stoner-Wohlfarth Theory 58

4.4 Exchange Interaction in Thin Films 60

4.4.1 Direct Exchange 61

4.4.2 Indirect Exchange 63

4.4.3 Superexchange 64

Chapter 5 65

Exchange Bias 65

5.1 Theories and Models of Exchange Bias 65

5.1.1 Meiklejohn-Bean Model 66

5.1.2 Néel's Antiferromagnetic Domain Wall 67

5.1.3 Fulcomer-Charap Model 68

5.2 The York Model of Exchange Bias 69

5.2.1 Energy Barriers 69

5.2.2 Time Dependence 71

5.2.3 The Setting Process 72

5.2.4 Grain Volume Distribution 73

5.2.5 The Blocking Temperature 75

5.2.6 The Anisotropy Constant 78

5.2.7 Grain Volume and Film Thickness Dependence 78

Chapter 6 81

Experimental Techniques 81

6.1 Thin Film Deposition 81

6.1.1 High Target Utilisation Sputtering (HiTUS) 82

6.1.2 Sample Preparation 86

6.2 Sample Structural Characterisation 87

6.2.1 X-ray Diffractometer 88

6.2.2 Pole Figure Measurement 90

6.2.3 Reflectivity Measurement 91

6.2.4 Scherrer Analysis 92

6.2.5 Transmission Electron Microscopy 93

6.2.6 Grain Size Analysis 96

6.2.7 Scanning Electron Microscopy 98

6.3 Magnetic Characterisation Methods 100

6.3.1 Vibrating Sample Magnetometer (VSM) 100

6.3.2 Thermal Activation Measurements 103

6.3.3 Training Effect 105

6.3.4 XMCD Introduction 105

6.3.5 Method of XMCD Analysis 107

Chapter 7 109

Antiferromagnetic and Ferrimagnetic materials for spintronic devices 109

7.1 Chemical Analysis of Polycrystalline Heusler Alloys 109

7.2 Structural Characterisation of Polycrystalline Mn2VSi 110

7.3 Magnetic Characterisation of Polycrystalline Mn2VSi 114

7.4 Structural Characterisation of Polycrystalline Mn3Ga 120

7.5 Magnetic Characterisation of Polycrystalline Mn3Ga 127

7.6 Structural Characterisation of Polycrystalline Mn3Ge 140
7.7 Magnetic Characterisation of Polycrystalline Mn3Ge 143
Chapter 8 147
8.1 Conclusion 147
8.2 Future Work 148
Acronyms 150
List of Symbol 152
Reference 156

List of Figures

Figure 1.1 Recent iridium price in USD/g [135]. 16

Figure 2.1 Schematic diagram if a GMR stack and resistor network [9]. 19
Figure 2.2 Schematic diagram of current in the plane (CIP) and current perpendicular to the plane (CPP) GMR stack [110]. 21
Figure 2.3 A schematic diagram of perpendicular recording media [136]. 23
Figure 2.4 A schematic diagram of quantum tunnelling. 26
Figure 2.5 A schematic of magnetisation in the TMR effect related to the Fermi Energy (E_F) [137]..... 26
Figure 2.6 A schematic diagram of conventional MRAM cell and spin transfer torque (STT) RAM cell. 30

Figure 3.1 Periodic table of the elements. The large number of Heusler materials can be formed by combining different elements according to the colour scheme [37]. .. 32
Figure 3.2 Overview of the most common types of structure in the Heusler compounds [37]. 35
Figure 3.3 Calculated total spin-moment per unit cell as a function of the total number Z_t of valence electrons per unit cell for all the studied half-Heusler alloys. The dashed line represents the Slater-Pauling behaviour [46]. 37
Figure 3.4 Calculated total spin-moment per unit cell as a function of the total number (Z_t) of valence electrons per unit cell for all the studied full-Heusler alloys. The dashed line represents the Slater-Pauling behaviour [138]. 38
Figure 3.5 Schematic representation of the DOS for a half-metal with respect to normal metals and semiconductors [46]. 39
Figure 3.6 Schematic images for Heusler alloys with bcc structure[60]. 42
Figure 3.7 (a) Hysteresis loop of Ni_2MnAl film deposited at different temperatures. (b) Hysteresis loops of Ni_2MnAl/Ni_2MnGe bilayer sample and Ni_2MnGe thin film measured at 10 K [61]. 44
Figure 3.8 (a) Schematic crystal structure $D0_{19}$ hexagonal antiferromagnetic Mn_3Ga [67], and (b) $D0_{22}$ tetragonal ferrimagnetic Mn_3Ga [76]..... 46
Figure 3.9 XRD scan of the hexagonal Mn_3Ge powder at room temperature [79]. . 48

Figure 4.1 Prolate ellipsoid with semi-major axis *c* and semi-minor axis *a*. 49
Figure 4.2 Three principle crystallographic directions in the (110) plane of a cubic crystal [133]. 50
Figure 4.3 *M-H* curve for single crystals of iron (a) and nickel (b) [133] 51
Figure 4.4 *M-H* curve for single crystals of cobalt. 52
Figure 4.5 *M-H* curve of Co/CoO segregated particles measured at 77 K. Loop (1) field-cooled measurement. Loop (2) cooled in zero field [52]. 53
Figure 4.6 Classic model of exchange bias [52]. 54
Figure 4.7 A schematic diagram of 180° domain wall. 56
Figure 4.8 (a) Domain formation in a saturated magnetic field of the single domain state. (b) 180° domain wall formed to split single domain into two with opposite direction. (c) 90° closure domain wall formation leads to eliminate the Ems. 56
Figure 4.9 Ellipsoid single domain particle with the c axis as the easy direction. ... 58
Figure 4.10 Hysteresis loop for single domain particles with uniaxial anisotropy. h is the normalised field H/Hk[133]. 60
Figure 4.11 Antiparallel alignment of spins 62
Figure 4.12 Parallel alignment of spins 62
Figure 4.13 Bethe-Slater curve[133] 62
Figure 4.14 Variation of the indirect exchange coupling constant *j* of a free electron gas in the neighbourhood of a point magnetic moment at the origin r=0 [139]. 63
Figure 4.15 Superexchange interaction between transition metals and oxides or nitrides. 64

Figure 5.1 Meiklejohn-Bean model for exchange bias [140]. 67
Figure 5.2 Time dependence of the exchange field with ln(t) [98]. 72
Figure 5.3 Experimental and calculated magnetic viscosity as a function of T_{set} [98]. 73
Figure 5.4 Schematic diagram of the AF grain volume distribution with critical volume V_c and V_{set} [98]. 74
Figure 5. 5 Grain size distribution for a 6-nm thick Mn_3Ga thin film sample. 75
Figure 5.6 Temperature dependence of exchange bias measured for the Mn_3Ga (6 nm)/$Co_{0.6}Fe_{0.4}$ (3.3 nm) films 77

Figure 5.7 Variation of exchange bias with AF thickness [105]. 79
Figure 5.9 Grain volume distribution for varying thicknesses of IrMn [105]. 80
Figure 5.8 Variation of the exchange bias with antiferromagnetic grain diameter [105]. 80

Figure 6. 1 Schematic diagram of the HiTUS system [108]. 83
Figure 6.2 Schematic diagram of heater inside the chamber. 85
Figure 6.3 Ceramic substrate holder used in HiTUS for deposition. 86
Figure 6.4 Schematic diagram of X-ray Bragg diffraction. 88
Figure 6.5 The Rigaku SmartLab X-ray diffractometer [128]. 89
Figure 6.6 Schematic diagram of scintillating counter detector [141]. 90
Figure 6.7 An example of a reflectivity scan of Mn_3Ga/CoFe multi-layer thin film. 92
Figure 6.8 Schematic diagram of transmission electron microscope. 94
Figure 6.9 Schematic ray diagram of Bright field and dark field operation. 95
Figure 6.10 Bright field image of Mn_3Ga thin film. 95
Figure 6. 11 Zeiss particle analyser. 96
Figure 6.12 Schematic diagram of the A JEOL JSM-5910LV scanning electron microscope (SEM). 98
Figure 6.13 Schematic of a Vibrating Sample Magnetometer. 101
Figure 6. 14 Hysteresis loop measurement [121] 102
Figure 6.15 Schematic diagram of measurements procedures of the York Protocol [14]. 103
Figure 6.16 Schematic diagram of AF grain size distribution [14]. 104
Figure 6.17 Band illustrations of (a) a non-magnetic material and (b) a magnetic material with an external field. 106
Figure 6.18 The sum rule constant, *p*, *q*, and *r* which correspond to the integral of the dichroism spectra for the L_3 edge, the integral of the dichroism spectra over both the L_3 and L_2 edges and the area of the summed XAS signal after removal of a stepped background respectively [126]. 108

Figure 7. 1 Schematic diagram of Mn_2VSi films deposited 111

Figure 7.2 XRD scans for (a) 80 nm Mn_2VSi samples grown at elevating temperatures, (b) 80 nm Mn_2VSi samples post-annealed at elevating temperatures and (c) different thickness of Mn_2VSi samples grown at 723 K. 112
Figure 7.3 X-ray reflectivity scans for Mn_2VSi/CoFe films grown at 723 K and post-annealed at 723 K. 113
Figure 7.4 Hysteresis loop for Mn_2VSi/CoFe (in black) and Mn_2VSi/CoFeSi (in red) measured at 100 K. 115
Figure 7. 5 Magnetisation curve for polycrystalline Cr (3 nm)/Ag (15 nm)/Mn_2VSi (80 nm)/Al (3 nm) films measured at room temperature. 116
Figure 7.6 Hysteresis loops of Mn_2VSi/ CoFe (3 nm) layers with different Mn_2VSi layer thicknesses grown at 723 K. 117
Figure 7.7 Magnetisation curves for the 80-nm-thick $Mn_2VSi/Co_{0.6}Fe_{0.4}$ film for different activation temperatures between 103 K and 448 K. 118
Figure 7. 8 (a)XRD spectra for the 20 nm Mn_3Ga samples deposited under different bias voltage. (b) XRD spectra for the 20 nm Mn_3Ga samples deposited under different growth temperature. 120
Figure 7.9 (a) projection of $D0_{19}$ hexagonal Mn_3Ga along (0001) plane, (b) schematic diagram of Mn_3Ga unit cell, (c) schematic diagram of cubic Pt along (111) plane and (d) schematic diagram of the Mn_3Ga film deposited. 121
Figure 7.10 (a) 16×16 mm2samples measured using Ge(220)×2 crystalsmonochromater. (b) 5×5 mm2samples measured without Ge(220)×2 crystalsmonochromater. 123
Figure 7.11 (a) XRD spectra for the Mn_3Ga samples with different thicknesses (CoFe thickness of 3.3 nm). (b) XRD intensities around the (0001) line. (c) Pole figure scan at 41.45^o for the 20-nm-thick Mn_3Ga film. 125
Figure 7.12 XRR scan for 6-nm-thick Mn_3Ga/3.3-nm-thick CoFe film. 126
Figure 7.13 (a) Plan-view TEM image for grain size analysis for 6 nm thick Mn_3Ga thin film sample. (b) Grain size distribution for 6 nm thick Mn_3Ga thin film sample. 127
Figure 7.14 Magnetisation curve for polycrystalline Mn_3Ga (20 nm)/Pt (5 nm) films measured at room temperature. 127
Figure 7.15 Magnetisation curves for the polycrystalline Mn_3Ga (6 nm)/$Co_{0.6}Fe_{0.4}$ (3.3 nm) films (red line), Mn_3Ga (6 nm)/Co (3.3 nm) films (black line) measured at 120 K. 128

Figure 7.16 (a) Magnetisation curves for the polycrystalline $Mn_3Ga/Co_{0.6}Fe_{0.4}$(3.3 nm) films versus Mn_3Ga thicknesses of 6 (blue line), 10 (red line) and 20 nm (black line) measured at 120 K. (b) Magnetisation curves for the polycrystalline Mn_3Ga (6 nm)/$Co_{0.6}Fe_{0.4}$ films CoFe thicknesses of 3.3 (black line), 6 (red line) and 9 nm (blue line) measured at 120 K. 129
Figure 7.17 Magnetisation curves for the 6-nm-thick $Mn_3Ga/Co_{0.6}Fe_{0.4}$ film for different activation temperatures between 100 K and 350 K. 132
Figure 7.18 Magnetisation curves for the (a) 10-nm-thick and (b) 20-nm-thick $Mn_3Ga/Co_{0.6}Fe_{0.4}$ film for different activation temperatures between 100 K and 300 K. (c) 10-nm thick $Mn_3Ga/Co_{0.6}Fe_{0.4}$ film after cleaning in acetone for 30 minutes and measured with activation temperature set to be 125 K. 133
Figure 7.19 Temperature dependence of exchange bias determined for the $Mn_3Ga/Co_{0.6}Fe_{0.4}$ films with the Mn_3Ga thickness of 6, 10 and 20 nm. 134
Figure 7.20 Magnetic contrast image of Mn_3Ga (6 nm)/CoFe (2 nm)/Al (2nm) sample taken at the Co edge and Mn edge at 150 K. 136
Figure 7.21 (a) and (b) XAS and (c) and (d) XMCD spectra of the Co and Mn edges in Mn_3Ga (6 nm)/CoFe (2 nm) sample, respectively. The corresponding XMCD images of (e) Co L3 and (f) Mn L3 edges. 137
Figure 7.22 XMCD spectra of the (a) Co and (b) Mn edges in Mn_3Ga (6 nm)/CoFe (2 nm) sample, respectively. 139
Figure 7.23 XRD spectra for the Mn_3Ge samples with different AF thicknesses. . 142
Figure 7.24 XRD spectra for Sample A: Ta (5 nm)/Pt (35 nm)/Mn_3Ge (100 nm)/Ta (5 nm) film grown at 500℃. Sample B: only 100-nm-thick Mn_3Ge layer grown at 500℃ 142
Figure 7.25 Magnetisation curve for polycrystalline Mn_3Ge (100 nm)/Ta (5 nm) films measured at room temperature 143
Figure 7.27 Magnetisation curves for the polycrystalline Mn_3Ge (100 nm)/$Co_{0.6}Fe_{0.4}$ (3.3 nm) film measured at 100 K. 145
Figure 7.26 Magnetisation curves for the polycrystalline $Mn_3Ge/Co_{0.6}Fe_{0.4}$ (3.3 nm) with various AF thickness from 6 nm to 40 nm grown at room temperature measured at 100 K. 145

List of Table

Table 3.1 Fermi-level spin polarisation and resistivity of Mn-Ga films measured by point contact Andreev reflection [76][77]..... 47

Table 6.1 Heater temperature fluctuation measurements. 85

Table 7.1 Results of the chemical analysis performed by JEOL JSM-5910LV scanning electron microscope..... 110
Table 7.2 List of Mn_2VSi(220) peak with different post annealed temperature..... 113
Table 7.3 Comparison between the $D0_{19}$ and $D0_{22}$ phases of Mn_3Ga. 125
Table 7.4 Value of exchange bias with different layer thickness. 131
Table 7.5 Orbital moments, spin moments and total moment of the Co and Mn from $Mn_3Ga/Co_{0.6}Fe_{0.4}$ bilayer samples in units of μB/atom. 139
Table 7.6 Comparison between the $D0_{19}$ and $D0_{22}$ phases of Mn_3Ge. 140
Table 7.7 List of FWHM for Mn_3Ge peaks. 143
Table 7.8 List of samples growth plan for future work. 146

Acknowledgement

This thesis and the work during my PhD would never have been possible without the help and guidance from my supervisors Prof. Atsufumi Hirohata and Dr. Gonzalo Vallejo Fernandez.

I would also like to thank Prof. Kevin O'Grady who offered me an opportunity to start my PhD study and supported me throughout my study.

I must also thank all my colleagues, Ioan, Teo, Kelvin, Will, John, Joe and Ed who have made the last three years so enjoyable.

Most importantly, I would like to thank my dear parents and Yao Huang. You are the reason that keep me motivated throughout the difficult time.

In the end, I would like to thank my grandfather in heaven. I hope you would be proud of me.

Declaration

I declare that this thesis is a presentation of original work and I am the sole author. This work has not previously been presented for an award at this, or any other, University. All sources are acknowledged as References.

Chapter 1

Introduction

The purpose of this research is to design a replacement for IrMn, an exchange-biasing material characterised by elevated thermal stability and high resistance to corrosion. At present, IrMn is a widely-used antiferromagnetic alloy applied in a variety of electronic devices (e.g., hard disk drives [HDDs] and magnetic random access memory [MRAM]). The desired material that will replace IrMn is an antiferromagnetic (AF) Heusler alloy (HA) thin film.

Since iridium (Ir), which constitutes the densest element after osmium (Os), is characterised by stability and a high melting point (higher than 3,000°C), it is commonly found in meteorites and asteroids. However, it is among the rarest elements in the Earth's crust, and it is retrieved much less commonly than many materials often regarded as rarer. Approximately 5.8 tonnes of Ir are retrieved from the Earth's crust annually, the majority of which (87%) derives from South Africa [1]. As a member of the platinum-group of metals, Ir can be produced as a side product of platinum and palladium ores, the standard concentration being between 1% and 2% [1]. It is also noteworthy that Ir constitutes a side product of the electro-refining process of nickel and copper. At present, estimates suggest that Ir prevalence within the Earth's crust is $4x10^{-4}$ ppm, which is a conspicuously lower value when compared to other important metals, including asneodymium (33 ppm), lithium (17 ppm), dysprosium (6.2 ppm), platinum ($3.7x10^{-3}$ ppm), gold ($3.1x10^{-3}$ ppm), ruthenium ($1x10^{-3}$ ppm), and palladium ($6.3x10^{-4}$ ppm). This demonstrates that Ir prevalence in the Earth's crust is the lowest of all metals [2]. This fact was not concerning until relatively recently, and more specifically, until the discovery of GMR and TMR, since no commercial applications of the metal were extant. However, given these discoveries, and the utilisation of Ir in HDDs, demand for the metal rose four times in the period from 2009 to 2011 (to reach approximately 9.5 tonnes) [2].

In view of the least abundant status of Ir, IrMn, although a suitable material for a variety of electronic applications, is costly, with its price having risen by a factor of 4 over the recent half-decade (and for the recent decade, by a factor of 10), as shown in Fig 1.1.

Figure 1.1 Recent iridium price in USD/g [139].

Given the fact that an even greater number of modern technologies are now anticipated to draw on IrMn, this price increase is set to become even more pronounced. In view of this, Heusler alloys (HAs), which are alloys of the transition metals (e.g., iron [Fe], cobalt [Co], or manganese [Mn]) with materials like silicon (Si) or aluminium (Al), are now being focused on by many researchers. If HAs could be utilised for similar applications to those that IrMn is currently used in, costing and availability problems would be alleviated significantly. At present, the literature indicates that spintronic technologies will constitute the foundation of the future's electronic devices rather than contemporary society's volatile semiconductors, and it is notable that the read heads within HDDs are already constituted in this novel way. As such, it is clear that procurement issues surrounding IrMn have prompted scientists and researchers to explore new possibilities.

Given the criticality of Ir in the HDD industry for the recent ten years, a comprehensive analysis of the binary alloys that could be used instead has been conducted. Although PtMn was identified as a viable candidate in a variety of respects, the prohibitive nature of its elevated temperature anneal (temperatures of around 1,000°C are necessary to facilitate the conversion from the face centered cubic (fcc)

phase to the face centered tetragonal (fct) phase in bulk form) presents difficulties in the context of thin film form. As such, ternary alloys must be addressed to identify antiferromagnetic (AF) or compensated ferrimagnetic (CF) materials characterised by appropriate thermal stability values.

This study's objective is to identify a new material that can substitute for Ir, thereby lowering the expense associated with AF films by 10 times when comparatively examined against IrMn. In the research, the films were characterised in structural and magnetic ways by employing transmission electron microscopy (TEM), X-ray diffraction, and magnetic measurements. It is necessary for the device to exhibit an exchange bias, namely, the impact of a hysteresis loop shift facilitated by AF-ferromagnet coupling greater than 1 kOe in thin film form, with a blocking temperature exceeding 300K. If so, then it will be compatible with industry standards for HDD read heads. The following HAs are examined: Mn_2VSi, Mn_3Ga and Mn_3Ge.

1.1 Units and Errors

The application of c.g.s unit system has been utilised in this study as it is the standard system used in the magnetic recording industry. The c.g.s system is commonly used by the major magnetism community.

The errors on results presented in this study were calculated using the standard Gaussian error method.

Chapter 2

Spintronic Devices and Magnetoresistance

In recent years, primarily owing to the discovery of giant magnetoresistance (GMR), researchers and commercial stakeholders have been paying increasingly close attention to spin electronics. All commercially available hard disk drives (HDDs) contain magnetoresistive sensors within their read heads, and such sensors are also employed for all applications which require the accurate determination of a magnetic state. Further advances have resulted in the incorporation of spintronics into other applications, including magnetic random access memory (MRAM), the purpose of which is to substitute for the technology related to the current transistor. When a device is not powered on, a stable logic state can be achieved from strides forward in the manipulation of spin as opposed to electron charge, but novel properties are required for those materials which would implement these processes. Owing to their inferior spin polarisation capacities, which lead to impaired spin injection efficiency (typically less than 50%), conventional transition metal ferromagnets are unsuitable for spin manipulation. Contrastingly, existing materials could be replaced by half-metallic Heusler compounds and alloys, since these are associated with significantly higher spin polarisation (estimates suggest this can reach 100%). Noteworthy, Heusler alloys provide a wide range of materials with tuneable transport and magnetic properties, many of which are precisely what new data storage technologies require.

2.1 Magnetoresistance

Thomson [3], after documenting the relationship between electrical current and conductor magnetisation, was responsible for discovering the concept of magnetoresistance in 1856. Owing to the Hall Effect, ordinary magnetoresistance occurs in magnetic and non-magnetic materials. With respect to ferromagnetic materials, magnetoresistance is impacted by the material's intrinsic anisotropy, which gives rise to anisotropic magnetoresistance (AMR). Here, the process relies on the applied magnetic field direction, and it can be accounted for by spin-orbit coupling inside the ferromagnetic material [4]. In the context of AMR, if the charge current is parallel or normal to the atomic magnetic moments (which themselves are oriented via an applied magnetic field), the electron spin-orbit coupling promotes variability in the

scattering cross section. The effect is significant, but the scale of the change in resistance is negligible, which impairs the precision with which potential magnetisation states can be distinguished.

2.1.1 Giant Magnetoresistance

Grünberg and Fert received the Nobel Prize for documenting the giant magnetoresistance (GMR) effect in 2007. The GMR effect is reliant upon spin dependent scattering (SDS) of the current carrying electrons in the host materials. SDS occurs in transition metals due to the number of unoccupied states in the *d* bands. It was first examined for bulk ferromagnetic materials towards the end of the 1980s [5]. By employing the two current model, which holds that it is possible to separate the current moving through a transition metal into a pair of channels, Mott [6] initially documented the phenomenon in 1936. As a consequence of this early research, Fert and Campbell could conduct their investigation into SDS in the latter part of the twentieth century, the results of which conformed to the existing experimental findings [7][8].

A GMR structure is intentionally engineered so as to facilitate the exploitation of the SDS, and it can be accounted for by drawing the resistor diagram below.

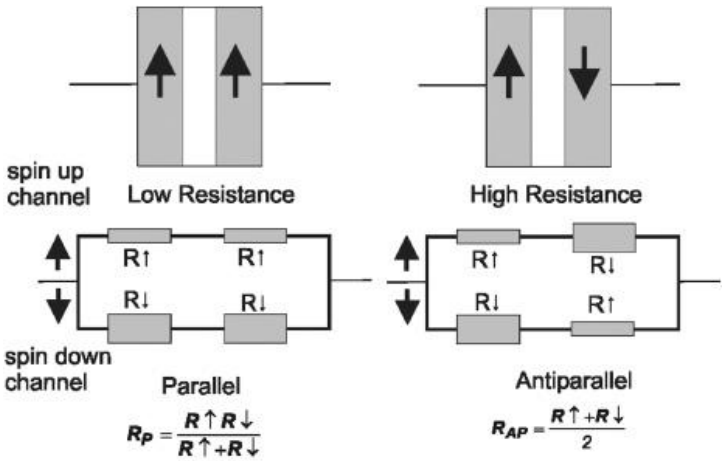

Figure 2.1 Schematic diagram of a GMR stack and resistor network [9].

Regarding the two current model or independent spin up and spin down electron transport channels, it is possible for the ferromagnetic layers to serve as resistors in a parallel configuration for the paths of the spin channels. As it shown in Fig 2.1, when the magnetisation direction of F layers are parallel (pointing upwards), the spin-down electrons are scattered back leaving for a low resistance in the path of spin-up electrons. Contrastingly when F layers are antiparallel, both spin-up and spin-down electrons exhibiting high resistance through the structure. In view of this, the evidence indicates that the sole mechanism that can be utilised to distinguish between the low and high resistance states of the GMR stack is to switch the magnetisation of the two magnetic layers from the parallel state (R_P, low resistance) to the antiparallel state (R_{AP}, high resistance). As documented by M. T. Sarah *et al* [9], this is reflected in the following equation:

$$\frac{\Delta R}{R} = \frac{R_{AP} - R_P}{R_P} = \frac{(R\downarrow - R\uparrow)^2}{4R\downarrow R\uparrow} \tag{2-1}$$

Although the GMR mechanism does not seem to be complex, a comprehensive investigation of electron scattering dynamics draws attention to several limiting aspects of the magnetoresistance effect. In statistical terms, the electron scattering process can be characterised as either elastic or inelastic, and it can potentially give rise to spin flipping [10]. At the same time, within the materials' bulk or the interfaces, scattering processes take place. The implication of this is that it is necessary for the orientation of the electrons to remain consistent prior to the emergence of SDS. Given a spin polarised electron's potential travel path, this distance cannot be longer than the electron's mean free path (typically tens of nanometres) [9]. Figure 2.2 provides an overview of the different electron path lengths by referencing the fundamental geometries of GMR sensors.

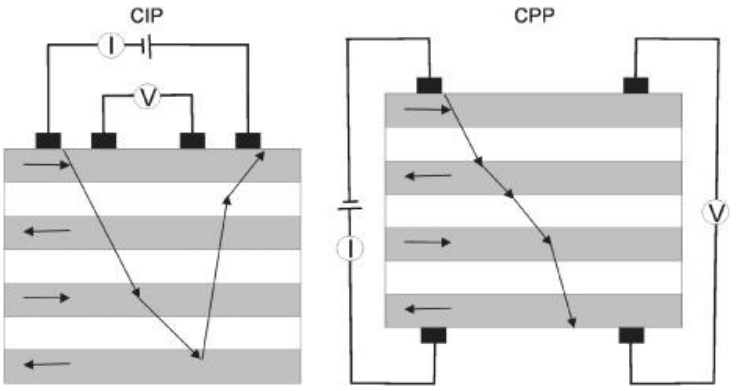

Figure 2.2 Schematic diagram of current in the plane (CIP) and current perpendicular to the plane (CPP) GMR stack [110].

While the sole prerequisite for efficient GMR sensor operation is the transition from parallel to antiparallel magnetisation for the pair of ferromagnetic layers, the application of a sufficiently large magnetic field can result in a transition to the parallel configuration. This is because the magnetic field overcomes the exchange interaction that exists between two magnetic layers. The best way in which to solve this issue was to draw on a pinning mechanism, thereby maintaining the constancy of the magnetisation direction of one of the layers, all the while permitting the transition of the second layer with an external magnetic field.

Within the IBM laboratories, the above considerations gave rise to the spin valve [11][12]. These valves include a typical GMR configuration combined with an antiferromagnetic thin film, the purpose of which is to pin an adjacent ferromagnetic layer via exchange bias, simultaneously permitting the rotation of the free magnetic layer after exposure to an external magnetic field. In this case, the free layer is fabricated using a soft ferromagnetic material, which permits the potential for straightforward switching within a small detected field. The free layer's easy axis of the magnetisation can be parallel or at a right-angle to the magnetisation of the reference layer. Furthermore, a proportional relationship exists between the change in resistance and the dot product of the pair of magnetisation vectors. Consequently, the change in resistance is $\frac{\Delta R}{R}$, which is proportional to the cosine of the angle between

the pair of magnetisation vectors. To facilitate a linear response to the magnetic sensor, a 90° offset regarding the magnetisation vector directions is established. Figure 2.3 gives a contemporary illustration of a spin valve structure, constituted from a ferromagnetic Heusler alloy. It is also possible to pin a magnetic layer by creating a sequence of soft and hard magnetic layers, which are spatially arranged so as to ensure that all pairs of layers have antiparallel coupling. As a consequence, a synthetic antiferromagnet (SAF) can be established.

Strong pinning of the fixed ferromagnetic layer is the foundation of the spin valve structure, and this relies on exchange bias. As a consequence, researchers focused on antiferromagnetic materials. It was possible for the first GMR structures to draw on antiferromagnets with low anisotropy and low thermal stability, including NiO and CoO. Advancements relating to higher anisotropy (approximately 10^7 erg/cm^3) were identified when using antiferromagnetic alloys, including IrMn and PtMn [13], which heightened the degree to which the alloys were thermally stable. As a result of the need for magnetic pinning characterised by strength, stability, and reliability, research initiatives focusing on exchange bias emerged [14].

A sequence of spin scattering events, which subsequently lower the degree to which the sensing structure is efficient, can occur when the complexity of GMR spin valve structures increases, and this is also the case when more magnetic and spacing layers are introduced. Limiting the electron mean free path minimises the spin diffusion length. Furthermore, nanocrystalline defects, including vacancies, roughness, grain boundaries, and interlayer combination at interfaces, can give rise to spin independent scattering. It is also noteworthy that the multilayer structures' quality can be enhanced when recent deposition techniques and annealing are applied, since this underpins the crystallisation quality of the thin film components.

At present, researchers are seeking to identify optimal ferromagnetic compounds with high SDS. Initiatives have highlighted that half-metallic Heusler compounds, characterised by the majority spin band shifted below the Fermi level (giving rise to a theoretical 100% spin polarisation, as noted in Chapter 3), are promising in this respect.

2.1.2 Applications of GMR

Advancements in data storage technology were promoted significantly by the documentation and commercial application of GMR, since it provided a new way in which to approach electronic devices, namely, as devices transporting spin as opposed to electron charge. The degree to which magnetic field detection has become more efficient in recent years was the determining factor that contributed to the utilisation of GMR-based read heads in hard disk drives (HDDs) within a decade of the discovery of the GMR effect. Owing to the higher efficiency of the magnetoresistance sensor, it was possible to decrease the data bit size, thereby permitting exponential increases in the areal density of storage. HDDs store data on a magnetic medium applied to a disk, and one (or a collection of) rotating disks comprise the device. The coating of each disk is a sequence of thin films, and one of these films serves as the recording medium.

The deposition of a granular Co-based alloy (specifically, CoCrPt) takes place so as to ensure the separation of individual grains by a non-magnetic compound (e.g., Cr or SiO_2). In addition to this, the grains are exchange decoupled, thereby maintaining the variable orientations of the magnetisation of the adjacent regions or bits of information. The binary data is read as 1 or 0 depending on the nature of the magnetic transition at certain intervals, and after the information has been written by the write head, it is possible for it to be rewritten once the information bits' magnetisation is switched. A. Moser *et al.*, [15] provides an in-depth examination of magnetic recording technology, while Fig 2.3 gives an illustration of the read-write head in a perpendicular recording media configuration.

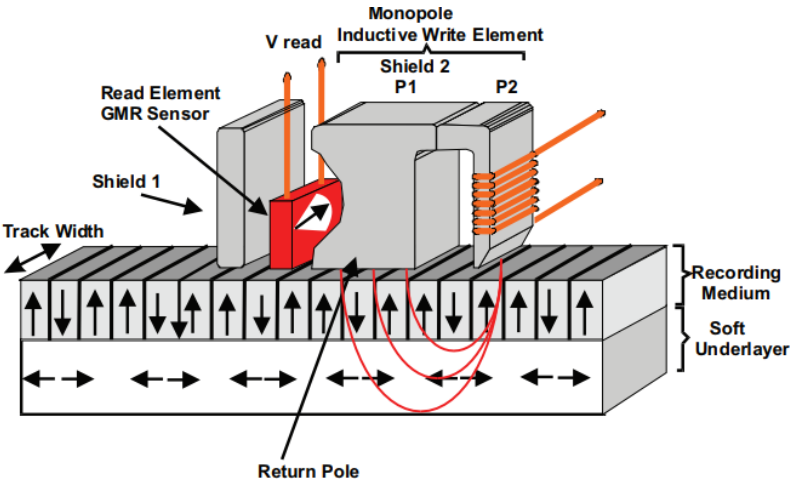

Figure 2.3 A schematic diagram of perpendicular recording media [140].

Owing to the need to downsize the lateral size of storage bits, a comparably sized sensor dimension was required, which in turn promoted the development of the current perpendicular to plane (CPP) configuration of GMR sensors. The limitations of the current in plane (CIP) GMR heads was approached as a consequence of the edge degradation impacts brought about by the device manufacturing process, paired with a higher likelihood of shunting (the result of abbreviated sensor length).

2.2 Current Induced Magnetisation Switching

Based on the studies published by Berger [16] and Slonczewski [17], it was demonstrated that a spin polarised current can induce spin transfer torque. This reverses the magnetisation direction in a ferromagnetic layer in the absence of an external magnetic field. Katine [18] published experimental findings attesting to this. With respect to metallic ferromagnetic materials, the 4*s* conduction electrons are exchange coupled to the 3*d* magnetism inducing electrons, which subsequently undergo excitation as spin waves or magnons. Noteworthily, similarities exist between quantised crystal lattice vibrations (referred to as phonons and the photon light quanta) and this phenomenon. In the forward looking research conducted by Berger, a prediction was made regarding scattering at the material interface. Slonczewski associated the current induced torque to the spin component's spin polarisation and absorption, which is normal to the magnetisation.

One of the key findings published from experiments conducted relating to CPP magnetoresistive devices indicated that the current flowing through the device as a probe of the GMR structure's resistance has the potential to switch the layers' magnetisation direction. In the process of electrons flowing through a ferromagnetic layer, they are spin polarised in the direction of the magnetisation of the ferromagnetic layer. The scattering of electrons with an antiparallel spin orientation are not involved in the conduction mechanism. When the current flows through the pinned ferromagnetic layer, the spins of the electrons align parallel to the magnetisation direction, and while sustaining their polarisation, they are conveyed through the non-magnetic spacer layer. In the process of their interaction with the free magnetic layer, it is possible to classify the transfer of angular momentum as an effective torque

associated with the magnetisation. When the current density is sufficient, it is possible to reverse the magnetisation of the free layer.

According to Katine [18], current driven magnetisation reversal occurs in Co/Cu/Co nanopillars. It is necessary to have a current density amounting to 10^8 Å/cm^2 to switch the magnetisation in a low magnetic field. When a high magnetic field is applied, magnetisation precession occurs. The switching relies on the direction of the current, which demonstrates that the reversal mechanism is caused by spin transfer torque and not by the magnetic field.

2.3 Tunnelling Magnetoresistance

Despite the fact that GMR was responsible for drawing research attention towards the domain of spintronics, magnetic tunnel junctions (MTJ) are now found in place of GMR devices within HDD read heads and MRAM applications affording greater magnetoresistance. Such devices permit greater resistance, thereby ensuring that tunnel junctions are aligned with complementary metal–oxide–semiconductor (CMOS) technology, straightforward scalability, and thermal stability. In view of these considerations, the purpose of this section is to examine tunnelling magnetoresistance (TMR)-based devices.

In a variety of ways, tunnelling magnetoresistive (TMR) junctions are comparable to GMR structures. However, rather than a conductive non-magnetic interlayers, magnetic tunnel junctions (MTJ) draw on an insulating oxide layer, the purpose of which is to separate the two ferromagnetic films. Hence, the CPP configuration is utilised to bypass the metallic conduction through the multilayer structure. As indicated by the name, the conduction mechanism that lies at the centre of TMR structures is dependent on the quantum tunnelling of electrons, which percolate through the non-conductive barrier. It is important to recognise that TMR is not simply dependent on the SDS within the electrodes; rather, it also relies on the conduction

states that are present to tunnel from one side of the insulating oxide barrier to the other (see Figures 2.4 and 2.5).

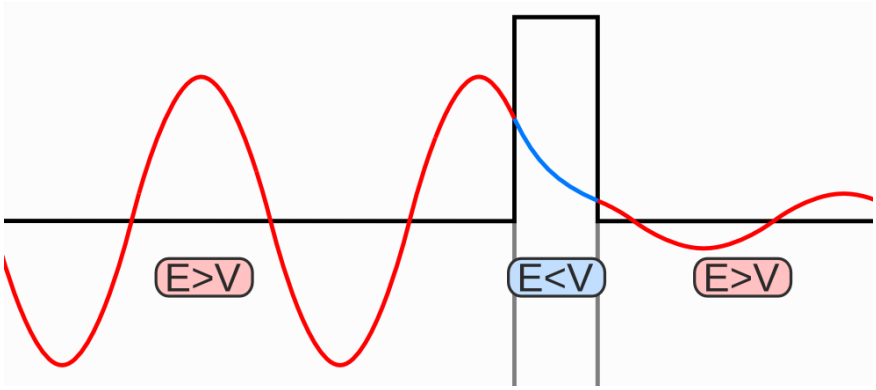

Figure 2.4 A schematic diagram of quantum tunnelling.

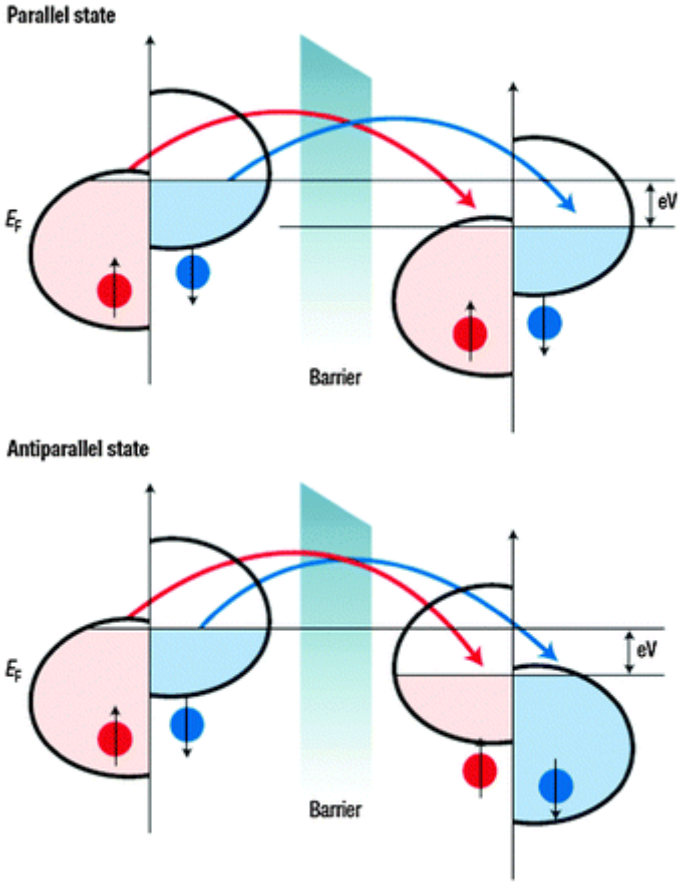

Figure 2.5 A schematic of spin split band structure and the TMR effect related to the Fermi Energy (E_F) [141].

With respect to the parallel orientation, numerous majority conduction states and majority valence states lead to a considerable electron flow, and as such, a low resistance. Regarding the antiparallel orientation, less majority and minority states can lead to a significant resistance. The implication of this is that for every spin direction at the Fermi energy or the spin polarisation, the TMR relies on the number of the available states. This is represented in the following equation:

$$\frac{\Delta R}{R} = \frac{R_{AP} - R_P}{R_P} = \frac{2P_{\mathrm{F1}}P_{\mathrm{F2}}}{1 - P_{\mathrm{F1}}P_{\mathrm{F2}}} \qquad (7\text{-}2)$$

where P_{F1} and P_{F2} denote the spin polarisations of the two ferromagnetic layers in the junction. Now, it should be noted that the P_{F1} can be defined in the following way:

$$P_{\mathrm{F}} = \frac{N_{maj} - N_{min}}{N_{maj} + N_{min}} \qquad (7\text{-}3)$$

where N_{maj} and N_{min} denote the number of electrons in the majority and minority spin channels at the Fermi level, as accounted for by the density of states (DOS) of the ferromagnetic layers. In view of the fact that spin polarised materials, including Heusler compounds, should theoretically display 100% spin polarisation (see Chapter 3), it is clear that the TMR values are anticipated to be significant.

By employing a Fe/Ge/Co in plane magnetic tunnel junction (iMTJ) utilising low temperature electrical assessments, it was possible for Julliere to discover the TMR effect in 1975 [19]. In the final years of the twentieth century, studies such as Miyazaki *et al* [20] and Moodera *et al* [21] found that TMR ratios of greater than 10% could be attributed to iMTJs when an AlO_x barrier was used and measurements took place at room temperature. In 2000, advancements took place for the AlO_x-based MTJs, but the theoretical bound for the magnetoresistance ratio 70%, had already been achieved [22]. Noteworthily, Julliere's formula [19] estimated this magnetoresistance ratio value, where the TMR ratio is determined by the ferromagnetic layers' spin polarisation.

Following the turn of the new millennium, the studies conducted by Butler *et al* [23] and Mathon *et al* [24] predicated that a TMR ratio of greater than 1000% could be obtained. In each case, the calculations were relevant for structures such as Fe

(001)/MgO (001)/Fe (001), where (001) crystalline orientation of the bcc Fe layer was required for heightened conveyance of spin polarised electrons. In the following years, studies such as Parkin *et al* [25] made ongoing strides in the domain of Fe-based iMTJ, thereby establishing TMR ratios of 88% at room temperature for epitaxial structures, the deposition of which took place by molecular beam epitaxy (MBE). In the studies of Djayaprawira *et al*.,[26] and Hayakawa *et al*.,[27] TMR ratios amounting to over 200% were identified at room temperature for systems utilising CoFe and CoFeB magnetic layers, with the iMTJs deposited by the conventional sputtering technology on Si substrates.

In a recent study, Ikeda *et al*.,[28] indicated a TMR ratio of greater than 600% (room temperature), which exceeded 1000% at low temperatures. This was conducted utilising pseudo-spin-valves in the absence of the pinning antiferromagnetic layer, and post annealing took place at 525%. Noteworthily, these findings are consistent with the early theoretical models formulated in response to the effect.

One of the main obstacles that researchers had to overcome when attempting to develop perpendicular MTJs (pMTJ) related to the deposition of highly crystalline bcc CoFeB (001)/MgO (001)/ CoFeB (001) with perpendicular anisotropy. It is not possible to use perpendicular anisotropic materials, including CoCrPt and Co/Pt multilayers, since these are associated with varying crystal structures, thus impairing epitaxial growth across the MTJ. TMR ratios of greater than 90% were identified for pMTJs in the context of $L1_0$ ordered FePt [29], as well as Co/Pt superlattice arrangements [30]. The first initiatives relating to pMTJ development relied on the utilisation of materials with in plane and perpendicular anisotropy, and sophisticated deposition processes had to be conducted. According to the study conducted by Ikeda *et al*., [31], the researchers identified a TMR ratio of greater than 100% for standard CoFeB/MgO/CoFeB MTJs, and the result was demonstrated that a slim layer of CoFeB is characterised by perpendicular anisotropy after deposition onto MgO (001). As a consequence of this finding, pMTJ production took place on a huge scale for MRAM applications.

As the results indicate, it is possible to draw on either GMR or TMR sensors in HDD read heads, as well as MRAM applications, but both are associated with unique

strengths and weaknesses. The resistance area product of the two is different, in particular, greater for TMR sensors, and this stems from the tunnelling effect. Furthermore, the greater resistance of MTJs has the effect of causing noise problems, paired with an elevated resistor capacitor time constant, thereby limiting operation bandwidth. However, it should be recognised that the better TMR ratio results in higher output voltage signal, thereby resulting in the limitation of errors that occur when the data reading process is underway. In addition to this, GMR sensors are energy-efficient when compared to TMR sensors, but as a result of the lower MR ratio (approximately 20%), considerable current densities are required to facilitate usable signal voltage. While this can have an impact on the degree to which a device is thermally stable, it is more pertinent to note that large currents, especially in the context of spin transfer torque applications, can impair the degree to which devices are magnetically stable.

2.4 Magnetic Random Access Memory

Non-volatile RAM is characterised by its ability to retain memory content even in the absence of a power source, and the innovation of magnetic random access memory (MRAM) utilises this as its foundation. At present, researchers are seeking to modify MRAM technology so as to facilitate energy-efficiency as well as standard low voltage technology. The key objective of most research projects is to design computing technology that can quickly alternate between powered and unpowered states (when not needed and needed, respectively), thereby promoting energy sustainability into the future.

A Conventional MRAM cell is illustrated in Figure 2.6, drawing on magnetic field writing stimulated by current flowing through a world line, which is employed as a gate operation device for the isolation transistor, and a bit line. When the device is engineered in this way, it is necessary to use a relatively large current, since this minimises the dimensions of the tunnel junction (because the field needed for switching grows when the MTJ is scaled down). Evidently, since power consumption

is proportional to the chip capacity, this is not a viable approach. Alternatively, the device layout can be based on the spin torque mechanism.

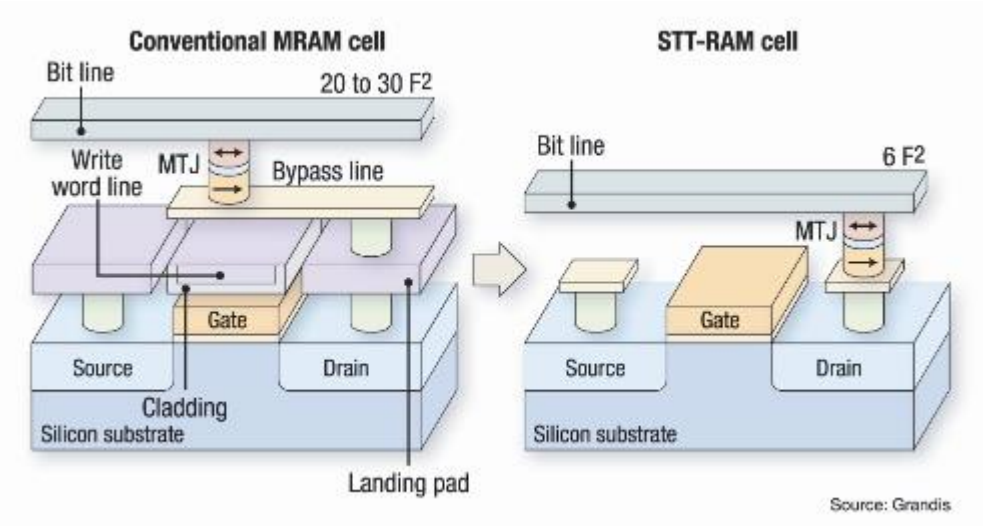

Figure 2.6 A schematic diagram of conventional MRAM cell and spin transfer torque (STT) RAM cell.

With respect to MTJs, the spin polarised current induces spin transfer torque on the free layer's magnetisation, and in the event that the current threshold limit is surpassed, the free layer's magnetisation orientation is reversed. Regarding the inverse mechanism, when electrons are transmitted through the free layer and subsequently arrive at the pinned (fixed) layer, the spin current can move through when the spin polarisation is parallel. In the context of the antiparallel configuration, the inversely polarised electrons reflected back at the pinned layer interface with the tunnel barrier. When a certain threshold value is exceeded, the strength of the spin current that has been reflected increases to the required level, thereby switching the free layer's magnetisation.

The initial MTJ was employed for MRAM demonstration in 1996 [32]. Just two years ago, in 2016, Toshiba Corp reported that a prototype 4 Gbit STT-RAM had been developed, which is constituted of eight 512-Mbit banks. The smallness of the cell area can amount to $9F^2$, where F is the fabrication rule [33]. Future iterations of MRAM and STT-RAM technology must satisfy the current considerations, including the lowering of the switching field of critical current density, as well as a lowering of the fabrication rule. In the study conducted by Yakata [34], a synthetic ferromagnet

(specifically, CoFeB/Ru/CoFeB) was employed, and this was applied as a free layer by AIST. The results of the study demonstrated an increase of 500% with respect to thermal stability, accompanied by an 80% increase in the critical current density. Noteworthily, it is possible for this configuration to establish a 10 Gbit STT-RAM device. The consideration that has yet to be addressed to create a high-density STT-RAM is to ensure that the fabrication rule is reduced. According to A. Hirohata *et al*., substituting the supplementary transistor with a different design may solve this problem.

In addition to the need for higher thermal stability, researchers are continually engaging in initiatives to heighten the TMR ratio. A value of greater than 150% is optimal for the achievement of a sub 10 ns read-out. The write current density (J_c) is less than 10^6 A/cm^2, while it is necessary for the MTJ breakdown voltage to exceed the write voltage (approximately 0.5V at 10 ns) by three times. In the context of STT applications, for which large perpendicular anisotropy is a necessity, the Gilbert damping constant must be minimised to the greatest possible extent.

Chapter 3

Heusler Alloy

In 1903, Fritz Heusler made an intriguing discovery. He found that an alloy, Cu_2MnAl, exhibited ferromagnetic qualities. What is remarkable about this compound is that neither copper, manganese nor aluminium are in themselves, ferromagnetic [35][36].The discovery of ferromagnetic alloys presented a novel category of materials that has since grown to include more than 1000 compounds, which are classified as Heusler compounds. As Figure 3.1 indicates, all Heusler compounds are comprised of three metallic or semiconductors elements, in a 1:1:1 (half-Heusler alloys) or 2:1:1 (full-Heusler alloys) ratio.

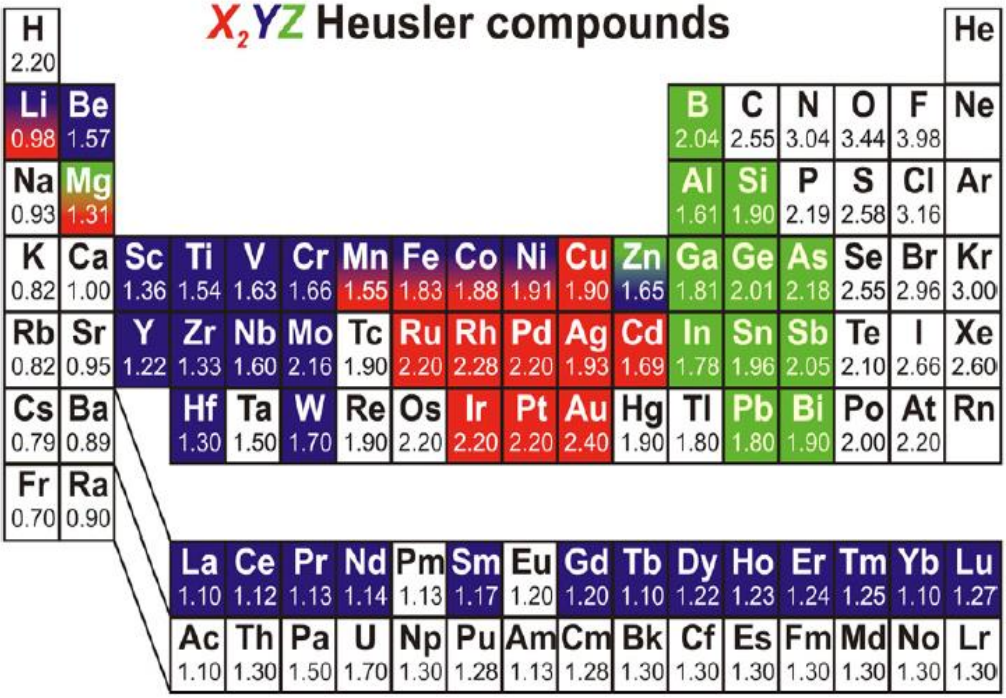

Figure 3.1 Periodic table of the elements. The large number of Heusler materials can be formed by combining different elements according to the colour scheme [37].

By counting the number of valence electrons, it is possible to predict the properties of many Heusler compounds; for example, those with 27 valence electrons are superconducting non-magnets for full-Heusler alloys. Semiconductors with tuneable band gaps between 0 and 4 eV are an important group of Heusler compounds that have particular relevance to photovoltaic cells and thermoelectric technologies [37]. The band gap changes in response to alterations to the elements in the compound. These compounds are also expected to behave as topological insulators through various spin-

polarised edge, conduct electricity on the surface but not within the body of the material.

3.1 Heusler Alloy Structure

In both the theoretical and experimental literature addressing Heusler alloys, researchers have found that the structural order of each compound has a significant effect on its characteristics. In view of this close connection between the structural and functional aspects of the compounds, when examining their physical characteristics, it is necessary to engage in comprehensive structural examination. The purpose of this section is to examine the various ways in which Heusler compounds can be structurally characterised.

Broadly speaking, Heusler compounds can be categorised into one of two groups: firstly, if they have a composition 1:1:1, then they are referred to as half-Heusler compounds; and secondly, if they have a composition 2:1:1, then they are denoted stoichiometric full-Heusler compounds. Regarding the first category, half-Heusler compounds ($C1_b$ structure) are distinguished by the following physical characteristics: firstly, half-metallic ferromagnetism; secondly, shape memory properties; thirdly, semiconducting; fourthly, thermoelectric properties; and finally, behaviour as a topological insulator [38], [39].

For ordered X_2YZ Heusler compounds, along with the space group $Fm\bar{3}m$, they undergo crystallisation within the $L2_1$ structure. Based on the inorganic crystal structure database (ICSD) notation, this is denoted Cu_2MnAl. With respect to the Y atoms, these are found at the 4*b* (1/2, 1/2, 1/2) position, while the X atoms and the Z atoms are found at the Wykhoff position, 8*c* (1/4, 1/4, 1/4), and 4*a* (0, 0, 0), respectively. For the purpose of the present study, two Heusler alloys have been studied, Mn_2VSi and Mn_3Ga, which are full-Heusler compounds. It is possible to create a series of $L2_1$ structure variants in the event that the X, Y, and Z atoms undergo intermixing with respect to the relevant crystallographic positions. Noteworthy, this results in a range of symmetries and structural features [40]. The purpose of the following paragraphs is to provide a brief outline of frequently observed structures, the schematic diagram is shown in Fig 3.2 :

- $D0_3$-type structure

  Space group $Fm\bar{3}m$ is conserved but the $D0_3$ structure arises when the X and Y (or X and Z) atoms are intermixed with respect to their crystallographic positions. In ISCD notation, this is written as BiF_3.

- $B2$-type structure

  When the Y and Z atoms undergo random intermixing with respect to their crystallographic positions, the Y and Z sites can emerge as equivalent, which gives rise to the $B2$ structure (often described in reference to the CsCl lattice). It is also noteworthy that because of the intermixing, a CsCl lattice characterised by the X atom at the centre of the cube, surrounded in a random way by the Y and Z atoms, is generated. The reduction of symmetry takes place, and the space group given rise to is $Pm\bar{3}m$, denoted in ICSD notation the CsCl structure. In addition, every X atom is located in the Wykhoff position ($1b$), while the Y and Z atoms are distributed in a random way on the $1a$ position.

- $A2$-type structure

  For X_2YZ Heusler compounds, randomness to the greatest possible extent with regard to intermixing on the Wykhoff position ($2a$) gives rise to the $A2$ structure. One of this structure's features is limited symmetry $Im\bar{3}m$. In addition, the X, Y, and Z sites emerge over time as the same, thereby creating a body-centred cubic lattice, referred to in ICSD notation as the tungsten (W) structure.

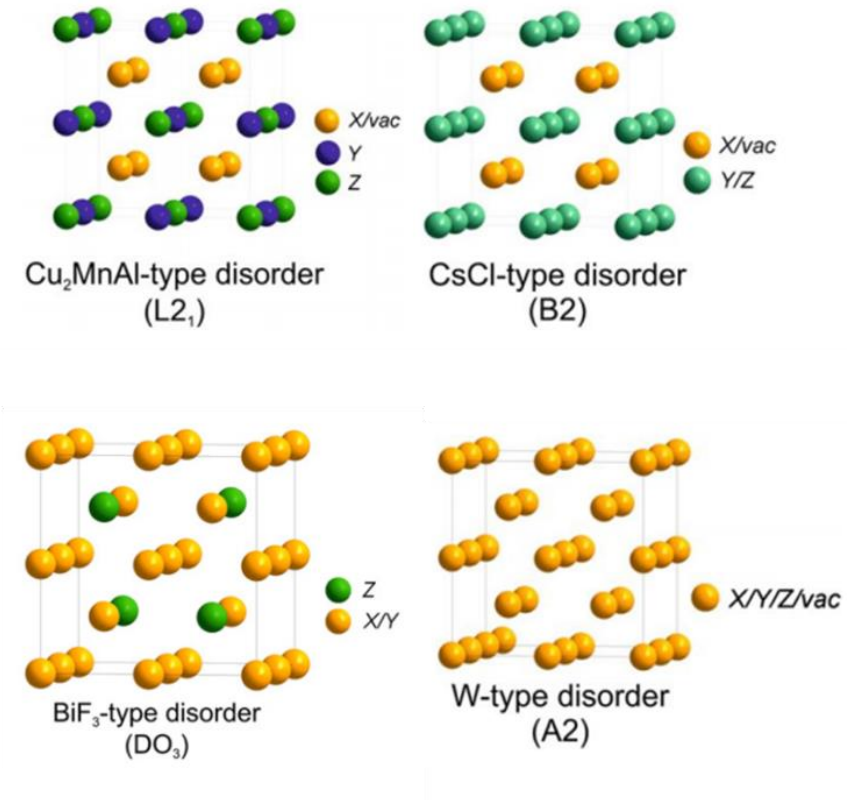

Figure 3.2 Overview of the most common types of structure in the Heusler compounds [37].

Given the cubic symmetry that characterises the structural features of Heusler compounds, this has a limiting impact on the degree to which the materials have functional utility when high magnetocrystalline anisotropy is required. To be more specific, this arises in the context of exchange bias configurations which require thermal stability of the antiferromagnetic (AF) configuration. Regarding the Mn_2YZ Heusler compound structure, tetragonal distortion was identified in the study conducted by Graf *et al.* [37], which stems from the augmentation of the *c* axis, thereby allowing a pair of Mn atoms to exist in different local symmetries (for Mn_2NiSn, cubic and tetragonal symmetries). Inverse structures are commonly associated with tetragonal distortion, here one Mn for 2*b*, where the second Mn and the Y atom both have the 4*d* position. It is also notable that the Z atom lies at the 2*a* position, comparable to the regular structures with tetragonal distortion. The key element in this set of Heusler compounds is Mn_3Ga [41][42].

Regarding the most straightforward and accessible macroscopic approach to identifying the level of disorder in a Heusler structure, X-ray diffraction (XRD) is

frequently applied. Typical (220), (200), and (111) superlattice reflections are anticipated from the ordered $L2_1$ and inverse Heusler structures, whereas the semi-disordered *B2* structure is predicated to have no superlattice reflection (111). The prediction also states that *A2* will only be associated with (220) reflections.

3.2 Slater-Pauling Behaviour of the Heusler alloys

In half-Heusler compounds, the total moment in μ_B/f.u. (formula unit) follows a simple rule:

$$M_t = Z_t - 18 \tag{3-1}$$

Where M_t is the total spin magnetic moment and Z_t is the total number of valence electrons. Z_t is given by the sum of the number of spin-up and spin down electrons, while M_t is given by the difference:

$$Z_t = N_\uparrow + N_\downarrow \tag{3-2}$$

$$M_t = N_\uparrow - N_\downarrow \tag{3-3}$$

$$M_t = Z_t - 2N_\downarrow \tag{3-4}$$

This is a direct analogue to the well-known Slater-Pauling behaviour of the binary transition metal alloys [43][44][45]. The difference between half-Heusler alloys and transition metal alloys is that in half-Heusler alloys, the 9 minority bands are fully occupied. This means that the screening is achieved by filling the majority band, while in transition metal alloys, the majority bands are fully filled with 5 *d*-states, and charge neutrality is achieved by filling the minority bands. Hence, the total spin magnetic moment in transition metal alloys is given by:

$$M_t = 10 - Z_t \tag{3-5}$$

Figure 3.3 shows the calculated total spin magnetic moments for half-Heusler alloys plotted against the total number of valence electrons [46].

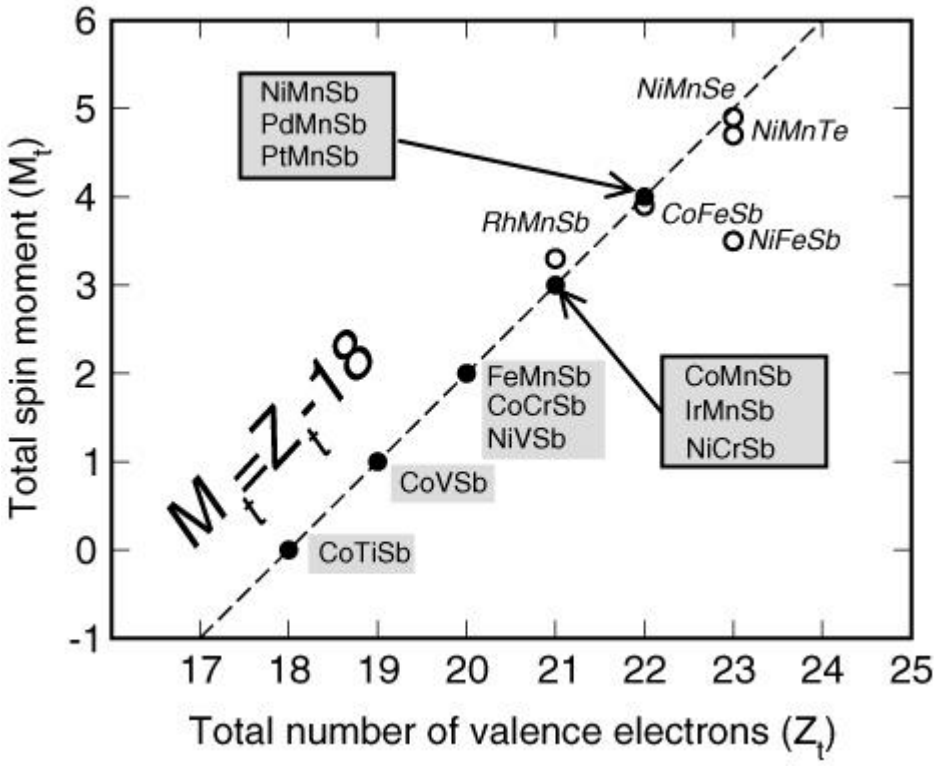

Figure 3.3 Calculated total spin-moment per unit cell as a function of the total number Z_t of valence electrons per unit cell for all the studied half-Heusler alloys. The dashed line represents the Slater-Pauling behaviour [46].

In full-Heusler alloys, the total spin magnetic moments (M_t) can be derived using a similar approach. Figure 3.4 shows the total spin magnetic moments for all the compounds under study as a function of the total number of valence electrons. The dashed line indicates the half metallicity rule of the full-Heusler alloys:

$$M_t = Z_t - 24 \qquad (3\text{-}6)$$

The minority band is occupied by 12 electrons.

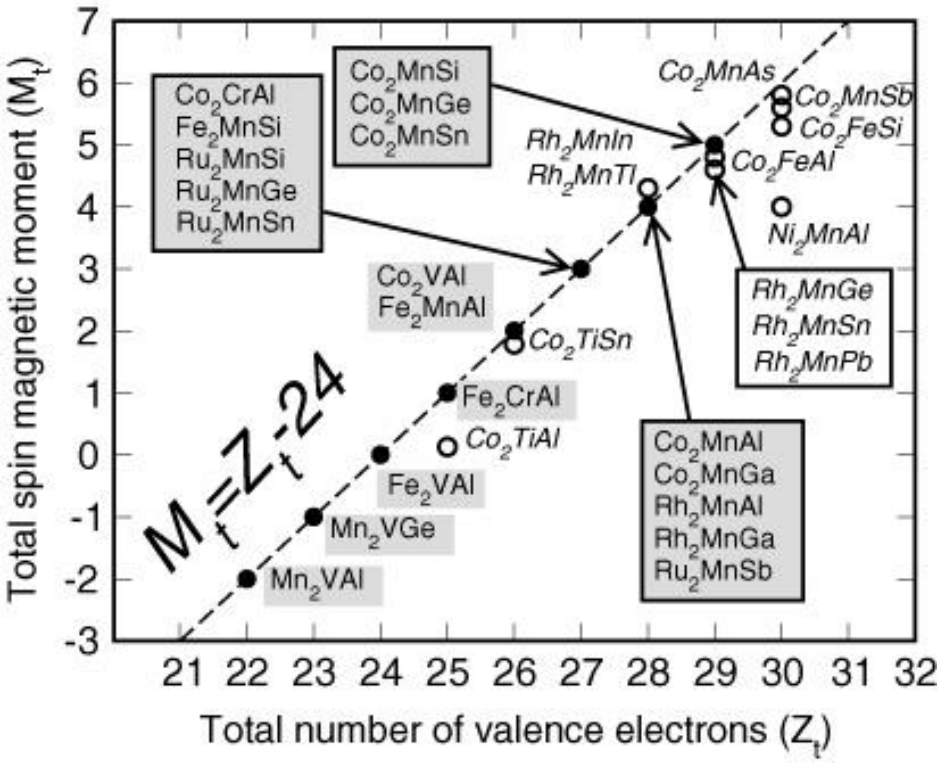

Figure 3.4 Calculated total spin-moment per unit cell as a function of the total number (Z_t) of valence electrons per unit cell for all the studied full-Heusler alloys. The dashed line represents the Slater-Pauling behaviour [142].

3.3 Antiferromagnetic Heusler Alloys

A noteworthy case in the context of applications are those Heusler compounds referred to as half-metallic antiferromagnetic (AF) materials. More specifically, these are constituted from magnetic elements with precisely 18 half-Heusler (or 24 full-Heusler) valence electrons, each characterised by total zero spin magnetic moment under half-metallicity. In applied contexts, half-metallic AF materials play a particularly important role because they do not produce external stray fields. According to X. Hu *et al*. [47], this means that they create no external stray field and thus minimise energy losses.

In these half-metallic materials, the two spin bands display divergent behaviours. The majority-spin band, usually known as the spin-up band, exhibits a metallic behaviour in which the density of states (DOS) at the Fermi level (E_F) is non-zero. The minority-

spin band (spin-down) shows a typical semiconducting behaviour with a band gap at E_F. Half-metals are the hybridisation between metals and semiconductors. A conventional metal's DOS is illustrated below, along with that of a semiconductor and a half-metal (Figure 3.5). In an ideal situation, half-metallic ferromagnets display 100% spin polarisation at E_F, which contributes to their fully spin-polarised current. As a result of this, they can serve as the optimal spin injectors into a semiconductor or non-magnet, thereby optimising the degree to which spintronic applications are efficient [48].

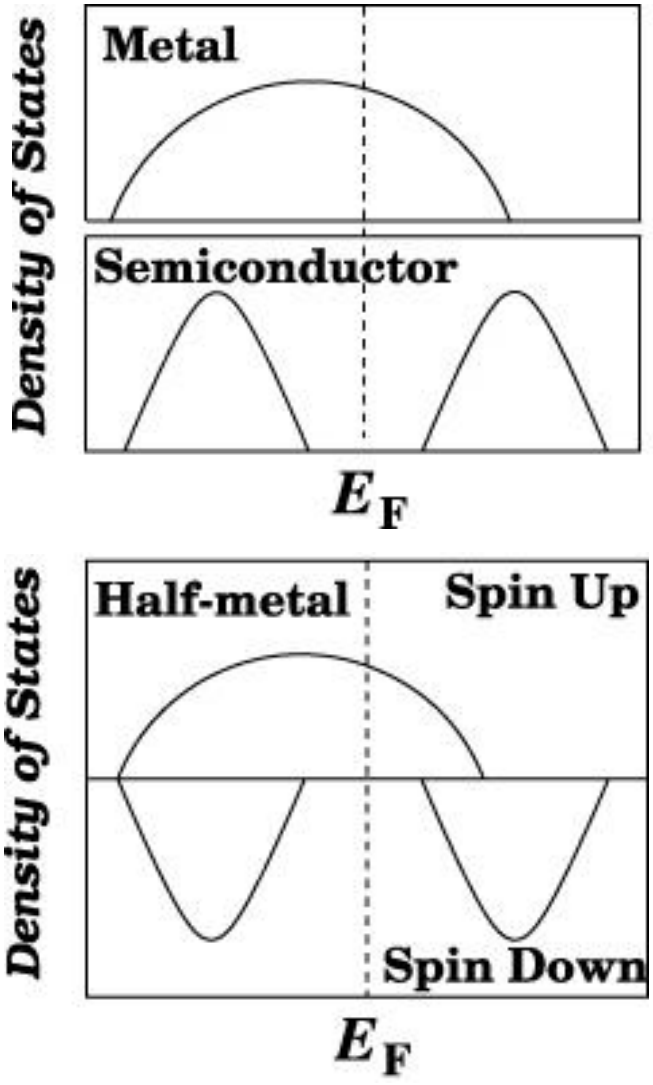

Figure 3.5 Schematic representation of the DOS for a half-metal with respect to normal metals and semiconductors [46].

In 1988, following the observation of giant magnetoresistance (GMR), antiferromagnetic materials began to be applied in spin valve structures, and they have since garnered extensive scholarly attention [49]. In recent years, ground-breaking research in the field of AF spintronics has identified several benefits associated with the use of AF materials for data storage, including external magnetic field insensitivity, the absence of short range magnetic interactions, and intrinsic high frequency AF dynamics. Furthermore, in the field of data storage, the expectation in the research community is that magnetically compensated AF materials will entirely substitute for the frequently applied ferromagnetic materials [50]. Before antiferromagnets (AFs) were applied in numerous industrial areas, the intrinsically antiparallel aligned non-magnetic materials were identified as fascinating but lacking in utility, as argued by Louis Néel in 1970 [50][51]. As a consequence of this, most researchers were not interested in examining the fundamental mechanisms and potential use cases of AFs, and this was even the case after the observation of exchange bias in 1956 [52]. Resultantly, AF materials were regarded as subjects of interest rather than research topics with enormous potential for industrial applications. In view of these considerations, investigations into AF Heusler alloys at this time received little attention among researchers.

Oxley *et al*. [53] conducted a significant experiment addressing the crystallisation of the AF bulk compound Cu_2MnSb, which outlined its chemical and crystallographic aspects. The AF transition was proven as a result of magnetic susceptibility, and the Néel temperature was identified at 38 K. Then, their research presented the standard experimental process that can identify AF phases in Heusler alloys, and this notably occurred before the identification of the exchange bias phenomenon. Other studies conducted around this time, including Kübler *et al*. [54], investigated the magnetic properties as a function of temperature for various X_2MnZ full-Heusler alloys, where a positive AF configuration for Pd_2MnIn was discovered at lower than 60 K for the determination of the energy disparity between the ferromagnetic (F) and AF ground states. In addition to this, the research conducted by Kübler *et al*. indicated a related band gap at E_F.

Neumann *et al*. [55], were the first to examine the phenomenon of itinerant antiferromagnetism in the context of Heusler alloys, and this took place within a project investigating magnetic transitions pertaining to bulk Pd_2TiIn. Based on

susceptibility measurements, the Néel temperature amounted to 110 K, but it is critical to note that the overall magnetic moment amounted to 4.9 μ_B/formula unit when no constituent elements were associated with a large spontaneous moment. The high induced magnetic moment value was comparable to Pd_2MnIn at the point where the moment was restricted to the Mn atom in a collinear AF type-2 structure, and the moments were arranged in parallel with respect to the (111) plane, where the arrangement across planes was antiparallel. Noteworthy, the account given for the large induced moment for the Ti-based Heusler alloy was formulated in response to the observation of spin fluctuations, which signalled weak itinerant ferromagnets [56].

Despite the way in which preliminary research in this field reported the presence of AF stable phases in the context of full-Heusler alloys, and then outlined the relationship between structural and magnetic properties (so as to underline the source of AF coupling), these experimental studies neglected to examine applications. In addition, they overlooked various exchange bias parameters (*e.g.*, film thickness and temperature dependence). Furthermore, it is important to recognise that the preliminary research studies focused in bulk form. It was not until the turn of the new millennium that experimentation on AF Heusler alloy thin films emerged as a widespread practice.

A particularly notable area of investigation relates to full-Heusler compounds in which the X and Y are characterised by identical chemical elements. This could contribute to the more straightforward growth of such materials, thereby improving the various features of the applications that use them as their foundation. Furthermore, in the present context, it is possible to bypass the degradation of the magnetic properties that results from impurities and atomic swaps, since the X and Y are the same chemical elements.

In this research, Mn_2VSi and Mn_3Ga Heusler alloys have been investigated. In the following section, more information with regards to these two materials will be provided.

3.4 Mn_2VSi

Mn_2VSi Heusler alloys are believed to be half-metallic ferrimagnets which can be stabilised in face centred cubic (fcc) structure with lattice parameter $a = b = c =$ 0.567 nm [57]. For Mn_2VSi compounds, the Mn spin moment reaches a value of $-0.87\ \mu_B$ and the V moment of $0.35\ \mu_B$, with the total spin moment amounting to $-0.62\ \mu_B$ [57]. According to Galanakis *et al*. [58], Co substitution for Mn stabilizes the half-metallic character of the parent compounds. When the total number of valence electrons reaches 24, the total spin moment vanishes as predicted by the generalised Slater-Pauling rule. Thus an alternative way to create half-metallic antiferromagnets for realistic spintronic applications is to simply introduce Co atoms in the Mn_2VAl and Mn_2VSi half-metallic ferrimagnets. But the magnetic properties of the Mn_2VSi compounds are strongly dependent on the substrate and the growth conditions and the latter compounds will very easily switch between the magnetic (ferrimagentic) and non-magnetic (antiferromagnetic) configurations [57]. Relatively little experimental or theoretical data exists regarding Mn_2VSi alloys, but due to the similarities between Mn_2VSi, Mn_2VAl, and Ni_2MnAl, we are able to better understand Mn_2VSi alloys when examining them comparatively against Mn_2VAl and Ni_2MnAl alloys.

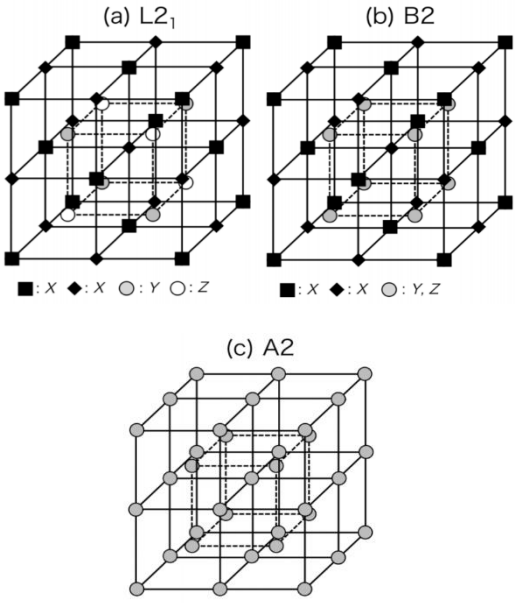

Figure 3.6 Schematic images for Heusler alloys with bcc structure[60].

Mn_2VAl has three types of ordered phases, as shown in Figure 3.6. $L2_1$ Mn_2VAl is known as a ferrimagnetic full-Heusler alloy [59]. Magnetisation and neutron diffraction measurements of a bulk sample have demonstrated that *A*2- type Mn_2VAl is an antiferromagnet with a Néel temperature above 600K (R. Y. Umetsu *et al* in preparation).

In general, the Heusler-type AF alloys have a similar lattice, which aligns with ferromagnetic materials for spintronics, such as Co-Fe alloys. According to Tsuchiya *et al*. epitaxial *A*2-type antiferromagnetic Mn_2VAl thin film with Fe ferromagnetic layer on top was found to have an exchange bias amounting to approximately 120 Oe at 10 K [60].

In the notable publication issued by Dong *et al*. [61] addressing Ni_2MnAl thin films, the highly-ordered Heusler alloy was deposited by molecular beam epitaxy (MBE) on GaAs(001) single-crystal substrates. This was achieved by employing a thin seed layer of $Sc_{0.3}Er_{0.7}$, since this facilitated the enhancement of lattice-matched growth for the Heusler alloys. This publication is particularly noteworthy in the context of the present research, since its findings served as one of the motivating factors for conducting this study. To be more specific, Dong *et al*. demonstrated that it is possible to modify the degree of ordering in the Heusler structure when the deposition temperature is changed from 180 ºC (for the partially disordered *B*2-type structure) and 400 ºC (for the completely ordered $L2_1$ phase). Regarding the stable AF phase of partially disordered Ni_2MnAl, this was confirmed by employing an exchange bias measurement, which took place in response to the addition of a ferromagnetic Heusler layer, brought into contact with the AF. The study further demonstrated that the fundamental parameter is the growth temperature (T_g), which alters the degree in which the Heusler alloy structure is ordered.

The hysteresis loops in Fig. 3.7 show the Ni_2MnAl phase transformation as a function of growth temperature. Ni_2MnAl (64 nm)/Ni_2MnGe (12 nm) bilayer sample shows a loop shift of 35 Oe when the sample is field cooled to 10 K.

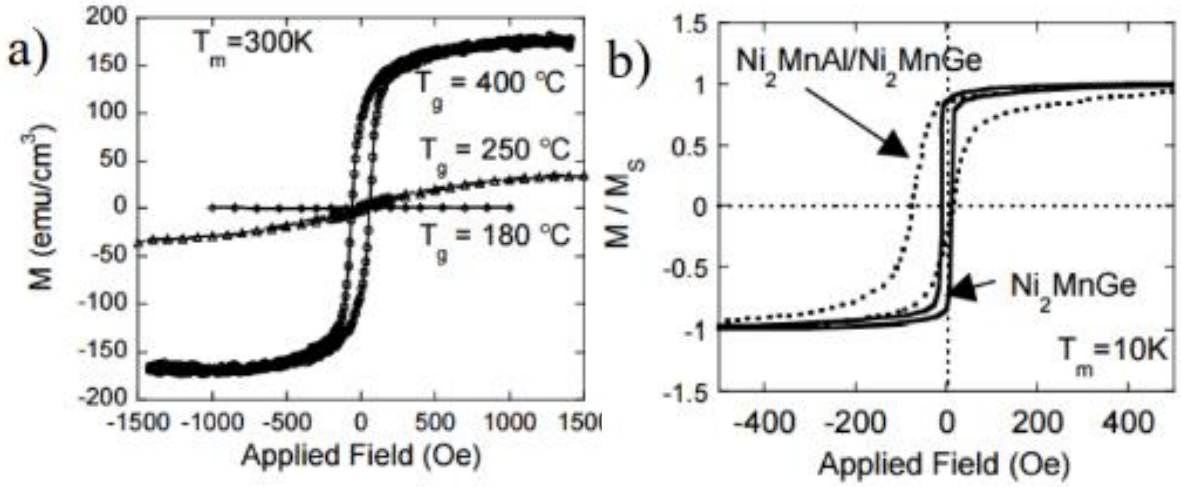

Figure 3.7 (a) Hysteresis loop of Ni_2MnAl film deposited at different temperatures. (b) Hysteresis loops of Ni_2MnAl/Ni_2MnGe bilayer sample and Ni_2MnGe thin film measured at 10 K [61].

3.5 Mn_3Ga

Mn-rich Heusler alloys have attracted much attention in spin transfer torque, spin-Hall effect and rare earth free hard magnets. Mn_2-based Heusler compounds quite often crystallise in the inverse structure with antiparallel coupled magnetic moments on Mn atoms; the ferri- or antiferromagnetic order and the lack of inversion symmetry leads to the emergence of new properties that are absent in ferromagnetism. Elemental Mn is not ferromagnetic, despite having a *d* band that is more than half full. Of all the elements, the unit cell of the stable cubic α-Mn phase is the largest and most intricate. The unit cell of α -Mn is made up of 48 atoms distributed over four inequivalent sites, each site resulting in different magnetic moments ranging between 0.5 μ_B and 2.8μ_B. Below 90 K, Mn orders in various antiferromagnetic and ferromagnetic structures [62][63]. However, when combined in binary or ternary compounds, it leads to the emergence of a vast range of magnetic properties, including room temperature magnetism, such as the ferromagnetic Cu_2MnAl Heusler alloy with the Curie temperature T_c = 603 K, discovered by Friedrich Heusler in 1903 [35][36], long before the development of quantum mechanics.

As a binary Heusler alloy, many studies have been carried out experimentally and theoretically to reveal the magnetic properties of Mn_3Ga alloys. The Mn-Ga alloys show a manifold of stable phases and Mn_3Ga was reported to exist in a face-centred cubic (fcc) structure. Wurmehl *et al*. [64] predicted that Mn_3Ga becomes a half-metallic fully compensated ferrimagnet in the cubic $D0_3$-type phases. However, the experiments showed that the cubic phase of Mn_3Ga is not stable. It is possible to stabilise the bulk [65][66] and thin films of Mn_3Ga (in an experimental context) as ε-Mn_3Ga. This phase is antiferromagnetic with a hexagonal $D0_{19}$ crystal structure which has a non-collinear triangular magnetic structure with antiferromagnetic behaviour [65][67] as shown in Fig 2.6 (a). This is comparable to the triangular magnetic state of a conventional $IrMn_3$ antiferromagnet [68]. In the triangular antiferromagnetic structure three magnetic moments point in three different directions which causes the net magnetisation to be zero [69]. ε-Mn_3Ga has been reported to have a high Néel temperature (T_N) of 470 K [65]. Mn_3Ga also forms a tetragonal phase of τ-Mn_3Ga with the $D0_{22}$ structure [70]. This ferrimagnetic Mn_3Ga is reported to possess a large uniaxial anisotropy of 1×10^6 J/m^3[71] and high Curie temperature (T_C) of around 770 K [70]. Bulk- and thin-film forms of the hexagonal material can be annealed to realise

the τ-Mn_3Ga phase [72]. The Mn_3Ga tetragonal phase has been grown epitaxially on different substrates [73][74][75]. Both magnetisation and anisotropy are reported to be dependent upon the $Mn_{3-x}Ga_{1+x}$ alloy stoichiometry and the surrounding conditions of the Mn_3Ga films [73][75]. In this work, antiferromagnetic ε-Mn_3Ga has been successfully produced which will be discussed in Chapter 7.

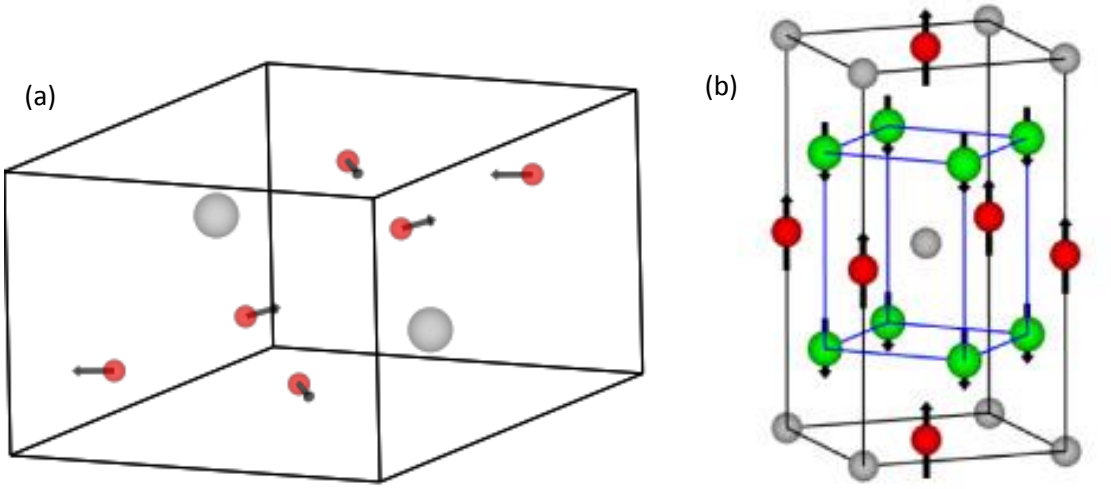

Figure 3.8 (a) Schematic crystal structure $D0_{19}$ hexagonal antiferromagnetic Mn_3Ga [67], and (b) $D0_{22}$ tetragonal ferrimagnetic Mn_3Ga [76].

Mn-Ga films are known to have high resistivity and high spin polarisation at the Fermi level, which makes them competitive candidates for perpendicular spin torque memory. According to Winterlik *et al.*, the stoichiometric $D0_{22}$ Mn_3Ga shows 88% spin polarisation at the Fermi level [41]. The spin polarisation measurements of Mn-Ga compounds with different seed layers have been performed by Stamenov *et al.* using point Andreev reflection spectroscopy [76][77], the results are shown in Table 3.1. When attempting to develop novel alloys with significant spin polarisation, spin polarisation measurements are critical. Although tunnelling magnetoresistance (TMR) measurements can be employed for the purpose of estimating the spin polarisation of ferromagnetic electrodes of magnetic tunnelling junctions (MTJs), the preparation of TMR pillars depends on the presence of a thin film stack and, moreover, time-intensive microfabrication processes. Contrastingly, point contact Andreev reflection has the capability to estimate existing spin polarisations of bulk alloys in a comparatively straightforward manner. However the most significant disadvantage of using point

contact Andreev reflection comes from the surface modification due to the possible surface oxidation or chemical contamination on the surface of the sample [78].

Table 3.1 Fermi-level spin polarisation and resistivity of Mn-Ga films measured by point contact Andreev reflection [76][77].

Film stack	Spin polarisation (%)	Resistivity ($\mu\Omega$cm)	Magnetisation (kAm^{-1})
Pt/Mn_3Ga [77]	58	160	110
MgO/Mn_2Ga [76]	40	120	470

As shown in Table 3.1, $D0_{22}$ Mn_3Ga epitaxial films grown on a Pt(001) seed layer exhibit 58% spin polarisation at the Fermi level (E_F). It may be possible for thin films with higher order parameters to exhibit a higher value of spin polarisation that is closer to the predicted value. In addition, various magnetic and electronic properties, including net magnetisation and density of states, can be different depending on the position of Mn vacancies in non-stoichiometric alloys. The spin polarisation measured in $D0_{22}$ Mn_2Ga thin film is significantly lower than that of Mn_3Ga, at only 40% [77]. Furthermore, the electrical resistivity of $D0_{22}$ Mn_3Ga and Mn_2Ga are measured to be 160 and 120 $\mu\Omega$cm, respectively, both of which are close to the minimum metallic conductivity [77].

Tetragonal Heusler alloys of the Mn-Ga compounds have been identified as very promising in the context of high density spin torque memory and future integrated logic circuits [72]. In addition, another area of potential application of Mn-Ga thin films relates to the phenomenon of exchange bias. It has been found that hexagonal $D0_{19}$ Mn_3Ga thin films exhibit a large exchange bias [67], which is a potential candidate used to pin the fixed layer in MTJs and spin valve stacks. Our own result shown in Chapter 7 also support this finding. Hence AF Mn_3Ga thin films have potential in spin electronic devices. In this work, hexagonal $D0_{19}$ Mn_3Ga thin films have been successfully fabricated. Their magnetic and structural properties characterisation will be discussed in the Chapter 7.

3.6 Mn_3Ge

The magnetic and structural properties of Mn_3Ge is very similar to Mn_3Ga. The Mn_3Ge Heusler compound was first synthesised in a $D0_{19}$ hexagonal crystal structure. It shows AF ordering with a very weak ferromagnetic (F) component, the small magnitude of F component was attributed to the free rotation of the spin triangle in the basal plane caused by a small distortion of the hexagonal structure [79]. According to Qian *et al.* [79], the neutron diffraction of $Mn_{3.1}Ge_{0.9}$ indicated a triangular antiferromagnetic structure with magnetic moments lying in the hexagonal basal plane. It has been reported that hexagonal Mn_3Ge compound has a high Néel temperature of 390 K. Figure 3.9 shows XRD scan of hexagonal Mn_3Ge powder at room temperature. The inset is the crystal structure as a projection of the basal plane and 3D of the unit cell, Mn atoms is indicated in blue spheres, Ge atoms in green spheres.

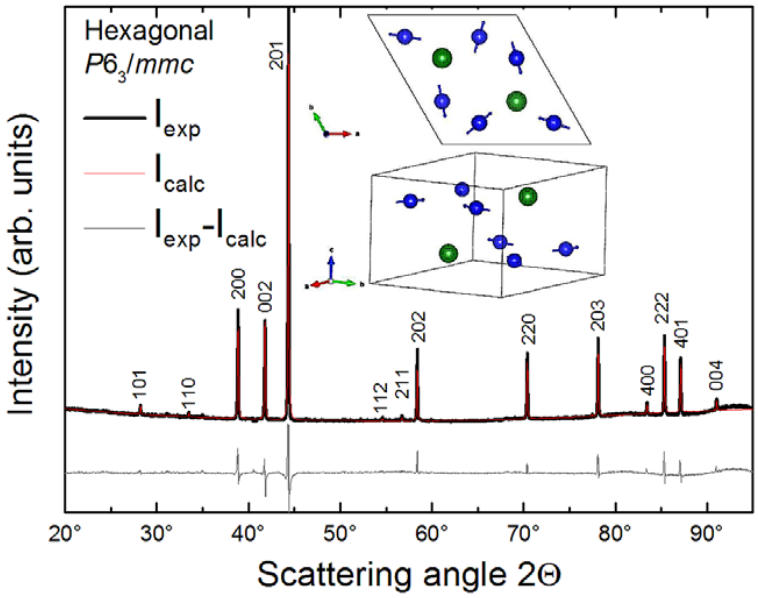

Figure 3.9 XRD scan of the hexagonal Mn_3Ge powder at room temperature [79].

The $D0_{22}$ tetragonal Mn_3Ge thin films have been reported to have a large perpendicular magnetic anisotropy and tunnelling magnetoresistance [80]. It is believed that AF ordered hexagonal Mn_3Ge is a potential material for spintronics applications due to its exchange bias behaviour up to room temperature [79].

Chapter 4

Magnetic Properties in Thin Films

4.1 Magnetic Anisotropy

Magnetic anisotropy has a strong impact on the shape of the hysteresis loop; that is, the way in which the magnetisation changes from zero to saturation magnetisation value M_s. By understanding the several factors that might influence the shape of the *M-H* curve, we will be able to understand the reason why the materials are magnetically soft or hard. Magnetic anisotropy can be understood as magnetic asymmetry in a system; the magnetic properties depend on the direction in which they are measured. There are three major types of anisotropy relevant to this work:

1. Shape anisotropy
2. Magnetocrystalline anisotropy
3. Exchange anisotropy

Magnetocrystalline anisotropy (also known as crystal anisotropy) is the only anisotropy intrinsic to the material; *i.e*. it depends on the atomic arrangement of the material. Shape anisotropy is extrinsic and originates from the geometry of the sample. The demagnetising field (H_d) of a single domain particle is proportional to the magnetisation M and is given by:

$$H_d = -N_d M \tag{4-1}$$

where N_d is the demagnetising factor of the sample.

Consider a specimen in the shape of a prolate spheroid as an example as shown in Figure 4.1.

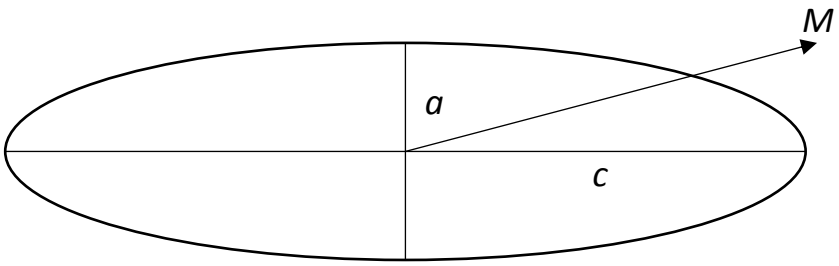

Figure 4.1 Prolate ellipsoid with semi-major axis *c* and semi-minor axis *a*.

If the sample is spherical, the same applied field will magnetise it to the same degree in all directions, *i.e.* shape anisotropy is zero. However, if the shape is not spherical, it will be easier to magnetise the sample along a long axis (*c*) because the short axis (*a*) has a larger demagnetising field. The shape anisotropy constant K_s is given by:

$$K_s = \frac{1}{2}(N_a - N_c)M^2 \qquad (4\text{-}2)$$

where N_a and N_c are the demagnetising factor along the a and c axes.

In this study, the samples were thin films which have no free poles at the surface of the grain. Therefore the shape anisotropy has only a small effect on the films. Hence in this study we only consider magnetocrystalline anisotropy and exchange anisotropy.

4.1.1 Magnetocrystalline Anisotropy

The origin of magnetocrystalline anisotropy is the spin orbit (L-S) coupling in the crystal lattice. The magnetocrystalline anisotropy acts like a magnetic field which holds the magnetisation of a domain in an easy direction. Let us assume in a single crystal with a cubic structure, a disk is cut parallel to the {110} plane as shown in figure 3.2 has direction along <110>, <111> and <100>. The magnetic measurements along these three directions are shown in figure 4.3 for iron and nickel.

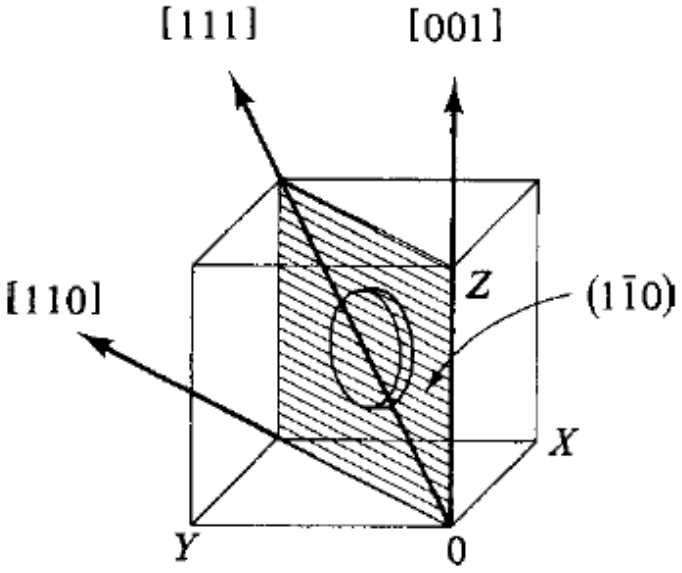

Figure 4.2 Three principle crystallographic directions in the $(1\bar{1}0)$ plane of a cubic crystal [135].

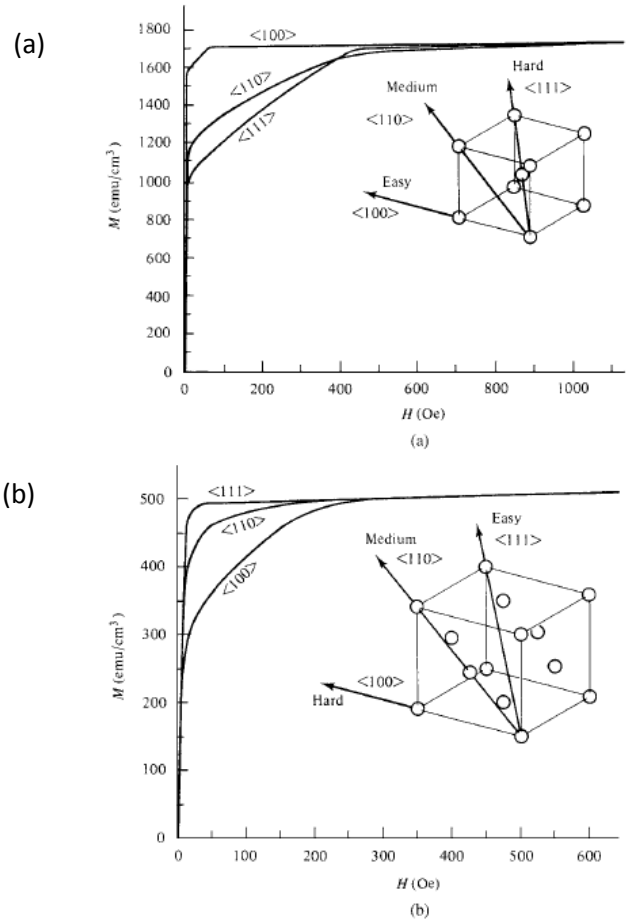

Figure 4.3 *M-H* curve for single crystals of iron (a) and nickel (b) [135]

Iron can be easily magnetised in the <100> direction which can be indicated as its "easy direction". Whereas the <111> direction needs a much larger applied field to reach saturation. Hence this direction can be indicated as its "hard direction". In nickel, the easy direction of magnetisation is <111>. In this study, antiferromagnetic Mn_2VSi has a face centred cubic structure with easy axis along the <110> direction. When atoms are bonded together the orbital angular moment of the electron is fixed. The spin angular moment of the electrons is coupled by spin orbit interaction and large applied fields are required to rotate the spin. The energy used to bias the magnetisation away from an easy direction is equivalent to the energy required to overcome spin-orbit coupling. This is called magnetocrystalline anisotropy energy E_K. In cubic crystals, E_K can be expressed in terms of a series expansion of the direction cosines α_1, α_2 and α_3 of M_s relative to the crystal axes.

$$\frac{E_K}{V} = K_0 + K_1(\alpha_1^2\alpha_2^2 + \alpha_2^2\alpha_3^2 + \alpha_3^2\alpha_1^2) + K_2(\alpha_1^2\alpha_2^2\alpha_3^2) + \cdots \qquad (4\text{-}3)$$

where V is the volume, $K_{0,1,2,\ldots}$ are anisotropy constants for a particular material at a given temperature and measured in the unit of erg/cm^3 (cgs). The strength of the anisotropy is measured by the magnitude of the anisotropy constants K_1, K_2, etc. Due to the fact that K_0 is independent of angle and K_2 is too small, both first and third terms in this expression can be neglected. This leaves K_1 as a dominated term which gives the energy per unit volume in order to flip the saturation magnetisation.

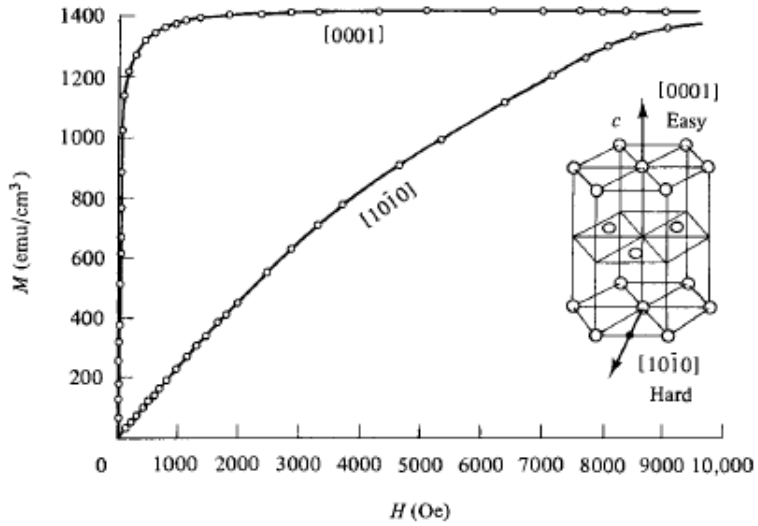

Figure 4.4 *M-H* curve for single crystals of cobalt.

In hexagonal crystal structures such as cobalt shown in Figure 4.4, the easy axis of magnetisation is along the *c* axis. All other basal directions are found to be hard axes. In this study, antiferromagnetic Mn_3Ga has a hexagonal crystal structure with easy axis along the [0001] direction. Hence, the anisotropy energy is only dependent on a single angle θ_s between M_s and the *c*-axis, *i.e.* uniaxial. The expression for E_K is

$$\frac{E_K}{\mathrm{V}} = K_0 + K_1 sin^2\theta_s + K_2 sin^4\theta_s + \cdots \qquad (4\text{-}4)$$

When K_1 and K_2 are positive the uniaxial crystal can be easily magnetised along the *c*-axis. When K_1 and K_2 are negative, the minimum value of E_K occurs at $\theta_s = 90°$.

Hence the easy direction lies in the direction of the basal plane perpendicular to the *c*-axis. When K_1 and K_2 are of opposite sign, this creates an easy cone of magnetisation.

4.1.2 Exchange Anisotropy

Exchange anisotropy was discovered by Meiklejohn and Bean [52] in 1956. Single-domain particles of cobalt were partially oxidised and as the result, each ferromagnetic (F) cobalt particle was coated with a layer of antiferromagnetic (AF) cobalt oxide. A hysteresis loop was then measured when the sample was field-cooled using liquid nitrogen at 77 K as shown in Figure 4.5. When the sample was field-cooled the magnetisation curve was shifted towards the negative field. If the sample was cooled in the zero field, the loop was symmetrical as shown in the dashed line of Figure 4.5 because the moments of the particles are randomly arranged, there is no net bias.

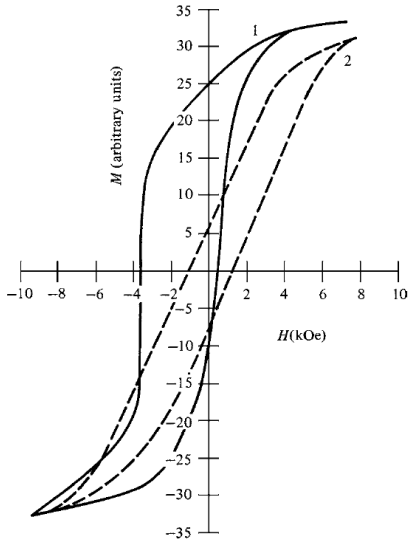

Figure 4.5 *M-H* curve of Co/CoO segregated particles measured at 77 K. Loop (1) field-cooled measurement. Loop (2) cooled in the zero field [52].

This phenomenon is due to the exchange coupling between the spins of ferromagnetic Co and antiferromagnetic CoO at the interface between two layers. Above the Néel temperature T_N of CoO, the CoO spins were paramagnetic and the spins in the single domain Co particles were aligned parallel to each other. When a positive field is applied and the sample cooled to $T < T_{\mathrm{N}}$, the spins of CoO aligned antiparallel to each other and become antiferromagnetic. The spin of Co near the interface are strongly exchange coupled to the CoO which leads to the spins in Co lying parallel to the spins in CoO, *i.e.* a unidirectional anisotropy. It is relatively easy to align the spins in a positive field, *i.e.* a smaller field is required, however in order to overcome the coupling, a larger opposite field is required as shown in Figure 4.6.

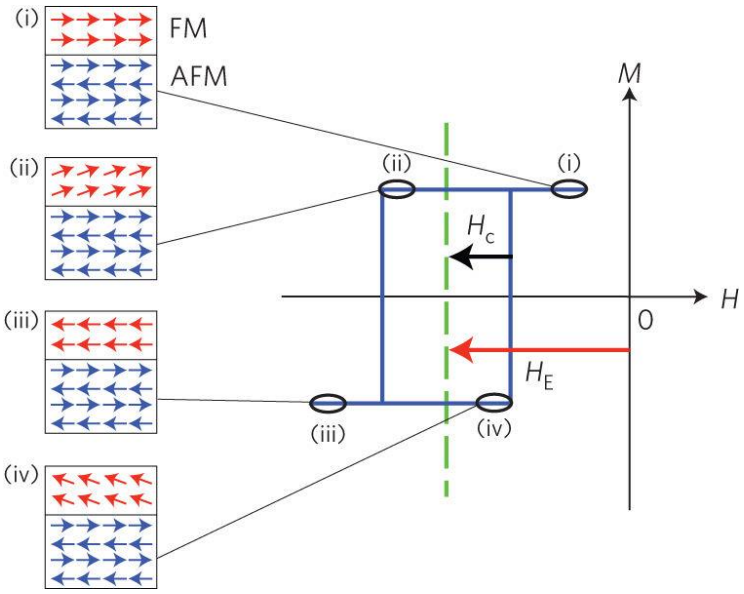

Figure 4.6 Classic model of exchange bias [52].

There are three important conditions for exchange anisotropy to appear in a system:

1. Thermal activation below T_N, where the AF layer can be aligned in antiparallel.
2. A sharp interface between the F/AF layers in order to allow for exchange coupling. Exchange bias has been observed in a nanoparticles [52].
3. Strong magnetocrystalline anisotropy in the AF to overcome the rotation of spins in the AF.

4.1.3 Texture in Polycrystalline Antiferromagnetic Films

There will be no net crystal anisotropy in a polycrystalline material if each grain is randomly oriented in space. However, in this study the texture of the thin film samples produced are highly dependent on the seed layer. For example (Chapter 7, page 121), $D0_{19}$ antiferromagnetic Mn_3Ga were deposited on a platinum seed layer under optimised conditions so that Mn_3Ga can be crystallised more easily in a preferred orientation, *i.e.* crystallographic texture. Hence the polycrystalline antiferromagnetic film will have an anisotropy dictated by each individual crystal. Texture of a film is induced depending on the shape and the formation of the crystallites. Thin film texture is strongly affected by the seed layer used. It has been found that the crystallisation direction of Mn_3Ga is along the (0001) plane which is parallel to the Pt(111) plane. The use of X-ray diffraction provides detailed information on the film texture which will be discussed in Chapter 6.

4.2 Domain Structures in Thin Films

Magnetic domains are regions in a magnetic material within which the magnetisation direction is uniform. The boundaries between two regions where the spontaneous magnetisation has different directions are known as domain walls. Domains form in a magnetic material to minimise the magnetostatic energy of a single domain configuration. The magnetostatic energy is induced by the demagnetising field which is in the opposite direction to the magnetisation. In a single domain state, the magnetostatic energy per unit volume is defined as:

$$E_{ms} = \frac{1}{2} N_d M_s^2 \tag{4-5}$$

where $N_d = \frac{4}{3}\pi$ (cgs), hence the magnetostatic energy per unit area on the top surface of the crystal,

$$E_{ms} = \frac{2}{3}\pi M_s^2 L \tag{4-6}$$

where L is the thickness of the domain. The magnetostatic energy is large in a single domain particle. By introducing a 180° domain walls E_{ms} is reduced but also leads to an increase in the domain wall energy. A 180° domain wall refers to the space between

two domains with opposite spins where the spins gradually rotate from one direction to the opposite direction over a certain distance. For example, to rotate the domain in a nickel crystal to its neighbouring domains with opposite magnetisations occurs over 290 atoms as shown in Figure 4.7, giving an angle between spins of 0.62°/ atom.

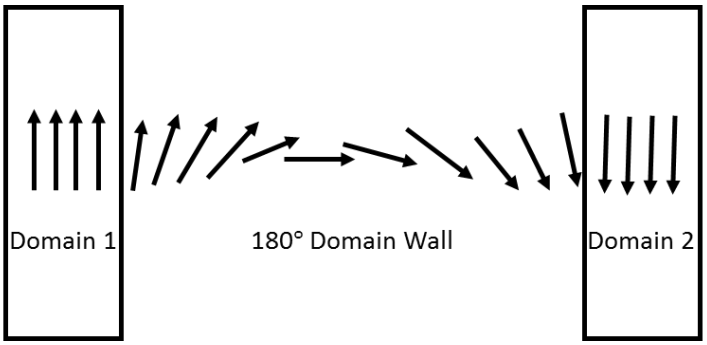

Figure 4.7 A schematic diagram of 180° domain wall.

If the material has a weak uniaxial anisotropy, the structure may form closure domains. E_{ms} is completely eliminated when the domains form a 90° closure as shown in Figure 4.8(c) however this increases the anisotropy energy.

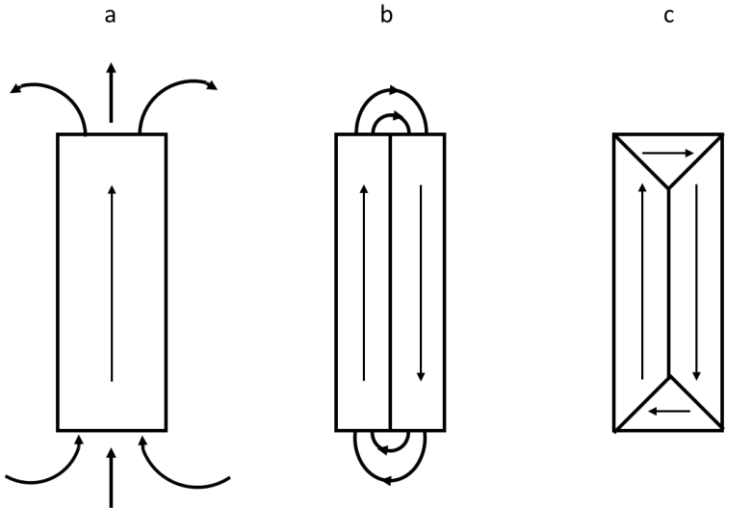

Figure 4.8 (a) Domain formation in a saturated magnetic field of the single domain state. (b) 180° domain wall formed to split single domain into two with opposite direction. (c) 90° closure domain wall formation leads to eliminate the E_{ms}.

Therefore by splitting the domains into smaller domains will reduce E_{ms} and more domain walls are formed. Further division of the domain is limited by the exchange

energy required to create the domain wall. Exchange energy is minimised by broadening the domain walls so that the spins rotate in small angles over a series of atoms. This is given by:

$$E_{ex} = 2A_{es}\cos\left(\frac{d\emptyset}{dx}\right) \tag{4-7}$$

where $A_{es} = n_A J_{ex} S_i S_j / L_p$ is the exchange stiffness, n_A is the number of atoms per unit cell, L_p is the lattice parameter. $\frac{d\emptyset}{dx}$ is the rate of change of spins rotation over a series of atoms.

On the other hand, anisotropy energy tends to make the spins flip abruptly in order to maintain the spins along the direction of an easy axis. The size of the domain and the domain wall thickness are dictated by the magnetostatic energy, exchange energy and anisotropy energy. Bloch was the first to theoretically examine the structure of a domain wall in 1932 [81]. The thickness of domain walls is given by

$$\delta = \pi\sqrt{\frac{A_{es}}{K_u}} \tag{4-8}$$

where K_u is the anisotropy constant of material. The complexity of domain walls rises as a result of the competition of the multiple energies. This is also true in polycrystalline thin films because of the direct exchange interaction between grains with varying easy axis orientations.

4.3 Stoner-Wohlfarth Theory

When we are considering the domain rotation process in a single domain particle based on the assumptions that there is no thermal activation (T=0) the moments are fixed along an easy axis direction and the Stoner-Wohlfarth theory is the simplest model to explain the behaviour. This model was introduced by Stoner and Wohlfarth in a classic paper in 1948 [82]. When the moment of a single domain particle is moved away from an easy direction by an applied field, it will rotate against the restoring force of the anisotropy.

Consider a single domain particle with an ellipsoidal shape as shown in Figure 4.9. The applied field is at an angle α biased from the easy axis and the saturation magnetisation M_s is at an angle θ_s from the easy axis.

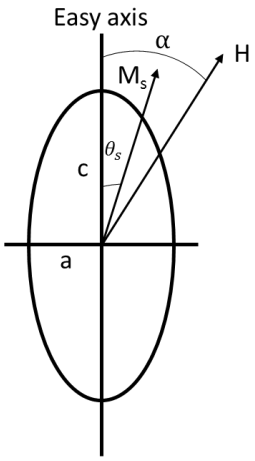

Figure 4.9 Ellipsoid single domain particle with the c axis as the easy direction.

The total energy E_T of the system consists two components *i.e.*, the anisotropy energy and the field potential energy. The anisotropy energy E_K is given by:

$$E_K = K_1 sin^2\theta_s \tag{4-9}$$

The field potential energy is given by:

$$E_P = -HM_s\cos(\alpha - \theta_s) \tag{4-10}$$

The total energy E_T is the sum of two terms:

$$E_T = K_1 sin^2\theta_s - HM_s\cos(\alpha - \theta_s) \tag{4-11}$$

The equilibrium position of the moment direction is obtained when the differentiation of E_T with respect to θ_s is equal to zero:

$$\frac{dE_T}{d\theta_s} = 2K_1 sin\theta_s cos\theta_s - HM_s \sin(\alpha - \theta_s) = 0 \qquad (4\text{-}12)$$

Since the component of the magnetisation in the field direction is given by:

$$M = M_s \cos(\alpha - \theta_s) \qquad (4\text{-}13)$$

and assume that the field *H* is perpendicular to the easy axis, $\alpha = 90°$. Then,

$$m = \frac{HM_s}{2K_1} \qquad (4\text{-}14)$$

where $m = \frac{M}{M_s}$ is the normalised magnetisation. Equation (4-14) indicates a linear relationship between the magnetisation and the field when the applied field *H* is normal to the easy axis.

The direction of the applied field *H* has a significant impact on the switching field. If the field is perfectly aligned along the easy axis, *i.e.* $\alpha = 0°$, the magnetisation will only flip over to the opposite direction when *H* reaches a threshold value in the opposite direction. A small deviation of the applied field from the easy axis induces a torque on M_s which leads to a rotation. In the case of a deviation of $10°$ this leads to a 30% reduction in the switching field as shown in Figure 4.10.

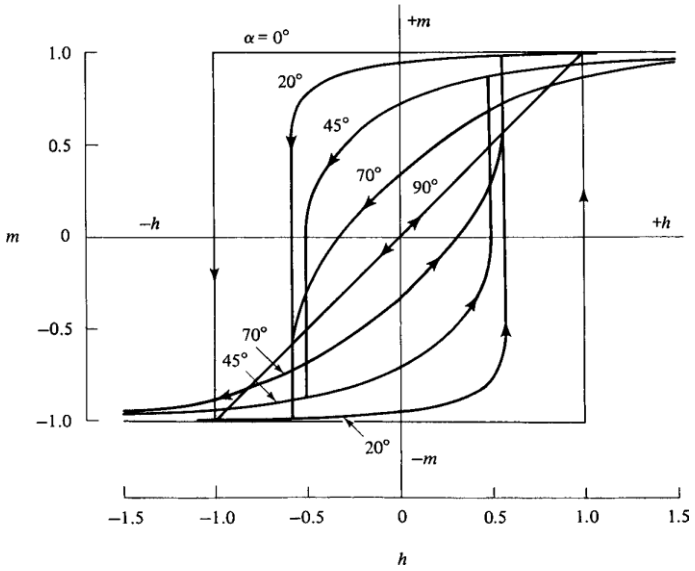

Figure 4.10 Hysteresis loop for single domain particles with uniaxial anisotropy. h is the normalised field H/H_k[135].

In the antiferromagnetic polycrystalline films studied in this work, the AF grain sizes are relatively small < 20 nm and are believed to contain a single AF domain. In addition they are known to be non-interacting and, hence, the Stoner-Wohlfarth model explains the process of coherent reversal of the grains in the film.

4.4 Exchange Interaction in Thin Films

The exchange interaction is essential for understanding the ordering of magnetic states in materials. In diamagnets and paramagnets there is no exchange interaction between the individual moments and each moment acts independently. In ferromagnets, antiferromagnets and ferrimagnets the exchange interaction between neighbouring atoms will force the individual moments into parallel or antiparallel alignment with each other. Pierre Weiss' postulated a molecular field model to explain the alignment between magnetic moments in solids, which should be responsible for the spontaneous magnetic order.

$$H_{mol} = N_{mol}M \tag{4-15}$$

where H_{mol} is the molecular field, M is the magnetisation and N_{mol} is the molecular field constant. However, the strength of the alignment was estimated to be of order

10^7Oe which is much larger than any manufactured field [83]. Hence the mechanism of the strong exchange interaction lies not only in magnetic interaction but also electronic interaction.

In this section three major types of exchange interaction will be discussed:

1. direct exchange
2. indirect exchange
3. superexchange

4.4.1 Direct Exchange

In order to understand direct exchange interaction, there are two key principles that must be known; Coulomb repulsion between electrons and the constraints imposed by the Pauli Exclusion Principle.

Coulomb repulsion describes the force between interacting charged particles. The force of interaction is attractive if two particles have opposite signs and repulsive if both have the same signs. The Pauli Exclusion Principle states that two identical particles cannot occupy the same quantum state in a system simultaneously.

The direct exchange interaction can be described by the quantum mechanical exchange force introduced by Heisenberg in 1928 [84]. The interaction takes place between moments, which are close enough to have sufficient overlap of their wave functions. The wave functions of these two atoms will overlap and minimise the total energy. In the case of two atoms with spin angular moment S_j and S_i, the exchange energy between them is derived from effective spin Hamiltonian

$$E_{ex} = -2J_{ex}\underline{S_i}\underline{S_j} \qquad (4\text{-}16)$$

where J_{ex} is the exchange integral. The Bethe-Slater curve shows that the sign of J_{ex} for transition metals is controlled by the r_a/r_{3d} ratio where r_a is the radius of an atom and r_{3d} is the radius of the $3d$ shell of electrons as shown in Figure 4.13. The ordering in antiferromagnetic materials is dictated by direct exchange. According to Pauli's exclusion principle, the spin states are forced to be in the opposite direction when the value of J_{ex} is negative. This gives rise to antiparallel alignment (antiferromagnetic) as shown in Figure 4.11.

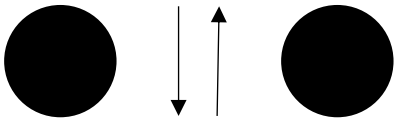

Figure 4.11 Antiparallel alignment of spins

If the atoms are separated by a large distance the electrons tend to move away from each other in order to minimise the repulsion between two electrons. This increases the r_a/r_{3d} ratio and hence increase the value of J_{ex} (positive). Therefore the parallel alignment (ferromagnetic) is formed when electrons share the same wave function but are confined to separate regions of space as shown in Figure 4.12.

Figure 4.12 Parallel alignment of spins

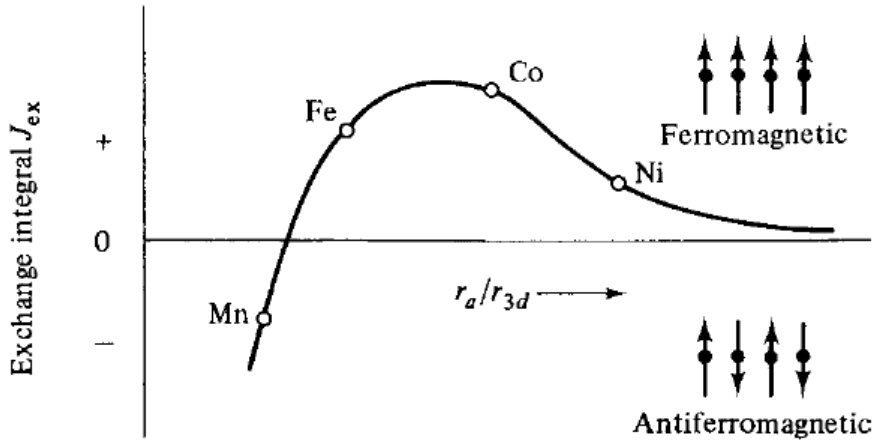

Figure 4.13 Bethe-Slater curve[135]

Finally, when the atomic separation becomes larger, electrostatic interactions become negligible and the energy difference between parallel and antiparallel spin arrangement disappears and hence there is almost no direct exchange interaction.

4.4.2 Indirect Exchange

When the interatomic distance is large the exchange coupling constant J_{ex} decreases dramatically as shown in Figure 4.14. In the case of rare-earth metals and alloys, the magnetic moment is determined by the partial filling of highly localised 4f transition states. The probability for an electron to hop from a 4*f* state at one site to another site is small. In consequence the direct exchange interaction is too weak for ferromagnetism to occur in rare earth materials with large interatomic distances. The origin of indirect exchange comes from the local magnetic moment spin-polarising the conduction electrons which align nearby moments. The indirect exchange coupling 'constant' *j* oscillates with a damped amplitude between the positive and negative value as the separation between atoms increases. This concept was introduced by Ruderman and Kittel (1954) [85], Kasuya (1956) [86] and Yoshida (1957)[87] and is known as the RKKY interaction. This coupling is weaker than direct exchange and superexchange in 3*d* metals and magnetic oxides.

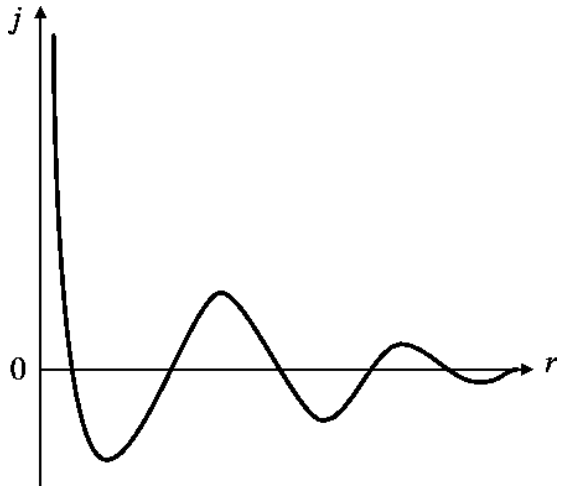

Figure 4.14 Variation of the indirect exchange coupling constant *j* of a free electron gas in the neighbourhood of a point magnetic moment at the origin *r*=0 [143].

4.4.3 Superexchange

Superexchange is a special type of the RKKY interaction which describes the interaction between moments on ions too far apart to be connected by the direct exchange, but coupled over a relatively long distance through a non-magnetic material. It occurs in oxides and nitrides of transition metals due to the bonding between the transition metal 3*d* orbits and 2*p* orbits in O or N. The doubly occupied *p* orbital has two electrons with opposite spins. The *p* state has spin-up and spin-down electrons concentrated in lobes of 180° apart while *d* state has opposite spins concentrated in lobes every 90° rotation about the ion. The *p* orbital on O can exchange an electron with each 3*d* orbital on the transition metals. As shown in Figure 4.15, this produces antiparallel alignment between the two transition metals atoms. It is a mechanism which leads to antiferromagnetism. It also leads to sheet AF structure. Superexchange also occurs in ferrites such as Fe_3O_4 but these are uncompensated materials and so have a net magnetic moment. In this work, the superexchange interaction does not occur in our samples as there is no oxygen or nitrogen present in the antiferromagnetic Heusler alloy.

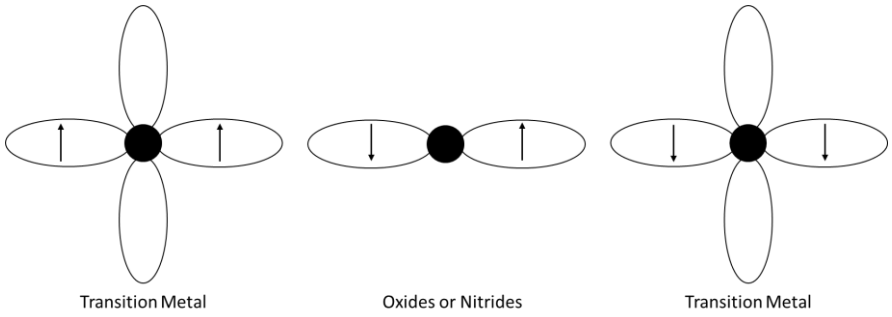

Figure 4.15 Superexchange interaction between transition metals and oxides or nitrides.

Chapter 5

Exchange Bias

The successful design of magnetic structures for spintronic applications is predicated upon the capability to manipulate and control magnetic properties. In heterostructures, the exchange coupling of a ferromagnet (F) and antiferromagnet (AF) produces a ferromagnetic behaviour characterised by stable order and high anisotropy, and the loop shift occurs when the antiferromagnetic order is established in the presence of the ferromagnet. Since AF is only weakly coupled to the external field, it keeps a history of the F direction at the time when the AF order was set. Noteworthily, this holds even when the magnetisation of the F is reversed in terms of its direction. In such a structure, the anisotropy may behave in a unidirectional manner, and this loop shift behaviour is commonly referred to as exchange bias. In the last decade, due to the importance of the phenomena of loop shift, which serves as a useful feature for controlling the magnetic properties in devices, a basic and quantitative understanding of exchange bias has started to emerge.

In this work, the interface between Mn_2VSi/CoFe and Mn_3Ga/CoFe has been studied. Using the York Model of exchange bias [14], both revealed exchange bias under 100 K. In this chapter, the earlier models of exchange bias are explained, and detailed information about the York Model is then discussed.

5.1 Theories and Models of Exchange Bias

The advancement of knowledge with respect to the phenomenon of exchange bias has been relatively slow for the following reasons. Firstly, since exchange bias is the consequence of a complex interfacial exchange interaction between the AF and F materials, the interface embedded between the F and AF layers is characterised by low volume. This means that it is difficult to separate its contribution from that of the F layer [88]. Secondly, the experimental apparatus for dealing with the interfacial interaction at the atomic scale has only become available in recent years.

Over the past four decades, various attempts have been made to explain the phenomenon of exchange bias by constructing theoretical models. However, even with the aid of these models, knowledge about the particulars of the phenomenon is far

from thorough, but it is still the case that exchange basis has been regularly applied in the context of spin valve structures. In addition, after the 1998 identification and application of giant magnetoresistance (GMR) in several devices, including hard disk drive (HDD) read heads [9], researchers were afforded with a valuable chance to illuminate and enhance the magnetic pinning mechanism, particularly with respect to thin film structures characterised by flat interfaces.

5.1.1 Meiklejohn-Bean Model

As briefly discussed in Section 4.1.2, Meiklejohn and Bean proposed the earliest model of exchange bias in 1956 [52]. These researchers suggested that the origin of the loop shift can be attributed to a large anisotropy in the AF and the phenomenon of a weak exchange energy coupling between F and AF. As shown in Figure 5.1 (a), the magnetic moments of F and AF align along the saturating magnetic field direction (at a temperature above T_N). When the temperature falls below T_N and a small negative field is applied, the magnetisation of F is still pinned along the original direction, as shown in Figure 5.1 (b). When a negative field is increased in such a way as to overcome the interlayer exchange energy, the magnetisation of F flips to the opposite direction, as shown in Figure 5.1 (c). The ideal model is valid under the following assumptions:

- The F layer rotates rigidly;
- F and AF are both considered to be single domain entities;
- The interface is smooth at the atomic scale;
- The AF layer is magnetically rigid to the external field;
- Spins of AF interface are fully uncompensated;
- The AF layer has an in-plane uniaxial anisotropy.

Hence, the interfacial energy is given by the following equation:

$$E_{\text{int}} = -HM_s t_F \cos\theta_s - J_{\text{int}} \cos\theta_s + K_F \sin^2\theta_s \qquad (5\text{-}1)$$

where H is the applied field, t_F is the thickness of the F layer, M_s is the saturation magnetisation of F, K_F is uniaxial anisotropy of F, J_{int} is the interfacial coupling constant, and θ_s is the angle between the easy axis and magnetisation direction.

During the reversal process, the F magnetisation flips back to the original direction while the field is still in negative direction.

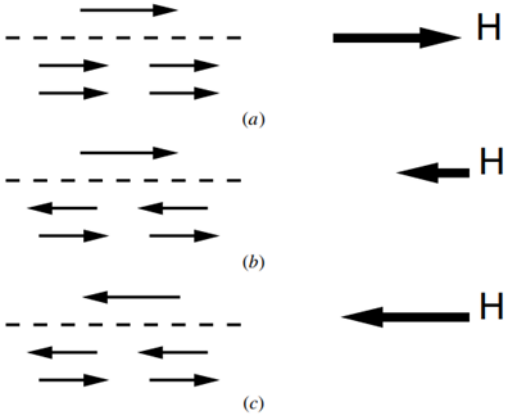

Figure 5.1 Meiklejohn-Bean model for exchange bias [144].

The exchange bias of the field is given as follows:

$$H_{ex} = \frac{J_{int}}{M_s t_F} \tag{5-2}$$

The value obtained from equation (5-2) is two orders of magnitude higher than the value obtained experimentally in small-grain polycrystalline films. Therefore, this model fails to predict a reasonable value for H_{ex}.

5.1.2 Néel's Antiferromagnetic Domain Wall

In order to explain the loss in exchange bias compared to the predicted value, one can assume that a partial domain wall in the AF layer during magnetisation reversal process will form. This idea was proposed by Néel in 1967 [89]. In the general concept, there is no demagnetising field in AF, thus meaning that the domains cannot be formed (as mentioned in Section 4.2). However, in exchange biased materials, the F layer provides sufficient magnetostatic energy to AF to form domains. The AF domain wall stores an important fraction of the exchange coupling energy, thereby lowering the

shift of magnetisation curve. In addition, Néel also took interface roughness into account, which indicated that AF sub-lattices would be present at the interface. This resulted in the partial compensation of AF moments, and as a result of the spins at the interface of each grain in polycrystalline, AFs were statistically distributed. Consequently, fluctuations in the moment of AF grains were produced. Importantly, Néel's model failed to predict the value of H_{ex}.

5.1.3 Fulcomer-Charap Model

A fundamental step forward took place regarding the incomplete understanding of exchange bias with the publication of the Fulcomer-Charap model [90]. After conducting theoretical and experimental investigations into exchange bias within permalloy films, the researchers found that exposure to acid vapour resulted in the progressive oxidisation of nickel in the alloy, thus giving rise to AF grains on the film surfaces. Significantly, Fulcomer and Charap noticed that incremental changes in the exchange bias of these systems occurred regarding, firstly, the grain size, and secondly, the number of grains within the AF material. Following the application of a granular reversal model (comparable to a Stoner-Wohlfarth system), numerical modelling yielded results consistent with the experimental outcomes. Most notably, the two researchers estimated that the exchange field resulting from the F/AF bilayer would yield thermally-activated alterations in orientation of the AF sub-lattices, thus bringing about a change in H_{ex}.

A foundational attribute of the Fulcomer-Charap model is the fact that numerous particle dimensions within the AF material are taken into consideration, thus enabling a broad range of anisotropy and coupling energies. The assumption made within the model regarding the particle size distribution is that up to a given maximum (after which no more particles exist), every value is as likely to arise as every other value. In view of this, the researchers discovered the importance of taking into consideration a distribution of particle size, but the precise form of the distribution was not consequential.

In view of these features, as noted in the study conducted by Grimsditch *et al*.[91], it was possible for the Fulcomer-Charap model to yield an accurate prediction of the temperature dependence of H_{ex} and H_c over a broad spectrum of temperatures (even

greater than T_N). For this reason, the Fulcomer-Charap model constitutes the foundation of numerous granular models which centre around thermal fluctuation effects. As a case in point, by drawing on the temperature dependence of the coupling outlined in the Fulcomer-Charap model, Nishioka *et al*. were able to examine the temperature dependence of exchange bias in NiFe/FeMn and Co/CrMnPt [92]. As another more recent example, Xi [93] sought to investigate the dependence of the blocking temperature (T_B) in exchange bias bilayers, and the thermal fluctuation model the researcher developed in view of this was based on the Fulcomer-Charap model. Some of Xi's noteworthy findings are as follows: firstly, that for large-grain systems, a monotonic rise in H_{ex} in conjunction with AF layer thickness (t_{AF}) can be observed; secondly, that with measurement time, T_B decreases linearly; and thirdly, that with the T_N of AF grains, T_B increases linearly. Xi's model is particularly noteworthy since it represents a broad extension of the Fulcomer-Charap model, in such a way as to illuminate a comprehensive account of thermal effects. Nevertheless, its limitation is that the calculations pertain to single-grain volume, thus meaning they cannot offer an account of real systems.

5.2 The York Model of Exchange Bias

5.2.1 Energy Barriers

According to Brown [94], thermal energy causes the magnetic moment of a single domain particle to vibrate about the equilibrium position. The magnetic moment reverses its orientation when the thermal energy is larger than the anisotropy energy barrier. The reversal of the moment of a grain has a relaxation time given by the Néel-Archenius law:

$$\tau^{-1} = f_0 \exp(-\frac{\Delta E}{k_B T}) \qquad (5\text{-}3)$$

where τ is the relaxation time in which the magnetisation decays to $1/e$ of its initial value; f_0 is the attempt frequency of the magnetic moment, $f_0 \sim 10^9 - 10^{12} s^{-1}$; and ΔE is the energy barrier. For a relaxation time of 100 s, $\Delta E = 25 k_B T$. In addition, for a magnetic recording device, the capability must exist to store the information for 10 years, which results in a higher energy barrier of $40 k_B T$.

For the purpose of determining the energy barrier required to reverse the magnetisation, it is necessary to consider a simpler case of perfectly aligned single domain nanoparticles, under the assumption that the easy axis and the magnetic field are in a state of alignment. In this context, the system exhibits a perfectly square hysteresis loop, and as outlined in the previous chapter, the anisotropy energy and field potential energy are included in the total energy related to the reversal process. In addition the system has two stable states when the magnetisation is in a state of alignment or, alternatively, when it rests in the opposite direction to that of the magnetic field. Furthermore, it is necessary for the switching field to be greater than the energy barrier (ΔE), which refers to the disparity between the system's minimum and maximum energy state. Here, ΔE can be expressed in the following way:

$$\Delta E = KV(1 - \frac{H}{H_K})^2 \qquad (5\text{-}4)$$

where H_K represents the anisotropy field, which in turn determines the system's maximum coercivity of the system; V is the particle grain; and K is the anisotropy constant. It should be noted that while the above equation (5-3) is used to describe a single particle, real systems involve a distribution of particle volumes and anisotropies. Therefore, the energy barrier turns into a distribution, $f(\Delta E)$. More information about the particle size distribution is given in Section 5.3.4.

With respect to the York Model of exchange bias, this is based on the single domain behaviour of the AF grains within a sputtered thin film. In view of this, by implementing identical structures as those given previously, it is possible to express the energy barrier for a single domain AF grain in the following way:

$$\Delta E = \mathrm{K}_{AF} V(1 - \frac{H^*}{H_K^*})^2 \qquad (5\text{-}5)$$

where H^* is the exchange field from the F layer acting on the AF layer, and H_K^* is the pseudo-anisotropy field in AF. Here, it is important to recognise that the value of $\frac{H^*}{H_K^*}$ is assumed to be small. This is valid for low F thickness < 5 nm in a CoFe system [95].

5.2.2 Time Dependence

The time dependence of magnetisation is known as the magnetic viscosity, which refers to a postponement in the magnetisation response to an applied field attempting to switch it. The logarithmic relationship between magnetisation (M) and time (t) was first expressed in the study conducted by Street and Woolley [96].

$$M(t) = \text{constant} + \text{Sln}\left(\frac{t}{t_0}\right) \tag{5-6}$$

where S is the magnetic viscosity coefficient. Here the magnetic viscosity coefficient is defined as the rate of change of magnetisation with ln(t). In addition, in the event that the magnetic field is increasing, S is positive when the magnetic field is increasing. Furthermore, S can be expressed by Gaunt's [97] formula.

$$\text{S} = \frac{d\text{M}}{d(\text{ln}t)} = 2\text{M}_\text{s}k_\text{B}\text{T}f(\Delta\text{E}_\text{C}) \tag{5-7}$$

where T is the temperature, M_s is the saturation magnetisation of the ferromagnet, and (ΔE_C) is the critical value of the energy barrier. In an AF material, there is no net magnetisation, thereby meaning that the order of the AF is chosen as an analogous for the magnetisation in the F. In this context, S can be expressed in the following way:

$$\text{S} = \frac{d\text{M}_\text{AF}}{d(\text{ln}t)} = 2\text{P}_\text{s}k_\text{B}\text{T}f(\Delta\text{E}_\text{C}) \tag{5-8}$$

where P_s is the saturation value of the order of the antiferromagnetic. For an AF grain in a polycrystalline thin film, the critical value of the energy barrier is determined by the grain volume distribution, the temperature dependence of K_AF, and the setting temperature. In the study conducted by Gaunt *et al*. [97], the findings indicated that the linear dependency on ln(t) constitutes a unique instance in which $f(\Delta E(t))$ is constant over the measurement period. Hence, it is true in those cases where the energy barrier distribution is broad.

5.2.3 The Setting Process

In a disordered AF, grains are randomly orientated. Thus, the setting process is pertinent, since it refers to the mechanism by which order is induced in the AF layer. The setting process derives its name from the fact that an ordered AF is designated as "set". The setting process was applied to the AF grains by heating below the Néel temperature (T_N), thereby ensuring that the structural features of the sample remained intact. As a consequence of this process, the AF grains – in the process of becoming thermally active – were aligned by the exchange field from the closest F layer. The time dependency of the exchange bias for the IrMn/CoFe systems (utilised as this research's reference) was observed, as indicated in Figure 5.2 [98]. The step increase in the exchange bias in reference to the temperature increase can be accounted for by the switching of additional 'free'spins in the population.

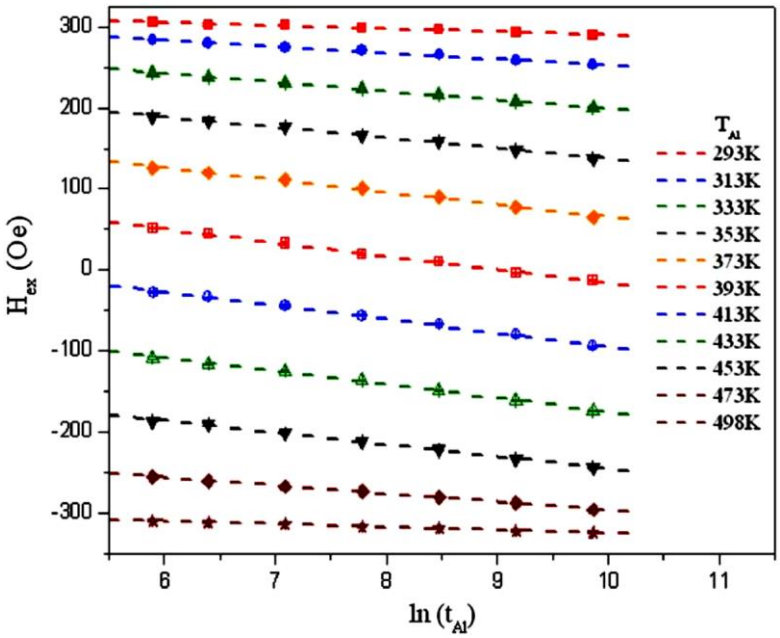

Figure 5.2 Time dependence of the exchange field with ln(t) [98].

The magnetic viscosity (S) is determined by the gradient of the linear fits in Figure 5.2:

$$S = 2P_s k_B T f(V_{act}) \qquad (5\text{-}9)$$

where V_{act} is the volume of a grain which overcomes the energy barrier at a given temperature. P_s is the saturation value of the order of the antiferromagnetic.

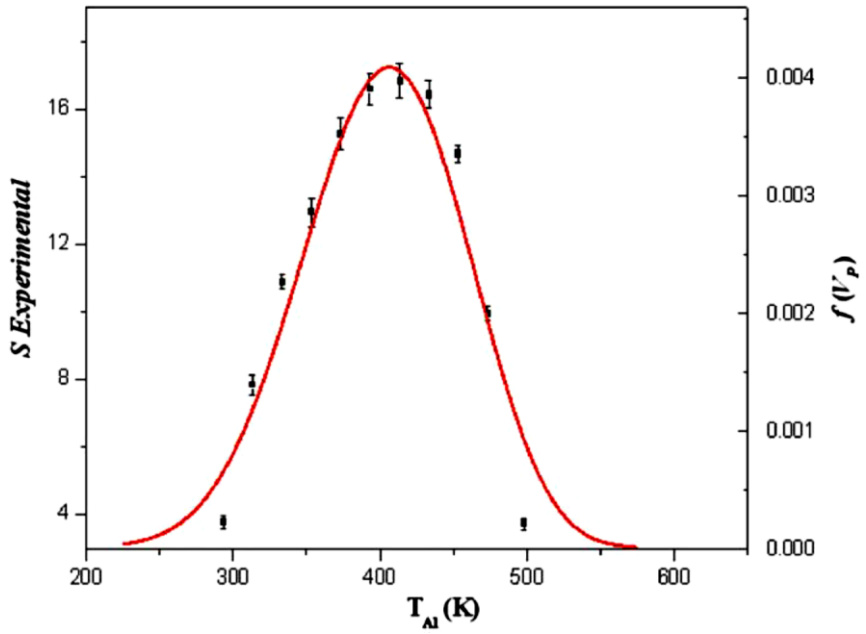

Figure 5.3 Experimental and calculated magnetic viscosity as a function of T_{set} [98].

Figure 5.3 illustrates the magnetic viscosity as a function of setting temperature. The initial expectation was that variance should arise with respect to both ends of the temperature spectrum. This prediction was made in response to the fact that more significant ambiguities in the value of S would result from the negligible number of grains at either side of the grain size distribution.

5.2.4 Grain Volume Distribution

The setting process time dependence, as well as the degree to which the small AF grains were thermally unstable, indicated that a pair of critical volumes existed inside an AF grain volume distribution. As indicated in Figure 5.4, V_c represents the lower grain volume limit (where values below this mean that thermal instability does not produce exchange bias), while V_{set} represents the upper grain volume limit (where values higher than this mean that the thermal energy is insufficient to induce setting in the AF grains).

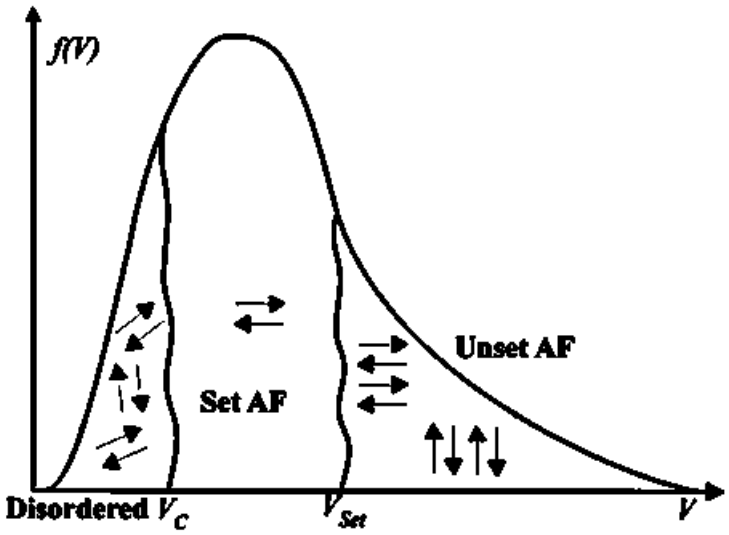

Figure 5.4 Schematic diagram of the AF grain volume distribution with critical volume V_c and V_{set} [98].

Based on the Néel-Arhenius law, presented in equation (5-3), along with an awareness of the AF grains' relaxation time, it is possible to calculate the critical volumes through algebraic manipulation of the equation. V_{set} refers to the upper grain volume limit, which it is possible to set in the time t_{set} at the temperature T_{set}. Thermal instability is a characteristic of those grains which are overly small, and it is the case that the behaviour of grains of this kind will imitate superparamagnetic particles of an F material. In addition, exchange bias is not impacted by these grains, and they are orientated at random.

$$V_{set} = \frac{k_B T_{set} \ln(f_0 t_{set})}{K_{AF}(T_{set})} \tag{5-10}$$

$$V_c = \frac{k_B T_{measure} \ln(f_0 t_{measure})}{K_{AF}(T_{measure})} \tag{5-11}$$

where the measurement temperature and measurement time are represented by $T_{measure}$ and $t_{measure}$, respectively.

In view of the above, it is possible to regard the exchange bias as proportional to the fraction of the grains which lie between the specified limits:

$$H_{\text{ex}} = C \int_{V_c}^{V_{set}} f(V)\, dV \tag{5-12}$$

where *C* denotes the stiffness of the interfacial coupling between the AF and F layers. It is important to note that although the determinants of *C* are not defined comprehensively, the evidence suggests that these relationships operate in an independent way from the degree of alignment in the AF grain they are derived from.

In sputtered polycrystalline films, the grain diameter distribution is log-normal, which stems from the way in which growth takes place (see Figure 5.5). With respect to the York Model of exchange bias, it is possible to derive the grain size distribution from the grain size measurements, which can be undertaken by taking TEM images of the sputtered films. The samples measured using TEM in this work are grown using HiTUS plasma sputtering system.

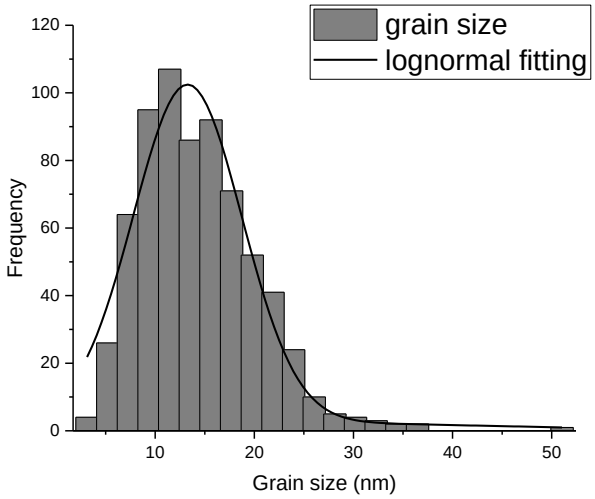

Figure 5. 5 Grain size distribution for a 6-nm thick Mn_3Ga thin film sample.

5.2.5 The Blocking Temperature

In the research conducted by Fulcomer and Charap [5], it was demonstrated that the switching of AF grains, comparable to the superparamagnetism that occurs in small F particles, can occur as a result of thermal fluctuations. As an extension of the points

made previously in Section 4.2.4, the behaviour of AF grains can fall into one of the following categories: firstly, unstable grains; secondly, blocked grains; or thirdly, unset grains. With respect to the process by which grains are classified, this is undertaken in a way that relates to the measurement timescale, thereby ensuring that the small grains, with minimal energy barriers and thermal energy, can undergo reversal in the course of measurement. As for grains which are larger, these are blocked, and it is possible for them to maintain their orientation in the course of the measurement process. Regarding unset grains, these are characterised by the greatest energy barriers, and the likelihood of these grains undergoing switching far surpasses the length of the measurement process. In the context of polycrystalline films, all three grain behaviours can be observed owing to the nature of the grain distribution. Prior to the York Protocol (see the next paragraph), scientists took measurements of blocking curves at increasingly high temperatures, thus facilitating an exchange bias amounting to zero. In addition to this, based on the data derived from the York Model, the temperature at which observations of zero exchange bias were recorded was the blocking temperature of the grain characterised by the greatest energy barrier. Therefore, the logarithmic time dependence of the AF changes were the determining factor for these measurements. Furthermore, it should be noted that measurements conducted in reference to the York Protocol are performed at T_{NA} (namely, the temperature of no activation). The justification for this is because for systems in which thermal activation is absent, the T_{NA} is a standard temperature. Chapter 6 presents a full discussion of the process by which T_{NA} can be measured.

The previously mentioned York Protocol, applied by Fernandez-Outon *et al.* [13], refers to the measurement process by which outcomes can be replicated which are not dependent on the experimental timescale. At the outset of the process described in the York Protocol, it is first necessary to set the antiferromagnet (see Section 6.3.2). This further necessitates the selection of a temperature, which should be based on an empirical consideration of the temperature which will ensure that the greatest possible number of grains are characterised by instability. Here, it should be noted that the setting process cannot set all grains, since a certain number of grains will remain unstable. Researchers should avoid excessive increases in temperature, since overly-high temperatures can cause layer inter-diffusion [14], thus damaging the films (or,

alternatively, surpassing the boundary conditions of the cryostat in the magnetometer). Hence, a 90-minute setting time has been chosen for setting the grains. Following this, the change of exchange field H_{ex} with t_{set} is less than 1%, which ensures the reproducibility of the H_{ex} value.

As shown in Figure 5.6, the York Model measures the median blocking temperature of the Mn_3Ga AF material.

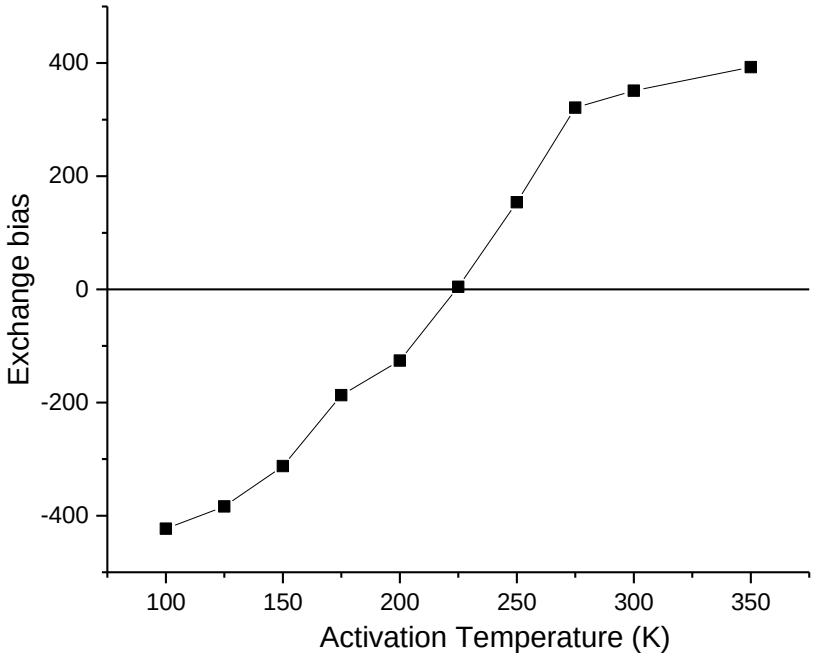

Figure 5.6 Temperature dependence of exchange bias measured for the Mn_3Ga (6 nm)/$Co_{0.6}Fe_{0.4}$ (3.3 nm) films

The exchange bias is zero at the median blocking temperature. As the activation temperature increases, the magnetisation curves shift towards the positive field. When past the zero point, the exchange bias will increase until all the grains are set in the opposite direction to their initial position. When exchange bias is zero, the volume of AF grains oriented in one direction is equal to those initially oriented in the opposing direction.

5.2.6 The Anisotropy Constant

The anisotropy constant can be calculated from the blocking temperature distribution [99]. A fraction of the total number of grains is aligned in one direction after setting the field at T_{set}. Following this, the F layer is saturated in the opposite direction, and under the applied field T_{act} is maintained for the sample. This ensures that a component of the antiferromagnet is reversed to bring about the opposite direction. Consequently, the largest grains switch, thereby facilitating the derivation of the exchange bias value. The value of H_{ex} measured after the activation step is given by:

$$H_{ex}(T_{act}) \propto \int_{V_{act}}^{V_{set}} f(V)dV - \int_{0}^{V_{act}} f(V)dV \tag{5-13}$$

$$V_{act} = \frac{k_B T_{act} ln(f_0 t_{act})}{K_{AF}(T_{act})} \tag{5-14}$$

where V_{act} is the volume of the largest grain to be thermally activated.

When T_{act} equals the median blocking temperature, $<T_B>$, the exchange bias becomes zero. This occurs at the median volume, $<V>$, of the grain size distribution. By rearranging equation (5-14), the anisotropy constant is obtained:

$$K_{AF}(< T_B >) = \frac{k_B < T_B > ln(f_0 t_{set})}{< V >} \tag{5-15}$$

5.2.7 Grain Volume and Film Thickness Dependence

Many reports have stated that the magnitude of the exchange bias changes in response to the thickness of the AF layer [100][101][102]. This was also found to be the case for Mn_3Ga Heusler alloys in the present study. The exchange bias, H_{ex}, is reported to increase as the thickness of the AF layer increases, and when the thickness of the AF layer reaches a certain value, the exchange bias starts to show an inverse relationship with the increasing AF thickness, where parameter n is in a range from 0.3 for FeMn [103] and 1 for CoO [104].

$$H_{ex} \propto \left(\frac{1}{t_{AF}}\right)^{n} \tag{5-16}$$

Vallejo-Fernandez *et al*. [105] calculated the exchange bias as a function of the AF grain diameter, as shown in Figure 5.7. The solid red curve is a theoretical fit of the experimental data calculated using equation (5-12). When the AF layer thickness is less than 6 nm, a large proportion of small grains are thermally unstable, thereby meaning that they do not contribute to the exchange bias. As the thickness increases, the exchange bias rises correspondingly, until the largest fraction of the grains is within the interval set by the two critical volumes. The way in which the AF grain volume distribution corresponds to different layer thicknesses is shown in Figure 5.9. This was achieved by applying an empirical and accurate statistical method.

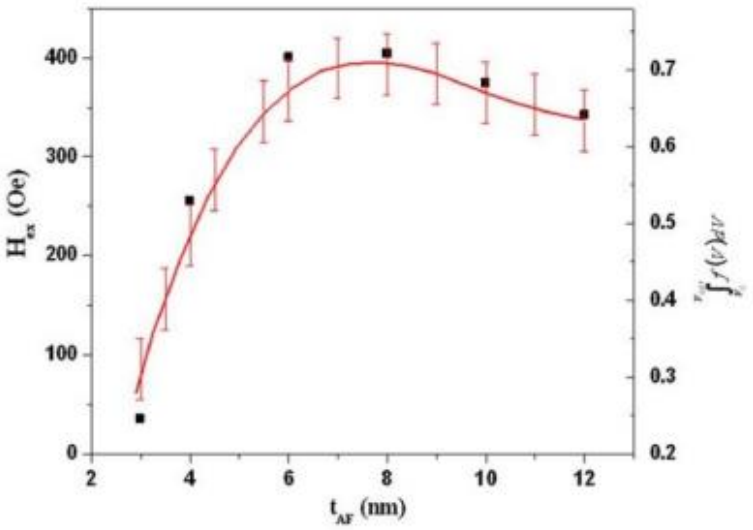

Figure 5.7 Variation of exchange bias with AF thickness [105].

Figure. 5.8 indicates that it is possible for the exchange bias to rise or fall in relation to grain size, and this is based on the AF layer thickness. Specifically, the value of the measured exchange bias rises with grain diameter in the event that AF thicknesses range from 4-6 nm, while the exchange bias goes through a maximum in the event that the AF layer thickness is 12 nm. As for AF layer thicknesses which exceed 12 nm, numerous grains satisfy the need for stable volume, but if they are overly-large, it is not possible for them to be aligned by the setting process. Consequently, H_{ex} falls. This phenomenon has also been proved by our work in Mn_3Ga heusler alloys.

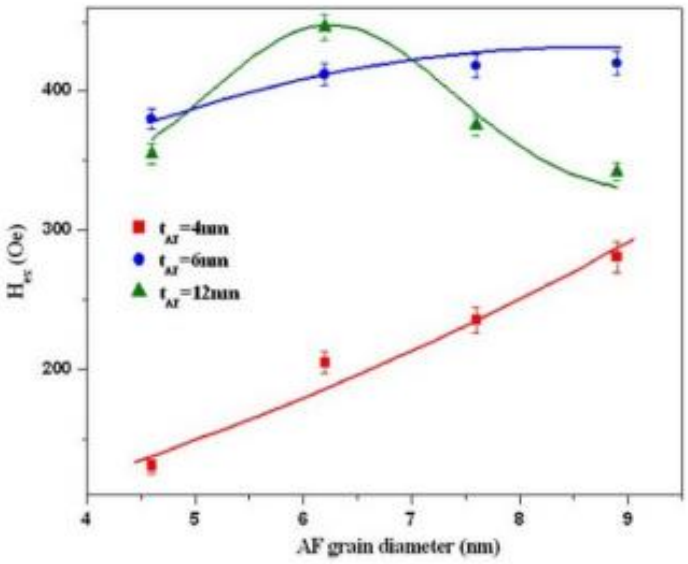

Figure 5.9 Variation of the exchange bias with antiferromagnetic grain diameter [105].

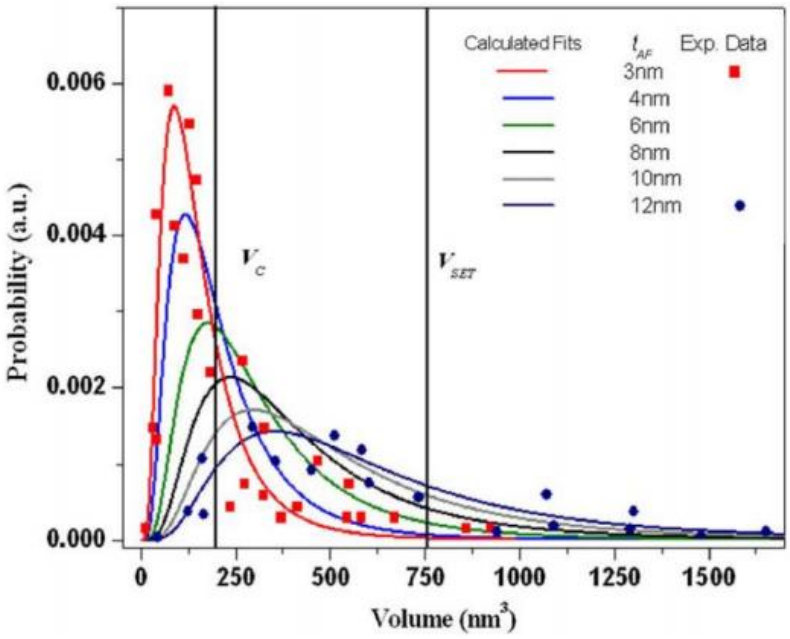

Figure 5.8 Grain volume distribution for varying thicknesses of IrMn [105].

Chapter 6

Experimental Techniques

In this chapter, detailed information of experimental equipment and techniques which have been used during the study is given. There are three major categories introduced in this chapter; thin film fabrication, sample structure characterisation and magnetic characterisation. All the polycrystalline Heusler alloy thin film samples were produced using High Target Utilisation Sputtering (HiTUS). A Rigaku SmartLab X-ray diffractometer and a JEOL 2011 Transmission electron microscopy (TEM) were used for structral analysis of the samples. A JEOL JSM-5910LV scanning electron microscope (SEM) was used to measure the composition of the antiferromagnetic material. A Microsense Model 10 vibrating sample magnetometer (VSM) and Surfaces/Interfaces: microscopy (SIM) beamline were used for magnetic properties characterisation.

6.1 Thin Film Deposition

A wide range of deposition techniques can be used to deposit metallic thin films resulting in single-crystal and polycrystalline films. There are two main technologies used in thin film deposition: evaporative methods and glow-discharge processes. Evaporative technology is one of the oldest techniques used for depositing thin films. Its mechanism depends on thermal evaporation or vacuum evaporation. A typical example of such is molecular beam epitaxy (MBE), which is designed for producing single-crystal epitaxial films in a high vacuum below 1.3×10^{-11} mbar. The thin films are slowly deposited by evaporating the target source onto a single-crystal substrate at an appropriate temperature. The film thickness, uniformity, lattice match and composition etc. are finely controlled by the fast shutter which intercepted the molecular beam between the target sources and the substrates. The major advantage of MBE is the low temperature requirement for film expitaxy. However its complex operation and low product throughput are the major limitations of MBE for production applications.

Another technology is glow-discharge processes. One well known example is plasma sputtering where the surface atoms are ejected from the target source by a high density

plasma beam. In this work, plasma sputtering technique was used for polycrystalline Heusler alloy thin film growth which is described in the following section 6.1.1.

6.1.1 High Target Utilisation Sputtering (HiTUS)

The thin film samples studied in this work were grown using the process of High Target Utilisation Sputtering (HiTUS), manufactured by PlasmaQuest Ltd. HiTUS is a technique that requires the use of an independent plasma source to generate a high-density plasma on the target surface. High purity Ar gas is injected into the chamber via an Argon gas feed. With approximately 95% of the target surface being exposed to the plasma, the result is increased material flux that results in enhanced durability, hence extending the target's lifespan. The speed at which HiTUS films can grow is dependent on the proximity of the substrate to the target; typically, the distance between them is 300 mm and the rate of growth Mn_2VSi, Mn_3Ga and Mn_3Ge are approximately 0.7Å/s, 0.9 Å/s and 0.8 Å/s respectively. The material sputters in a conical profile, which contributes to the growth rate. The relatively large separation between substrate and target causes the isolation of the substrate from the plasma beam, preventing re-sputtering and complications such as silicon becoming implanted in the Heusler alloy. Films produced by this method are uniform, polycrystalline structures that can be compared in terms of their properties to films used in data storage industries.

There are numerous advantages offered by the HiTUS system that can facilitate the creation of numerous film structures. Alloys are especially suitable for HiTUS sputtering because the whole surface of the target is eroded, which allows for a near matched stoichiometry between the thin film and the powder metallurgy target. Complex multilayer structures can be formed because the target carousel can be loaded with up to 8 individual targets meaning the vacuum does not have to be broken between the changes of targets. A further advantage is provided by the substrate carousel that can be loaded with up to 6 substrates, each of which can hold a single 20 mm x 20 mm substrate or four 5 mm x 5 mm substrates, both with TEM grids. In order to produce high quality thin films, a high vacuum environment is needed. It takes approximately three hours for the turbo molecular, rotary and cryo-pumps to reach a pressure of 5×10^{-7} mbar; combining this factor with the rate of sputtering means a full growth session can be completed in 8 hours. These pumps are controlled by a Programmable Logic Controller (PLC).

As shown in Figure 6.1, a Faraday cage surrounds a quartz tube in which a 2.5 kW, 3-turn copper radio frequency antenna is situated. This forms the HiTUS side arm that generates the plasma from argon gas, coupled inductively to the 13.56 MHz radio frequency field. Through a process of ambipolar diffusion [106], plasma ion beams are propelled into the main chamber by a launch magnet and are directed to the target surface by a steering electromagnet. The applied field of the launch and steering electromagnets are approximately 50 Oe and 500 Oe. Although the plasma's ion density of $10^{12} – 10^{13}$ ions/cm^3 is high, the ion energy at the target surface of < 10 eV which is too low to be adequate for sputtering [107]. Therefore, the plasma is coupled to a DC bias voltage to increase the ion energy.

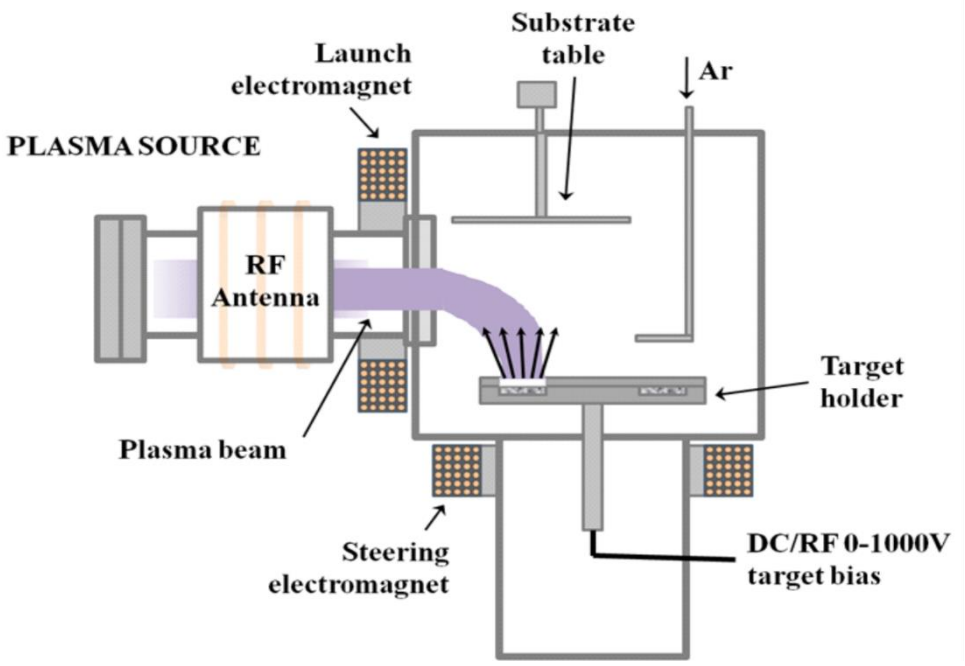

Figure 6. 1 Schematic diagram of the HiTUS system [108].

Control of sputtering parameters is necessary for the comparison of the properties of thin films. There are three ways to control the sputtering rate: Gas flow rate, DC bias voltage and RF power. By modifying the argon gas flow rate, which in turn alters the plasma pressure and deposition energy, the mean free path of ions and film density are changed. Hence sputtering rate is varied directly. Initial control of the ion energy can be achieved by setting the launch radio frequency power between 1 and 100% of 2.25

kW capacity. The ion energy can also be controlled in the chamber at the target surface by applying a DC bias voltage. A range of negative DC voltages from 0 to 1000 V can be applied to the target. These parameters are also able to adjust the mean grain diameter of the film, which is valuable in interpreting magnetic measurements[108]. Before film deposition, surface contaminants can be removed from the substrates by disabling the steering electromagnets, engulfing the main chamber with ions of < 30 eV [108].

At present, the University of York is the only institution that uses the HiTUS process to grow Heusler alloys, the results of which have been published in several papers [3,4]. In contrast to magnetron sputtered and MBE grown films that exhibit crystallisation in the as-deposited state, there is little or a total absence of crystallisation present in the samples of Heusler alloy films (such as Mn_2VSi in this studies) grown using the HiTUS system. Studies by Sagar and Fleet *et al*. [110] indicated that *ex situ* annealing of the films enabled large crystals (grains) to form from the as-deposited amorphous-like matrix. Grains measuring between 30 nm and 250 nm were discovered in Co_2FeSi films that had been annealed for up to 6 hours. Sagar *et al*. [109] propose that this phenomenon arises from nano-crystal nucleation in the as-deposited matrix seeding a layer-by-layer crystallisation.

The Heusler alloys grown in HiTUS required extreme annealing conditions. To promote grain size growth, an *in situ* annealing method has been used during deposition. In order to achieve high-temperature growth, a heater was installed inside the chamber directly above the substrates with a separation of approximately 7 mm. A stainless steel thermal couple (Labfacility, MI S/S Type K) was placed on the heater case, which was connected to the temperature reader as shown in Figure 6.2.

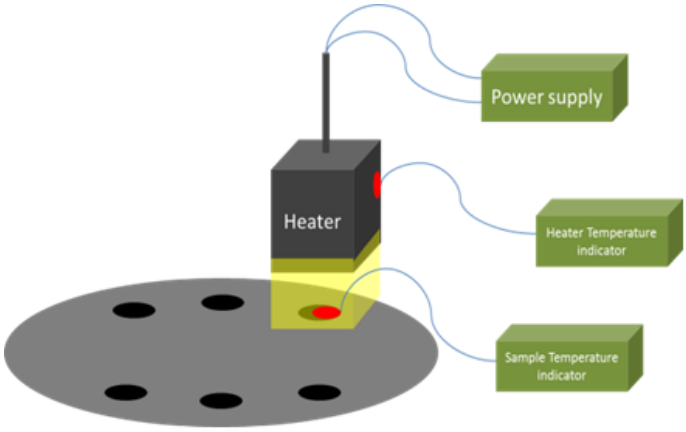

Figure 6.2 Schematic diagram of heater inside the chamber.

The heater was operated by illuminating a lamp (Philips, Halogen, 100 W) to increase the temperature of the back of the substrate. The power supply (ALDA, Model 00160141) controls the temperature, which can be heated up to approximately 730 ℃ (1003K). The heater was calibrated using an external thermocouple attached to the substrate to record the spontaneous temperature reading while the heater is operating. The heater temperature calibration is shown in Table 6.1. The overall performance of the heater was found to be stable, maintaining a temperature fluctuation range of approximately±12℃.

Table 6.1 Heater temperature fluctuation measurements.

Set-up temperature (℃)	Heater temperature (℃)
150	187±17
200	235±15
250	277.5±10.5
300	328.5±13.5
350	374.5±11.5
400	420±11

450	466±10
500	514±8

6.1.2 Sample Preparation

The substrate holder was made of machinable ceramic to prevent melting during high temperature *in situ* deposition. The substrates were 16×16 mm^2 square as shown in Figure 6.3. The sample can be then cut into the required sizes for later measurements using a diamond scriber.

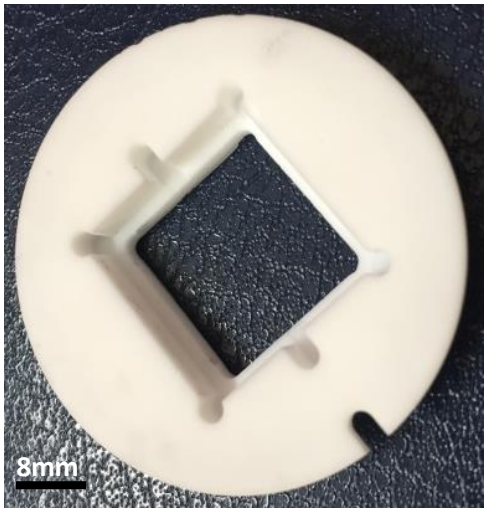

Figure 6.3 Ceramic substrate holder used in HiTUS for deposition.

Before the deposition, the Si substrates and substrate holders were cleaned in acetone and isopropanol using an ultra-sonic bath for 15 minutes to remove grease from the surface. They are then dried using nitrogen gas.

The loaded targets and substrates were further cleaned using the plasma before deposition. The targets are cleaned using 1000 V bias voltage plasma sputtering for approximately 2 minutes depending on the degree of contamination and oxidation. The substrates are then cleaned by Ar plasma for one minute with zero bias voltage and with the steering magnets turned off.

Before deposition, a 30 second conditioning and pre-sputtering was used to stabilize the Ar gas pressure and further clean the targets. The shutter is then opened and deposition started.

6.1.3 HiTUS Thin Film Thickness Calibration

The HiTUS system uses an INFICON XTM/2 deposition monitor to measure the thickness of the film during deposition. The device works by oscillating a piezoelectric quartz crystal at its electromechanical resonance. The resonance frequency is reduced when a small amount of material from the target is deposited onto the top of the crystal. The reduced resonance frequency is given by :

$$\frac{M_f}{M_q} = \frac{\Delta f}{f_q} \tag{6-1}$$

where M_f is the change in mass due to the deposition, M_q is the original mass of the quartz crystal, Δf is the change in resonance frequency and f_q is the uncoated resonant frequency of the crystal [111].

The thickness of the material deposited onto the film can be calculated using the Z-match equation (4-2)[112]:

$$t_{film} = \left(\frac{N_q \rho_q}{\pi \rho_f R_z f}\right) \arctan\left(R_z \tan\left[\frac{\pi(f_q - f)}{f}\right]\right) \tag{6-2}$$

where t_{film} is the thickness of the film, N_q is the frequency constant of the quartz crystal, ρ_q is the density of the quartz, ρ_f is the density of material, f is the resonant frequency of the loaded crystal and R_z is the Z-Factor of the film material.

6.2 Sample Structural Characterisation

Structural characterisation of a sample includes the grain size, crystal structure, layer sharpness and crystal orientation of the material. Two major apparatus were used for these measurements, an X-ray Diffractometer (XRD) and a Transmission Electron Microscope (TEM). XRD is an ideal equipment for scanning over a wide area and provide the average crystalline structural information across the sample. TEM allows one to accurately measure the grain size and orientation at the atomic scale. Both apparatus are discussed in the following sections.

6.2.1 X-ray Diffractometer

X-ray diffraction allow the identification of crystalline structure of the thin films, the principle of which can be explained by Bragg's law:

$$\lambda_{\mathrm{x-ray}} = 2d\sin\theta \tag{6-3}$$

where $\lambda_{\mathrm{x-ray}}$ is the X-ray wavelength. θ is the angle between the angle of incident and the scattering angle from the sample surface and *d* is the lattice spacing of the sample. There is variation between the types of lattice formation in a hexagonal or cubic structure. In this particular study, both cubic and hexagonal structures were investigated, where for the cubic case the lattice spacing can be described by the formula:

$$d = \sqrt{\frac{a^2}{h^2 + l^2 + k^2}} \tag{6-4}$$

where *a* and *c* are the lattice constant of the material and *h*,*k* and *l* are the Miller indices for a specific plane.

The lattice spacing for a hexagonal structure is given by:

$$\frac{1}{d^2} = \frac{4}{3}\frac{h^2+hk+k^2}{a^2} + \frac{l^2}{c^2} \tag{6-5}$$

Figure 6.4 shows a schematic diagram of the Bragg diffraction.

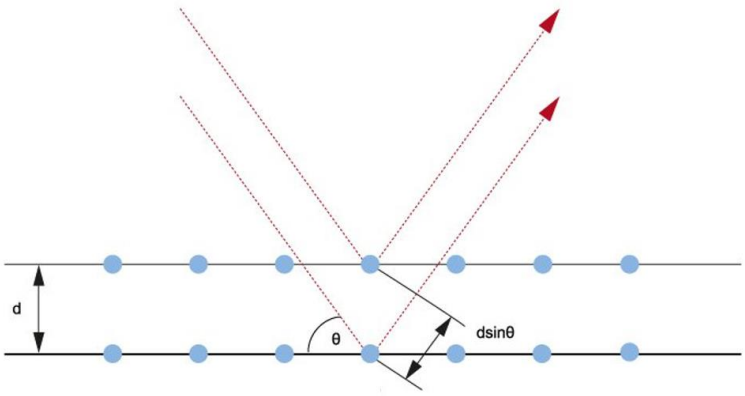

Figure 6.4 Schematic diagram of X-ray Bragg diffraction.

A Rigaku SmartLab X-ray diffractometer shown schematically in Figure 6.5 was used in this study. This apparatus employs a high intensity 9 kW rotating anode X-ray generator. It operates with a voltage of 45 kV and a current of 200 mA. Fluctuations in these two parameters were measured to only vary by ± 0.005%, with a 10% variation in power input.

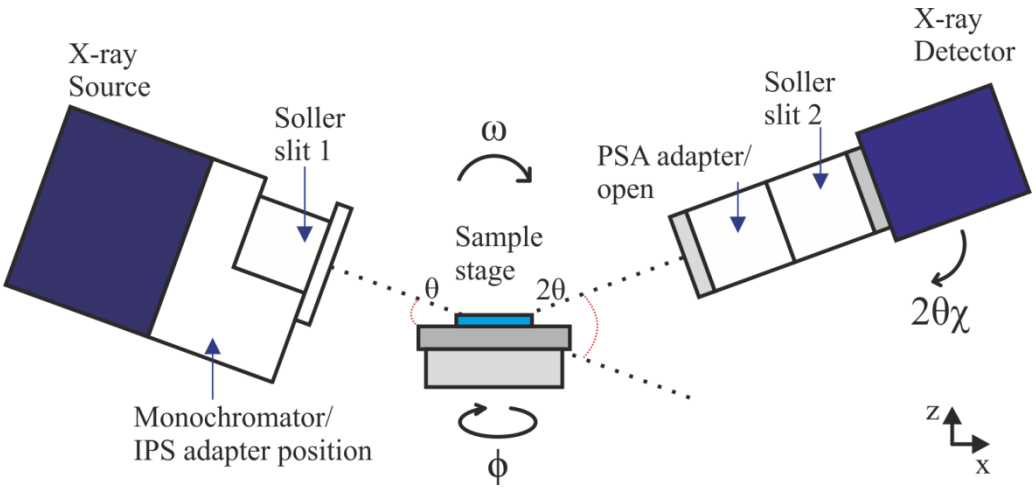

Figure 6.5 The Rigaku SmartLab X-ray diffractometer [128].

A Cu target was used as the X-ray source which generates a beam with $K\alpha_1$ and $K\alpha_2$ X-rays whose wavelengths are 1.541Å and 1.544 Å, respectively [113]. Germanium is used in the incident monochromater crystal system, which allows for the diffraction of X-rays. Ge(220)×2 crystals were fitted to produce monochromatic X-rays by diffracting them twice by the Ge(220) lattice planes. Passing X-rays through this crystal makes it possible to use only $K\alpha_1$ X-rays with approximately 0.003 degree divergence. As a consequence, the optimal measurement can be achieved using $K\alpha_1$ component. Soller slits and a PSA adapter were used to focus the electron beam.

The NaI scintillation counter collects all the reflected X-ray signals. When a charged particle strikes the scintillator, photons are emitted as its atoms are excited. The particles carrying charge are aimed at the photocathode of a photomultiplier tube. As a result, electrons are released by the photoelectric effect. These electrons are electrostatically focused so that they strike the first dynode of the tube. As a result of electrons hitting the dynode, a number of secondary electrons are released. These electrons also undergo acceleration and are directed to strike the next dynode. As shown in Figure 6.6, each subsequent dynode impact releases further electrons, and so there is a current amplifying effect at each dynode stage. Each stage is at a higher

potential than the previous to provide an accelerating field. The resultant output signal at the anode is in the form of a measurable pulse for each photon detected at the photocathode, and is passed to the processing electronics. The pulse carries information about the energy of the original incident radiation on the scintillator. Thus both the intensity and the energy of the radiation can be measured.

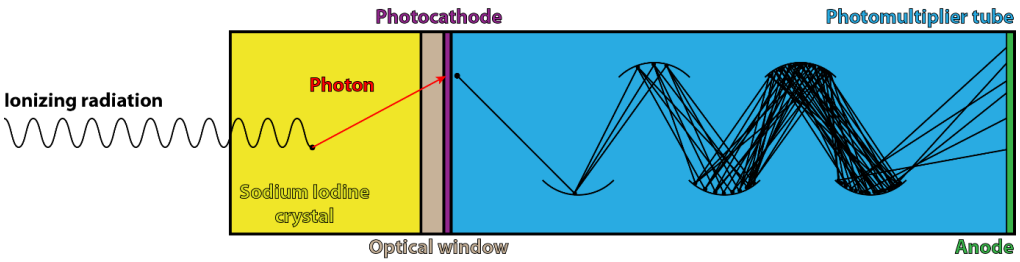

Figure 6.6 Schematic diagram of scintillating counter detector [145].

The Rigaku SmartLab XRD system utilises a goniometer, which includes a high resolution θ- θ closed loop which allows the X-ray source and detector to be positioned with a 0.001˚ step size. This loop is the element that provides the high level of accuracy and resolution θ-2θ scans. These θ-2θ scans rely on the detector being placed at an angle that is twice that of the incident angle of the X-ray. This measurement provides all the out of plane crystallographic information [113].

6.2.2 Pole Figure Measurement

Pole figure measurements have been used to analyse the distribution of the crystal orientations in the films. In materials science, texture is the distribution of crystallographic orientations in a sample. Where the crystallographic orientations are not random, the sample may be referred to as having a weak, moderate, or strong texture. This depends greatly on the proportion of crystals within a sample which display a preferred direction.

X-ray pole figures are the most widely known source of texture information due to its low cost and easiness to perform. It provides an average texture over a reasonably large surface area, in this study the typical sample surface is 25 mm^2. The average grain size in our films is smaller than 20 nm this means that hundreds of thousands of grains are contained in the measurement which ensures statistical viability.

The θ-2θ scan cannot describe the crystal texture accurately if a sample has a preferred orientation because the scan only measures planes perpendicular to the surface. Therefore we can describe the texture of a material by using pole figure scans. Pole figure measured with 4-axis goniometer in which 2 axes used to choose a specific crystallographic plane with $\theta - 2\theta$ a specified, hence to determine the Miller indices associated with the pole figure. The third axis tilts sample surface with respect to the focusing plane. The fourth axis rotates the sample about its normal.

A "rocking curve" is a short pole figure cut in one crystallographic direction where the profile width is a figure of merit for the degree of texture.

6.2.3 Reflectivity Measurement

X-ray reflectivity (XRR) measurement have been used to measure the density, interface roughness and thickness of Heusler alloy thin films. The principle can be explained using the total reflection phenomenon. When the incident angle is smaller than a critical angle total reflection occurs. Therefore, the intensity of the reflected X-ray is equal to that of the incident X-ray. When the incident angle is larger than the critical angle, both refraction and reflection occurred. This will lead to the intensity of the reflected X-rays to decrease. Hence an oscillation is observed in the intensity of the X-rays reflected from multilayered samples due to the interference between two reflected X-rays. The density, thickness and roughness of the thin film samples can then be determined from the incident angle and reflected X-ray intensity.

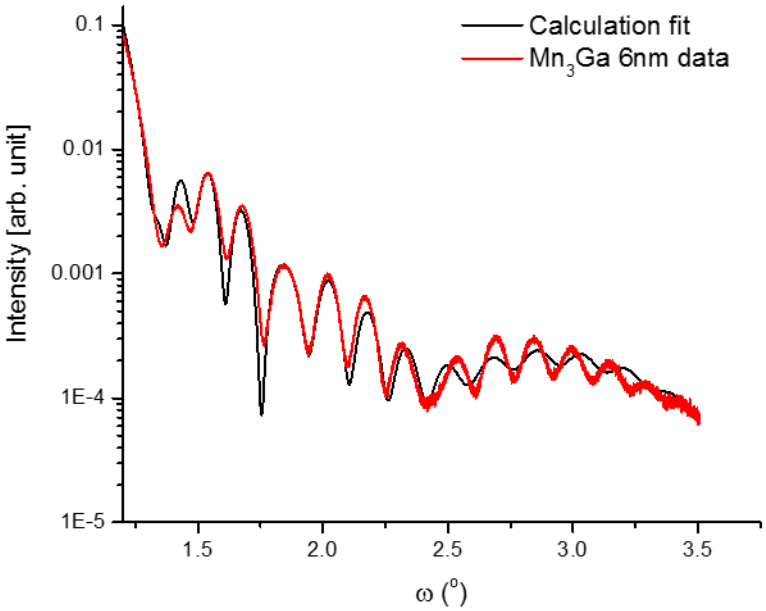

Figure 6.7 An example of a reflectivity scan of Mn_3Ga/CoFe multi-layer thin film.

From the reflectivity profile in Figure 6.7, the period of oscillation indicates the thickness of the layers. In general the amplitude of the oscillation indicates the difference in density and the degree of roughness between the substrate and each layers. By altering the parameters, the calculated fitting can match the measurement data giving the correct value for thickness, roughness and density of a multilayer sample. In this work GenX is used for reflectivity fitting. GenX is a multipurpose refinement program using a differential evolution algorithm. It was developed mainly for refining X-ray reflectivity and neutron reflectivity data [114].

6.2.4 Scherrer Analysis

Samples studied in this work were all polycrystalline where the diffraction patterns usually contain combination of amorphous, highly textured polycrystalline layers and single crystal substrate. Scherrer grain size analysis is a simple method to estimate the average grain size in a material from the width of a peak. In general, a sharp peaks (small full width half maximum) indicate large grains, whereas broader peaks indicate small grains. This is described by the Scherrer equation:

$$D = \frac{C\lambda_R}{\text{FWHM}\cos\theta} \tag{6-6}$$

where D is the grain diameter, C is a constant close to unity, λ_R is the wavelength of the radiation, θ is the Bragg reflection angle.

The broadening effect will ocuur when the Bragg reflection angle is large due to the inverse proportionality between the grain size and the diffraction angle.

6.2.5 Transmission Electron Microscopy

Transmission electron microscopy has been used to image the physical structure of the Heusler alloys thin film on an atomic scale. TEM employs electrons in order to 'see' a sample but since the electron have a much smaller wavelength than light means that an electron microscope can provide a much higher resolution than a light microscope. The human eye has a resolution of 0.1 to 0.2 mm and the Rayleigh principle explains the ability of a TEM to possess a resolution of 0.8 Ȧ:

$$\delta = \frac{0.61\lambda_R}{R^*\sin\beta} \tag{6-7}$$

where δ is the minimum distance can be resolved per radian, λ_R is the wavelength of the radiation, R^* is the refractive index of the view medium and β is the semi-angle of collection of the magnifying lens [115]. The refractive index is ~ 1 and the semi-angle is small, thus the resolution of light microscope is mainly determined by the wavelength of the radiation source. Taking green light as an example, its 550 nm wavelength gives 300 nm resolution. The wavelength of a 200 keV electron is about 4 pm, which provides 10,000 times better resolution than a visible light microscope [115].

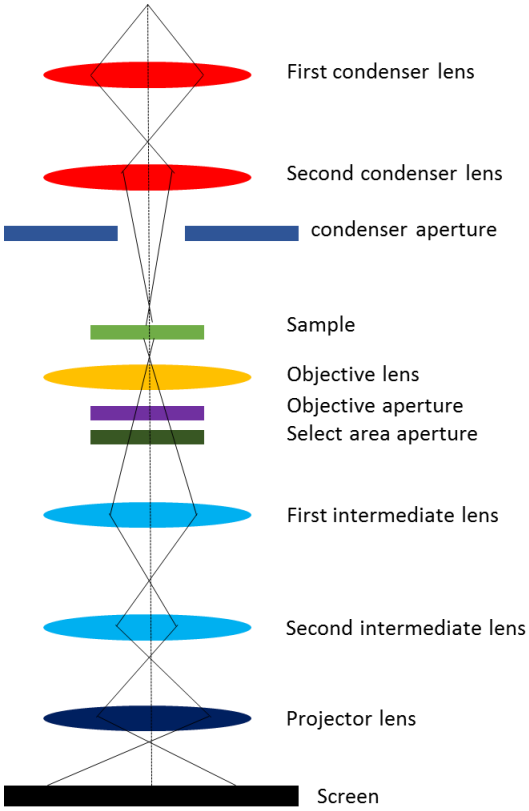

Figure 6.8 Schematic diagram of transmission electron microscope.

The transmission electron microscope which has been used for grain sizes analysis was JEOL JEM-2011. A Lanthanum hexaboride (LaB_6) filament is fitted at the top of the column which is operated under a high vacuum of 10^{-10} mbar. A series of roughing, diffusion, turbo-molecular, ion and cryogenic pumps are required. When the filament is heated to a temperature greater than the work-function, the electrons are emitted. The electron are then accelerated via an accelerating voltage from 80 – 200 kV. As Figure 6.8 shows the electrons pass through a condenser lens which consists of many electromagnetic coils. The current through these coil deflects the path of the electrons. The condenser lens is used to control the electron density travelling through the system. The electrons then interact with the sample located above the objective lens. This is used to focus the diffracted electrons after interaction with the sample. An intermediate image is then produced. A set of intermediate lenses and projector lenses then magnify the image by 50 to 1,500,000 times and project it onto the fluorescent screen. A digital image can be recorded with a Gatan Multiscan charge-couple device (CCD) camera fitted below the column. Apertures are used to form different images by selecting

electron beams and control the image contrast. By using the objective aperture the electrons that are imaged can be chosen to be either those are transmitted (Bright field) or diffracted (Dark field) only as shown in Figure 6.9.

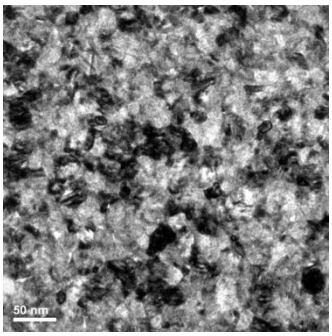

Figure 6.9 Schematic ray diagram of Bright field and dark field operation.

In this studies, bright field images were used for grain size analysis which will be discussed in the next section. TEM samples were prepared using the same procedure explained in previous section 5.1 with carbon-coated copper TEM grids used as substrates. Figure 6.10 shows a bright field image for polycrystalline Mn_3Ga thin film, the dark grains shown in the figure satisfy the Bragg condition which are valid for the grain size analysis.

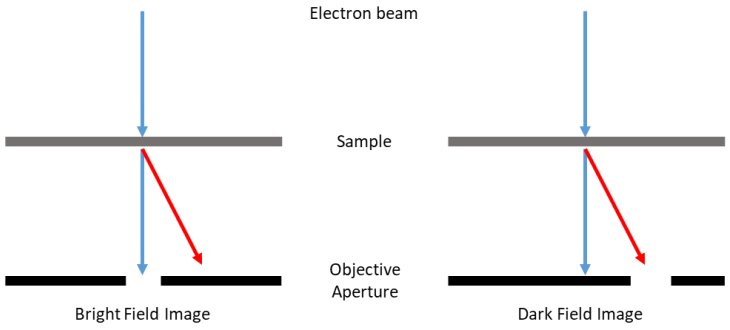

Figure 6.10 Bright field image of Mn_3Ga thin film.

6.2.6 Grain Size Analysis

Grain size analysis was undertaken using bright field TEM images. A Zeiss particle size analyser was used for grain size distribution measurements as shown in Figure 6.11.

Figure 6. 11 Zeiss particle analyser.

The original TEM images were printed with a scale bar indicating the magnification. The Zeiss particle analyser projects a light spot with tuneable radius. The light spot is used to match individual grains on the printed sheet. When the area of the light spot is equivalent to that of the grain, a pedal is depressed and a hole is punched through the image and registered as a voltage using a Lab View program. More than 500 particles were recorded in order to ensure good statistics and the data were then converted to an actual size according to the scale bar. The size distribution of a polycrystalline film follows a log-normal distribution. It is defined as a function so that the natural log of a random variable follows a Gaussian distribution [116],

$$f(\mathrm{D})d\mathrm{D} = \frac{1}{\sqrt{2\pi}\sigma_{\ln D} D}\exp\left\{-\frac{[\ln D - \mu^2]^2}{2\sigma_{\ln D}^2}\right\}d\mathrm{D} \tag{6-8}$$

$$D_m = e^{\mu} \tag{6-9}$$

$$\sigma_{\ln D} = \sqrt{\frac{\sum N\,(\ln D)^2}{\sum N} - \left(\frac{\sum N\,(\ln D)}{\sum N}\right)^2} \tag{6-10}$$

where D is the diameter of the grain, μ is the mean value of $\ln D$ and $\sigma_{\ln D}$ is the standard deviation of $\ln D$. The median grain diameter D_m and the standard deviation $\sigma_{\ln D}$ of the distribution is used to determine the grain size [116],

In this work the grain size of the sample was used in conjunction with the York model of exchange bias (see Chapter 5) to obtain the magneto-crystalline anisotropy constant of the antiferromagnetic Mn_3Ga. The anisotropy constant can be determined using Equation (6-10) when the sample is thermally stable at the temperature of measurement and has been fully set [117],

$$K_{AF}(< T_B >) = \frac{ln(1800 f_0) k T_B}{< V >} \tag{6-11}$$

where K_{AF} is the anisotropy constant, T_B is the temperature at which exchange field is zero, f_0 is an attempt frequency generally taken to be 10^9 s^{-1} and <V> is the median grain volume, the thermal activation time is set to 1800 s. In reality, not all the sample is thermally stable at the measurement temperature hence those unstable grains will not be taken into account during the calculation.

6.2.7 Scanning Electron Microscopy

In this study, the composition of the Heusler alloy thin films were carefully analysed because the atomic ratio between constituent elements strongly affects the magnetic properties and crystallographic structure of the sample. A JEOL JSM-5910LV scanning electron microscope (SEM) with an Oxford Instruments INCA energy dispersive X-ray (EDX) Si detector was used to measure the composition of the AF material.

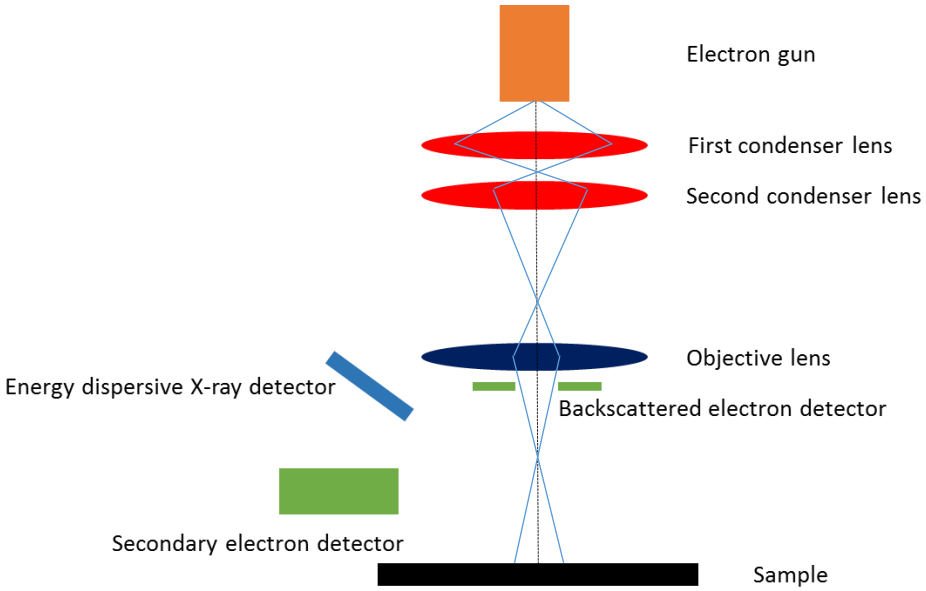

Figure 6.12 Schematic diagram of the A JEOL JSM-5910LV scanning electron microscope (SEM).

Figure 6.12 indicates the schematic diagram of the A JEOL JSM-5910LV scanning electron microscope (SEM). This microscope consists three important components which are the electron gun, magnification lenses and the detectors. Electrons are generated from a Tungsten hairpin filament with a current of 2.4 A. Condenser and projector lenses were used to focus the electron beam onto the sample and swept over the sample. There are several different processes that occur when the electrons beam enters the sample. Some incident electrons experience elastic or inelastic scattering and may end up in a direction back out of the sample surface. These electrons are called backscattered electrons and their number is dependent on the scattering cross section of the atoms in the sample involved in the scattering. There is another group of low energy electrons emitted from the sample surface which are called secondary

electrons. These electrons are excited out of the ground state of the atoms in the sample via interaction with high energy incident beams. The number of secondary electrons is dependent on the atomic number of the target sample, surface topography and energy of the incident electrons. A secondary electron detector receives the signal from secondary electrons generated by the primary beam which is then amplified and converted into an electrical voltage. Another inelastic process occurs when excited electron is de-excited into ground state and X-ray photons are generated. These photons determine the energy between two states and the composition of the material.

For imaging the sample surface, the incident electron beam scans over the surface and secondary electrons are collected by the detector and then display the changes in the number of secondary electrons as changes in the contrast on the monitor screen. The X-ray can be used when the electron beam is stationary, where the resulting spectra shows the average composition in the sampling volume of the scanned surface. Depending on the electron-atom interaction mechanism, electrons or photons may be emitted which means that the detectors positioned above the sample are able to detect these escaping from sample surface. The interaction volume is a pear-shaped penetrated area in which detectable interaction take place. The size of the interaction volume is determined by the electron beam energy and the atomic number of the specimen. The spread of the electron beam increases with the depth of penetration. For a sufficiently thin film, the beam spread is much less hence better spatial resolution is obtained. In Chapter 7.1, the chemical composition for Mn_2Vsi, Mn_3Ga and Mn_3Ge thin films are illustrated.

The precision of the EDX composition analysis is limited due to the large interaction volume and inhomogeneous sample. The microscope operates to a micron precision and the spectroscopy data have an expecting accuracy of 10% of the weight for the targeting samples.

6.3 Magnetic Characterisation Methods

Magnetic measurements in open circuits are usually made with a vibrating sample magnetometer (VSM) or alternating gradient force magnetometer (AGFM). The experimental data is a plot of a magnetic moment *m* vs the applied field *H*. AGFM provides higher sensitivities than VSM, however it is not suitable for low temperature measurement. In this study, VSM was used due to its capability for low temperature measurements. X-ray magnetic circular dichroism (XMCD) and x-ray photoemission electron microscopy (XPEEM) measurement was also performed at the SIM beamline at Paul Scherrer Institute (PSI) with the help from Dr. Carlos. A. F. Vaz.

6.3.1 Vibrating Sample Magnetometer (VSM)

To measure the magnetic properties of nanoparticles and thin films, a vibrating sample magnetometer (VSM) is the instrument of choice. Invented in 1955 by Foner [118], the VSM was an improvement on Smith's vibrating coil magnetometer [17,18].

VSM is based on the principle of Faraday's law. The equation for electromagnetic induction is:

$$\varepsilon = -N_c \frac{d\varphi}{dt} \tag{6-12}$$

where ε is the induced electromagnetic force (*emf*), N_c is the number of turns in the coils and $\frac{d\varphi}{dt}$ is the rate of change of flux. The change of flux is induced by a mechanical vibration of the sample under an external magnetic field from the electromagnet. The total magnetic flux penetrating the sample is.

$$\varphi = \vec{B_M} \cdot \vec{A} \tag{6-13}$$

where $\vec{B_M}$ is the magnetic flux density in the material and $\vec{A}$ is the area of the sample. When the sample is vibrating it induces an *emf* that is calculated using Faraday's law, which is:

$$\int \varepsilon dt = -N\vec{A} \cdot \vec{M} \tag{6-14}$$

where $\vec{M}$ is the magnetisation of the sample.

VSM operation depends upon a set of pickup coils between which, the sample is vibrated, whilst a field is applied, creating an AC signal within the coils. A speaker driver adjusted to ~ 81 Hz provides the vibration to the sample and prevents interference from mains driven noise. The oscillating magnetic field of the moving sample induces an alternating electromagnetic force (*emf*) in the detection coils, whose magnitude is proportional to the magnetic moment of the sample. A reference signal is created at the top of the sample rod that converts the induced AC voltage to a DC output voltage, usually with a lock-in amplifier which is sensitive only to signals at the vibration frequency.

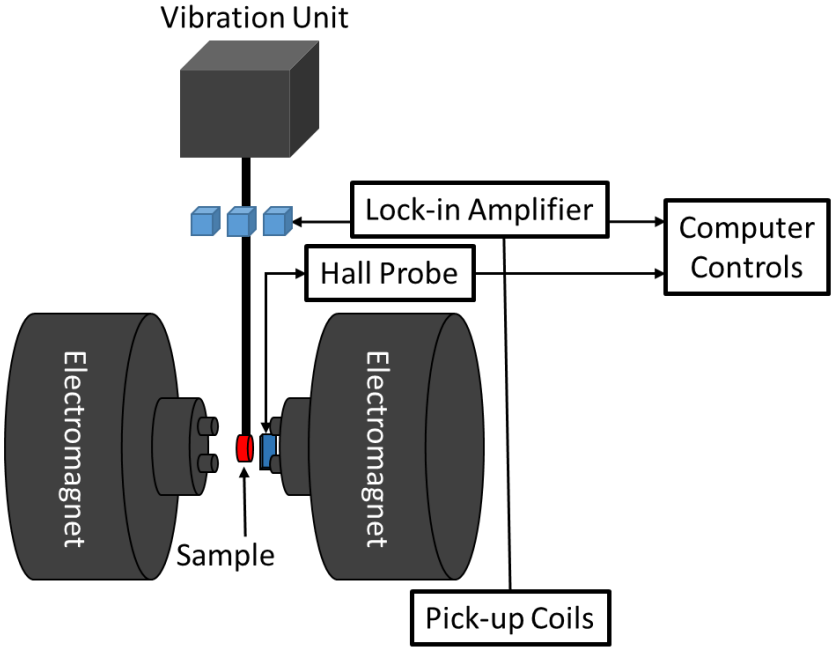

Figure 6.13 Schematic of a Vibrating Sample Magnetometer.

The design of the coils used in VSM is key to achieving low-level noise measurements. This specific version of the Microsense VSM, the Model 10, has a high sensitivity of 10^{-6} emu. Rotation of the magnet is possible within the range of -540 to + 540 degrees (resolution <0.1 degree). The vector coils are a standard option. At the most optimal gap of pole pieces, the system can reach a maximum field of 20 kOe. Temperature variation from 773 to 100 K is available via a gas-flow system. This controls the nitrogen flow over a heater to stabilise the temperature with 0.01 K temperature

resolution. The design of the VSM isolates the system from external magnetic and acoustic noise and permits measurements to be made rapidly under a variety of conditions.

VSM provides experimental results in magnetic moment (*m*) vs the applied field (*H*) where calibration of both *H* and *m* is required on weekly bases to keep the accuracy. The applied field *H* is calibrated by first calibrating the hall probe at zero field shield to check the zero pint. Then the probe is placed in an applied field which is measured by the Hall probe and calibrated against a Lakeshore 425 gauss meter which is a secondary standard. The calibration of *m* was carried out using a Palladium foil whose geometry and dimension is similar to that of the sample to be measured. Palladium is a Pauli paramagnet with high corrosion resistance whose susceptibility is not temperature dependent, therefore has a fixed value of moment at any applied field.

Magnetisation curves are generated from the VSM and provide the general magnetic properties of the Heusler alloy thin film, such as coercivity (H_c), saturation magnetisation (M_s), remnant magnetisation (M_r), squareness (M/M_s) and nucleation field (H_n).

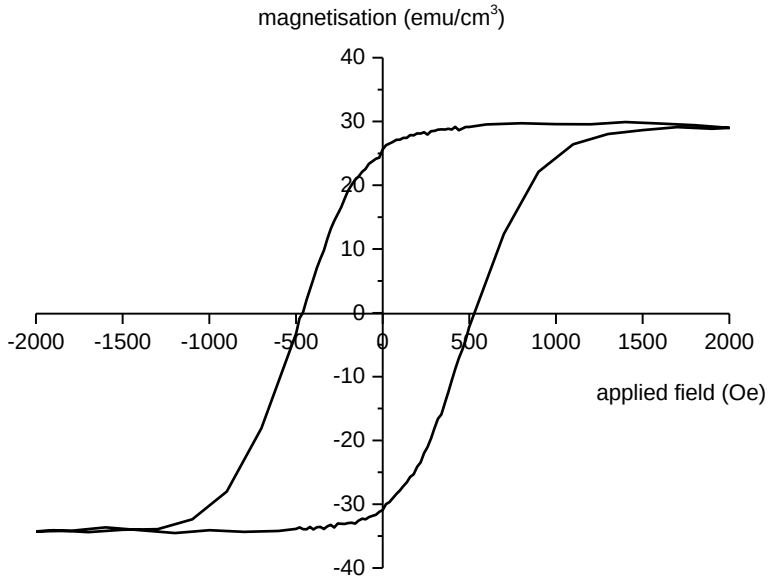

Figure 6. 14 Hysteresis loop measurement [121]

6.3.2 Thermal Activation Measurements

In this work, the magnetic properties of antiferromagnetic (AF) materials have been studied using the Microsense Model 10 VSM. This was achieved by attaching a ferromagnetic (F) layer using thermal activation measurements [14].

The thermal activation measurement is a unique way of measuring the blocking temperature (T_B), i.e., the point at which the exchange bias induced at the AF/F interface is zero. Normally T_B is determined by increasing the activation temperature until the loop shift becomes zero. In polycrystalline systems, individual grains have their own T_B and hence the average T_B, $< T_B >$, is measured using the York Protocol. The theory of the York Protocol was discussed in the previous chapter. Blocking temperature for granular AFs can be measured by the steps as shown in Figure 6.15.

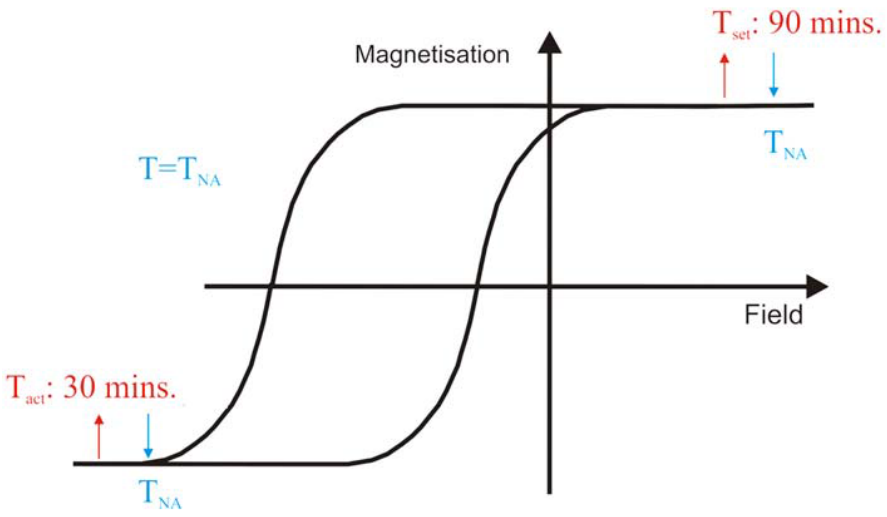

Figure 6.15 Schematic diagram of measurements procedures of the York Protocol [14].

1. In order to ensure there is no magnetic history affecting the measurements, the samples were set under a saturating applied field of 20 kOe at a maximum

temperature T_{set} (500 K) at which interfacial duffusion between layer does not occur for 90 minutes.

2. The samples were field cooled to non-thermal activation temperature T_{NA} (100 K).
3. The samples were heated to a thermal activation temperature T_{act} for 30 minutes with a reversed magnetic field applied.
4. The samples were cooled down to T_{NA}.
5. Hysteresis loops were taken at T_{NA} where all AF grains are thermally stable.

In all polycrystalline thin films, the volume of the AF grains follows a log-normal distribution. V_c is the minimum AF grain volume that is stable at the temperature of measurement and contributes to the exchange bias. For those grain volumes below V_c, the orientation of the AF alignment of a grain fluctuates under the influence of thermal energy as they are too small to be thermally stable at the temperature of use. Hence these grains do not contribute to the exchange bias. Essentially these small grains behave as a superparamagnetic particles of a ferromagnetic material. V_{set} is the maximum AF grain volume that can be aligned in order to contribute to the exchange bias at T_{set}. Grain volumes beyond V_{set} cannot be set because the AF grain upon which they have grown is itself not aligned at the temperature which can be applied. These two limits V_c and V_{set} are shown on the grain size distribution in Figure 6.16.

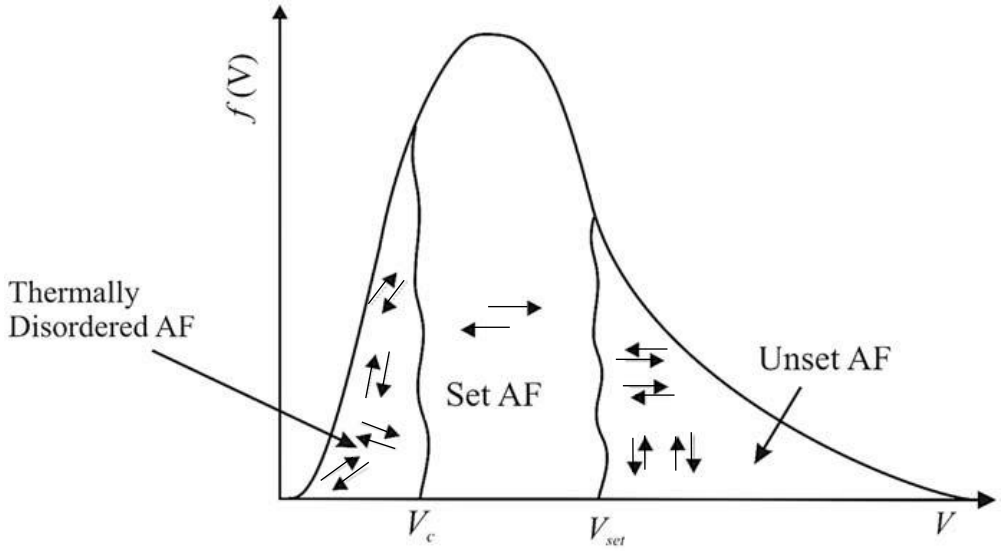

Figure 6.16 Schematic diagram of AF grain size distribution [14].

6.3.3 Training Effect

The earliest studies to describe the training effect was conducted by D. Piccard *et al*. [122] in 1966. The authors describe a drop in coercivity caused by movement of both legs of the hysteresis loop during field cycling. The unbalanced movement of the legs results in an overall reduction in exchange field (H_{ex}). They note both the temperature and time dependence of the rate of change. They established the pre-training state which can be recovered by two methods: Field cooling from above T_N or exposing the sample to a saturating field at $T_{measure}$. These observations can be explained with the York Model if the assumption is made that $T_{measure} > T_{N,}$ which can be justified given that T_N is around room temperature for all samples. Because of this, the AF layer is thermally active and is set by thermal activation, effecting recovery of H_{ex} and H_C.

In order to remove the training effect during the measurement, applied field is set in the opposite direction to the external field.

6.3.4 XMCD Introduction

Since I was not directly involved in the detailed measurement process, the detailed instrument operational information will not be discussed in this section. This section will mainly focus on the brief theory of XMCD and methods of XMCD analysis.

XMCD is a unique technique that uses X-ray to study magnetism. The technique provides element specificity, and it also enables the operator to determine where the magnetic signal originates from within a certain material. The materials that the technique can be applied to range from elemental films to more sophisticated alloys and compounds.

For the 3*d* transition metals, on which this work focuses on Mn and Co elements, it is important to gain insight into the dichroic effect for the L3 and L2 edges. Noteworthy, these two edges correspond to the $2p_{1/2}$ and $2p_{3/2}$ levels, respectively, both of which are discernible in the context of a *p* to *d* transition. It is possible to view the situation in terms of energy level diagrams, as seen in Fig 6.17.

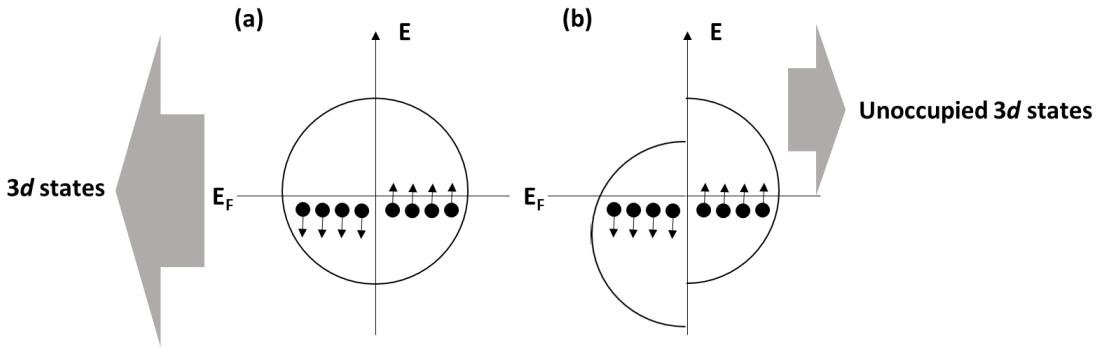

Figure 6.17 Band illustrations of (a) a non-magnetic material and (b) a magnetic material with an external field.

Figure 6.17 (a) shows a non-magnetic material without magnetic field. The number of spin up and spin down electrons are at an equal levels in its population. On the other hand, Figure 6.17 (b) shows how the application of an external magnetic field (*H*) to a magnetic field facilitates disequilibrium between the spin up and spin down bands. As a consequence of this, a configuration arises in which certain unoccupied 3*d* spin up states exist that can only be filled with spin up 2*p* electrons. Hence, it is possible for the unoccupied 3*d* states to serve as spin-dependent detectors. Noteworthy, this case becomes even more complex when considering the spin-orbit interaction, the result of which is to split the 2*p* core state into a pair of components: firstly, the $2p_{1/2}$ level; and secondly, the $2p_{3/2}$ level. In addition to the energy separation of these components, which amounts to few eV, the effect is important because these spin sub-states are now coupled to the orbital moment. The complexity increases owing to the orbital moment in view of the way in which it couples to the spin moment in a parallel way to the L3 edge, and in an antiparallel way to the L2 edge [123].

The right incident circularly polarised photons have a negative angular momentum, and for the left circular polarisation, it is positive. Hence, when attempting to illuminate the sample using circularly polarised light, the excitation likelihood increases when the X-ray photons' angular momentum is consistent with that of the orbital momentum. The probability is that a spin up $2p_{1/2}$ will be excited by left circularly polarised light, and the disparity in detected absorption between left and right circularly polarised light is evident when examining the XMCD signal.

6.3.5 Method of XMCD Analysis

The Sum Rules analysis was devised in the 1990s [124][125], and in the ground breaking research of Chen *et al* [126], a concrete way in which to apply the Sum Rules was established. Now, the approach is prominently applied in the literature as a key way to conduct XMCD analysis. As a popular quantitative method, derived from knowledge in the field of electromagnetism and quantum phenomena, the spin and orbital moments of 3*d* transition materials can be accurately measured using SR analysis. According to the Sum Rules, the orbital and spin magnetic moments can be determined from x ray absorption spectra (XAS) and XMCD spectra using the following equations [127]:

$$m_{orbital} = -\frac{4\int_{L3+L2}(\mu_+ - \mu_-)d\omega}{3\int_{L3+L2}(\mu_+ + \mu_-)d\omega}(10 - n_{3\mathrm{d}}) \tag{6-15}$$

$$m_{spin} = -\frac{6\int_{L3}(\mu_+ - \mu_-)d\omega - 4\int_{L3+L2}(\mu_+ - \mu_-)d\omega}{\int_{L3+L2}(\mu_+ + \mu_-)d\omega}(10 - n_{3\mathrm{d}})(1 + \frac{7 < T_z >}{2 < S_z >})^{-1} \tag{6-16}$$

$$m_{total} = m_{orbital} + m_{spin} \tag{6-17}$$

Where m_{total}, $m_{orbital}$ and m_{spin} are the total magnetic moment, orbital magnetic moment and spin magnetic moment in the unit of μ_B/atom respectively. $n_{3\mathrm{d}}$ is the electron occupation of the respective transition metal atom in 3*d* states. The L3 and L2 represents the integration range. $< T_z >$ is the expectation value of the magnetic dipole operator and $< S_z >$ is equal to half of m_{spin} in Hartree atomic unit.

In order to simplify the equations, three new terms *p*, *q*, *r* are used to replace the integrations, where:

$$p = \int_{L3}(\mu_+ - \mu_-)d\omega \tag{6-18}$$

$$q = \int_{L3+L2} (\mu_+ - \mu_-) d\omega \tag{6-19}$$

$$r = \int_{L3+L2} (\mu_+ + \mu_-) d\omega \tag{6-20}$$

Figure 6.18 gives an example that contains three new terms *p*, *q*, *r* as the replacement of the integration in the above equations. The integration area of XMCD and XAS spectra is indicated by the dash line in Figure 6.18.

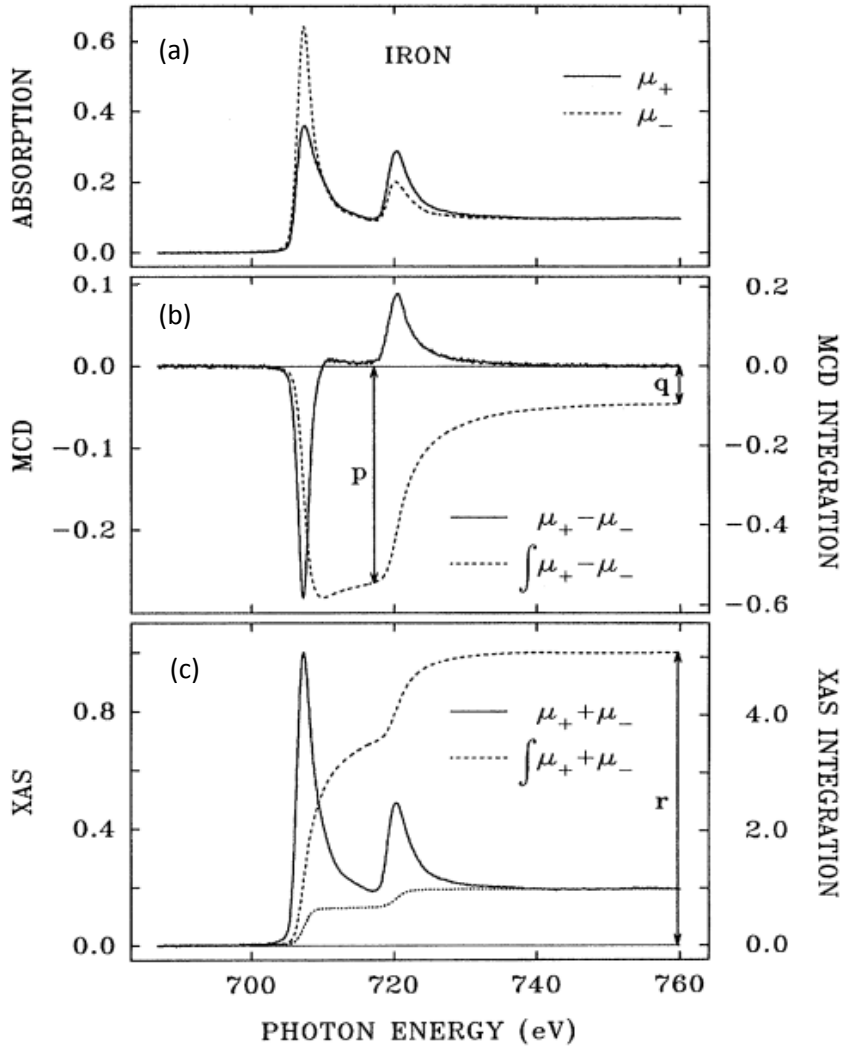

Figure 6.18 The sum rule constant, *p*, *q*, and *r* which correspond to the integral of the dichroism spectra for the L_3 edge, the integral of the dichroism spectra over both the L_3 and L_2 edges and the area of the summed XAS signal after removal of a stepped background respectively [126].

Chapter 7

Antiferromagnetic and Ferrimagnetic Heusler Alloys Films for Spintronic Devices

In this study, based on the previous study on Ni_2MnAl conducted by Teodor Huminiuc and Oliver Whear, a new set of Heusler alloys of Mn_2VSi, Mn_3Ga and Mn_3Ge was investigated during the last three years. The growth conditions of these films were first optimised using the HiTUS sputtering system. Their chemical components were characterised using scanning electron microscope (SEM) and energy dispersive X-ray spectroscopy (EDX). The structural study of the films was conducted using X-ray diffraction (XRD) and Transmission electron microscopy (TEM). The magnetic characterisation was performed using Vibrating sample magnetometer (VSM) and surfaces/interfaces: Microscopy (SIM) Beamline at Paul Scherrer Institute. In this chapter, these measurement results for three Heusler alloy films are discussed.

7.1 Chemical Analysis of Polycrystalline Heusler Alloys

The composition of the Heusler alloy thin films was carefully analysed because the atomic ratio between constituent elements strongly affects the magnetic properties and crystallographic structure of the sample. A SEM, JEOL JSM-5910LV, (10 keV acceleration voltage beam as discussed in Chapter 6.2.7) with an EDX, Oxford Instruments INCA, using a Si detector was used to measure the composition of the AF Heusler alloy films. For the composition analysis Mn_2VSi, Mn_3Ga and Mn_3Ge samples were grown at a thickness of 100 nm on Si substrates at a bias voltage of 900 V. 10 data points were measured using 10 keV electron beam energy for averaging, the results are listed in Table 7.1. A lower electron beam energy such as 5 keV cannot penetrate the thin film. A higher electron beam energy may destroy the sample surface and change the composition because Gallium has much lower melting point (302 K) than Manganese (1517 K). Therefore Gallium is easily evaporated during the deposition leading to a Mn-rich film. It is worth to note that the sample was assume to be a homogeneous solid so that the absolute quantification of the chemical composition of the film may contain a systematic error.

Table 7.1 Results of the chemical analysis performed by JEOL JSM-5910LV scanning electron microscope.

Heusler Alloy X_2YZ/X_3Z	Bias Voltage (V)	Composition (±10 %)		
		X	Y	Z
Mn_2VSi	900	55.16	17.87	26.97
Mn_3Ga	900	70.03	-	29.97
Mn_3Ge	900	73.04	-	26.96

7.2 Structural Characterisation of Polycrystalline Mn_2VSi

Polycrystalline Mn_2VSi films (80 nm thick) were deposited on Si (001) substrates and capped by a 3 nm Al layer using a PlasmaQuest high target utilisation sputtering system (HiTUS) at room temperature (RT). The deposition rate of the Mn_2VSi films was typically 0.07 nm/s. However, there is no crystallisation observed in the as deposited Mn_2VSi alloy. Hence, it is necessary to introduce a seed layer and a high growth temperature in order to promote the crystallisation of Mn_2VSi. As we will show later (page 113), 80nm thick film supports A2-type phase.

Previous work conducted by Sagar *et al.* [110] showed that using a lattice matched seed layer improves the crystallisation of ferromagnetic Heusler alloys at low post-annealing temperatures. For Mn_2VSi, chromium and silver were used as a buffer and seed layer respectively as shown in Figure 7.1. A 3 nm thick Cr buffer layer is used to smooth out the surface of the substrate and to promote adhesion and to prevent island growth of Ag. Silver was chosen as a suitable seed layer because the lattice mismatch was calculated to be 2% when the crystals were oriented at 45° to the Mn_2VSi. According to Whear *et al.*, the optimum thickness of the Ag seed layer is 15 nm as reported for Ni_2MnAl [128]. Due to the similarity between two materials, the same seed layer thickness is assumed to be optimal for MnVSi.

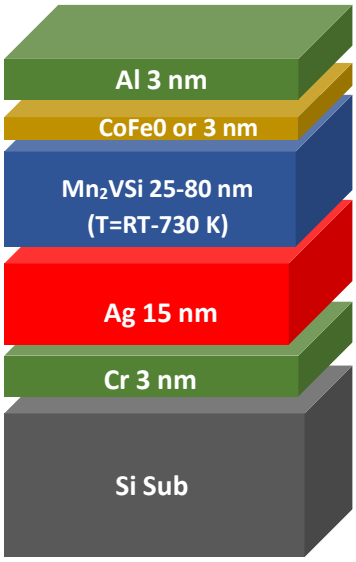

Figure 7. 1 Schematic diagram of Mn_2VSi films deposited

During the Mn_2VSi deposition the substrates were heated to temperatures between 473 K and 730 K. It is important to note that during deposition at high temperature, the samples are easily oxidised. As a consequence, the pressure inside the sputtering chamber is required to be below 4×10^{-7} mbar to avoid any oxidation. As shown in Figure 7.2 (a), the peaks from θ-2θ XRD scans show the integrated area and width which indicate crystallisation orientation as a function of the deposition temperature. The roughness of the curves was due to the noise during the measurement. Samples which were sputtered at the highest temperature (723 K) were found to show a significantly stronger $Mn_2VSi(220)$ peak at about 46.1^o than those grown at lower temperatures (<723 K) [see Figure 7.2(a)]. This at least confirms the formation of the *A*2 phase. In particular, the films grown at 723 K provided the strongest $Mn_2VSi(220)$ Heusler peak, whose full width half maximum (FWHM) is measured to be 0.396^o for the 80 nm thick case. This is almost a factor two reduction in the FWHM compared with the other samples, such as those grown at 523 K (FWHM= 1.27^o). Post-annealing was also used to compare with the heated growth method as described above. Here, the samples were grown at room temperature using HiTUS. The sputtered films were then placed into an annealing furnace (Carbolite, MTF 10/25/130, maximum temperature: 1273 K) for post-annealing at elevated temperatures between 573 and 923 K for 3 hours under 8×10^{-5} mbar. The XRD results for the post-annealed samples are shown in Figure 7.2(b). The $Mn_2VSi(220)$ peak at about 45.1^o is much less significant (FWHM=0.52^o

for 873 K, for example, as listed in Table 7.2) than those for the films grown at high temperature. In Figure 7.2(c), a structural comparison is shown between 25 and 80 nm thick Mn_2VSi films. Here, the 80 nm-thick Mn_2VSi film show the $Mn_2VSi(220)$ peak, confirming the formation of the *A*2 phase at least.

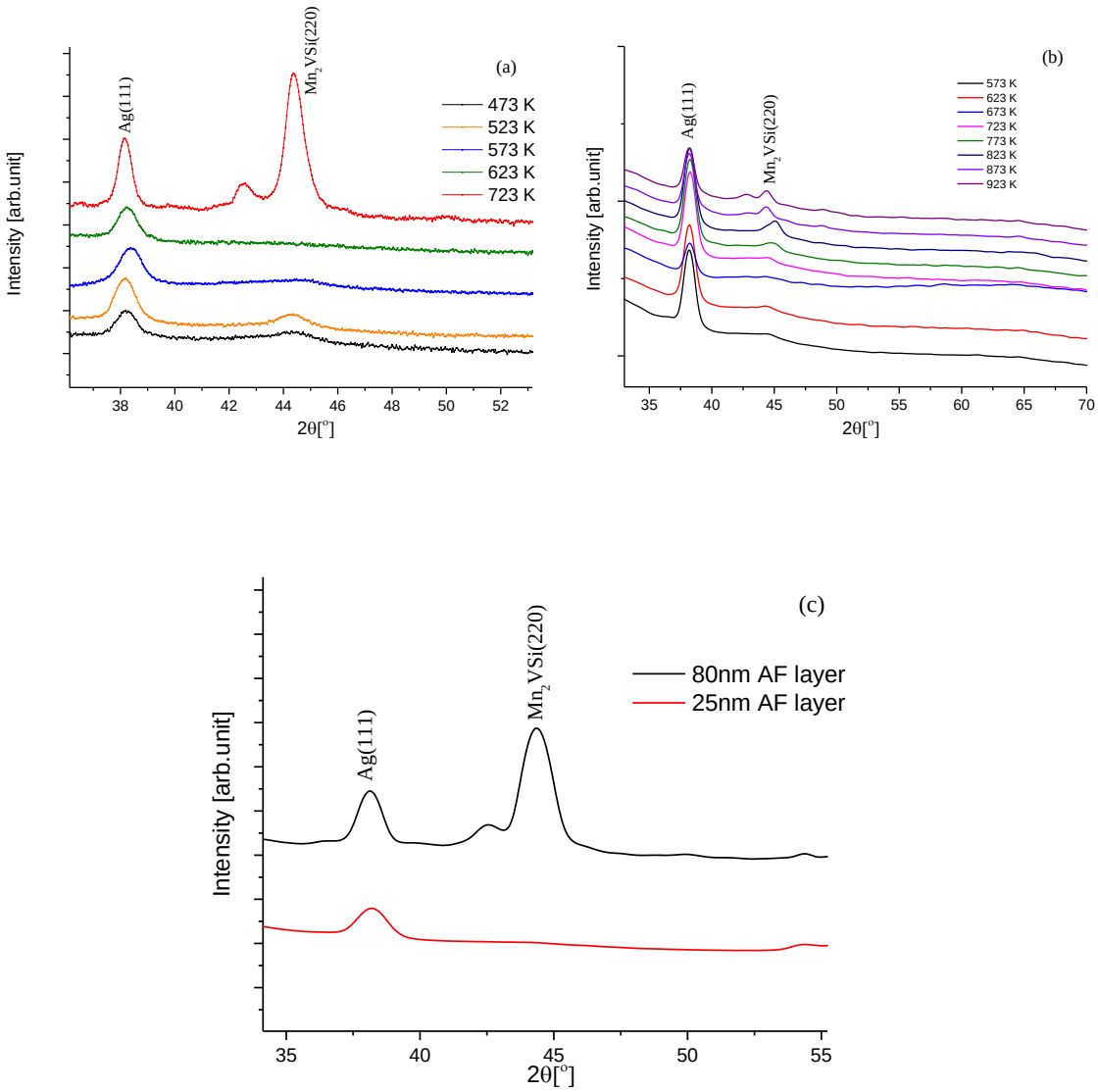

Figure 7.2 XRD scans for (a) 80 nm Mn_2VSi samples grown at elevating temperatures, (b) 80 nm Mn_2VSi samples post-annealed at elevating temperatures and (c) different thickness of Mn_2VSi samples grown at 723 K.

Table 7.2 List of Mn_2VSi(220) peak with different post-annealed temperature.

Post anneal temperature	723 K	773K	823 K	873 K	923 K
FWHM of Mn_2VSi (220) peak	0.93°	1.80°	0.53°	0.52°	0.46°

The corresponding X-ray reflectivity (XRR) results are shown in Figure 7.3. For the post-annealed films, weak oscillations indicate that interface between layers are rough. This is because during the post-annealing process the whole sample is heated, causing the diffusion at the interface between each layer. The 25 nm thick Mn_2VSi film grown at 723 K shows the smoothest interfaces. By fitting the result using GenX [114], the estimated thicknesses are Cr (2.8 ± 1.8) nm/Ag (17.2 ± 1.2) nm/Mn_2VSi (24.0 ± 0.3) nm/CoFe (3.7 ± 0.2) nm/Al (2.3 ± 0.2) nm. On the other hand, the 80 nm thick Mn_2VSi film grown at 723 K shows rougher interface. These results indicate that the thinner films minimises the interfacial diffusion during the deposition. However the thinner samples show smaller average grain size (no Mn_2VSI (220) peak shown at 46.1° for 25 nm) as compared with the thicker layer (FWHM= 0.396 ° for 80 nm), as shown in Figure 7.2(c). This is because the thickness of Mn_2VSi is too thin for the XRD signal to be detected. Therefore, the films are optimised to grow at 723 K with 80-nm-thick Mn_2VSi layer to obtain a preferred crystallisation orientation.

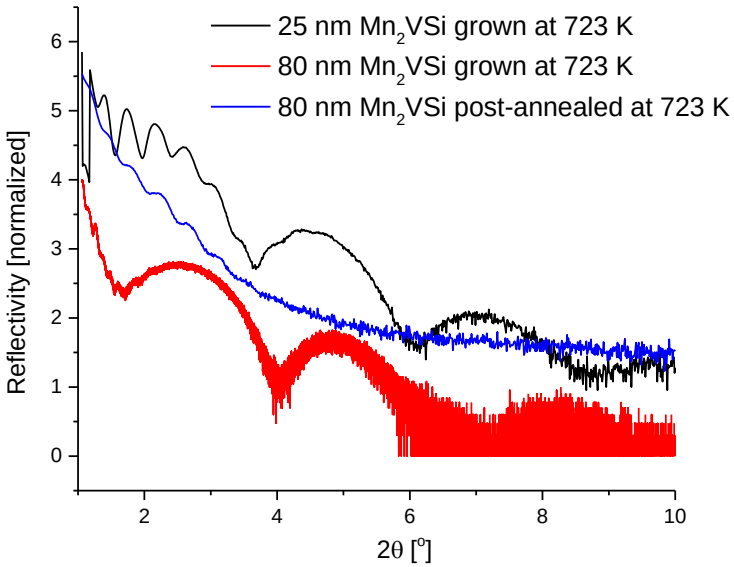

Figure 7.3 X-ray reflectivity scans for Mn_2VSi/CoFe films grown at 723 K and post-annealed at 723 K.

Samples studied in this work were all polycrystalline where the diffraction patterns usually containing a combination of amorphous, highly-textured polycrystalline layers and single crystal substrate. Scherrer's grain size analysis is a simple method to estimate the average grain size in a material from the width of an XRD peak. In general, a sharp peaks (small FWHM) indicate large grains, whereas broader peaks (large FWHM) indicate small grains. This is described by the Scherrer equation:

$$D = \frac{C\lambda_R}{\text{FWHM}\cos\theta} \tag{7-1}$$

where D is the average grain diameter, C is a constant close to unity which has a value of 0.94 [129], λ_R is the wavelength of the radiation, θ is the Bragg reflection angle. Noteworthy, the unit of FWHM needs to be in radian when operating the calculation using equation (7-1). The broadening effect will occur when the Bragg reflection angle is large due to the inverse proportionality between the grain size and the diffraction angle.

The grain size of Mn_2VSi grown at 723 K and 523 K was estimated using the Scherrer analysis as discussed in Chapter 6. The average grain diameter of 80 nm thick Mn_2VSi grown at 723 K is (22.6$\pm$0.3) nm, whereas the film grown at 523 K shows a much smaller grain diameter of (7.0$\pm$0.2) nm. This result indicates samples deposited at higher temperature have larger grain size, and hence it's easier to be detected using XRD.

7.3 Magnetic Characterisation of Polycrystalline Mn_2VSi

The magnetic characteristics of the Mn_2VSi samples were measured using a Microsense VSM. The 80-nm-thick Mn_2VSi films were deposited on a $16 \times 16\ \text{mm}^2$ single crystal Si substrate with 3-nm-thick Cr and 15-nm-thick Ag as buffer and seed layers at elevated temperatures. The substrate was cut into $5 \times 5\ \text{mm}^2$ pieces using a diamond pen in order to fit into the VSM probe. Similar to Mn_3Ga films to be discussed later, the samples were measured by VSM at room temperature showing paramagnetic behaviour as shown in Figure 7.4. There is no hysteresis loop found which indicates that the paramagnetic behaviour may be contributed by the seed layer

and hence Mn_2VSi shows no net magnetic moment at elevated temperature due to its antiferromagnetic nature.

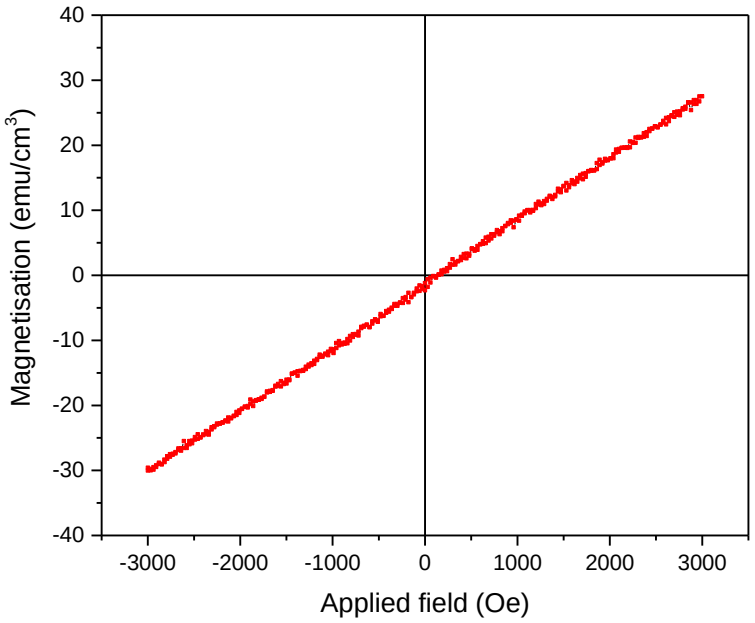

Figure 7.4 Magnetisation curve for polycrystalline Cr (3 nm)/Ag (15 nm)/Mn_2VSi (80 nm)/Al (3 nm) films measured at room temperature.

In order to verify if the Mn_2VSi thin films are antiferromagnetic, a 3 nm ferromagnetic layer was deposited on the top of the Mn_2VSi layer. When materials with ferromagnetic (F) ordering and antiferromagnetic (AF) ordering are in close contact and are field-cooled below the Néel temperature (T_N) of the AF, an exchange bias is induced in the F layer (as discussed in Chapter 5). The exchange bias introduces a shift in the hysteresis loop along the field axis, which is in the opposite direction of the setting field. Two F materials are compared for the exchange bias measurements; $Co_{0.6}Fe_{0.4}$ and Co_2FeSi. The CoFe alloy is a commonly used high magnetisation ferromagnet which allows for reduced thicknesses of the thin film while keeping the values of the magnetisation detectable. Co_2FeSi is a well-known ferromagnetic Heusler alloy that was reported to couple well to AF materials such as IrMn [130]. Moreover, the ferromagnetic Heusler alloy allows in theory for lattice matched coupling between the AF and F thin films as they both have similar size unit cells. As shown in Figure 7.5, two samples were measured using the VSM at 100 K. The

coercivity for Mn_2VSi/CoFe film is 200 Oe whereas for the Mn_2VSi/CoFeSi film, it is only 23 Oe. In the rest of this study, $Co_{0.6}Fe_{0.4}$ was chosen as the F layer.

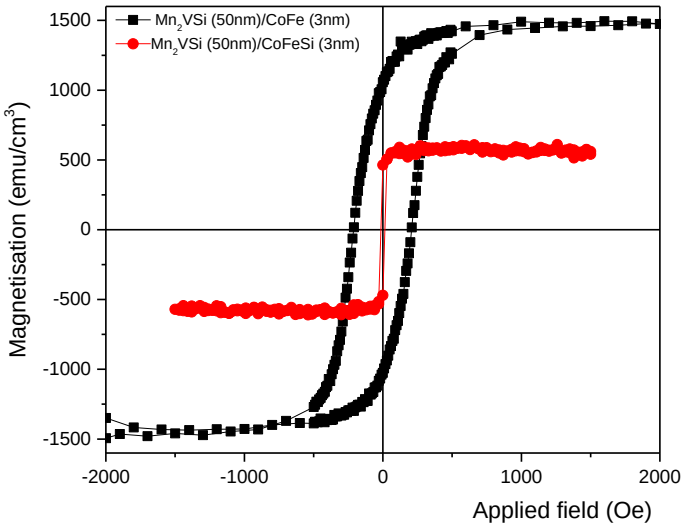

Figure 7. 5 Magnetisation loops for Mn_2VSi/CoFe (in black) and Mn_2VSi/CoFeSi (in red) measured at 100 K.

In Figure 7.6 the loops also show an increase in their coercivities, $H_{C,}$ from 114 Oe to 200 Oe with the increase in the thickness of the AF layer from 25 nm to 80 nm. It should also be noted that a significant decrease in the remanence is observed as the AF layer thickness increases as shown in Figure 7.6, indicating that the thicker AF layer may form a rough surface inducing the formation of a magnetically dead layer at the Mn_2VSi/CoFe interface. If the measurement is performed at a temperature close to T_N of the AF, the changes in the hysteresis loop become smaller. In Mn_2VSi, we use the setting temperature of 498 K for 90 minutes to ensure the AF layer paramagnetic. Under an external field of 20 kOe, the spin moments in the CoFe layer are aligned along the direction of the field. The samples with different thicknesses of the Mn_2VSi layer are measured at 100 K. The samples with the 80 nm Mn_2VSi layer are found to induce the largest exchange bias of about 30 Oe, whereas the rest of the samples show their exchange biases of less than 10 Oe (see Figure 7.6). This indicates that the Mn_2VSi cannot align their spin moments antiferromagnetically and hence cannot induce a large exchange bias.

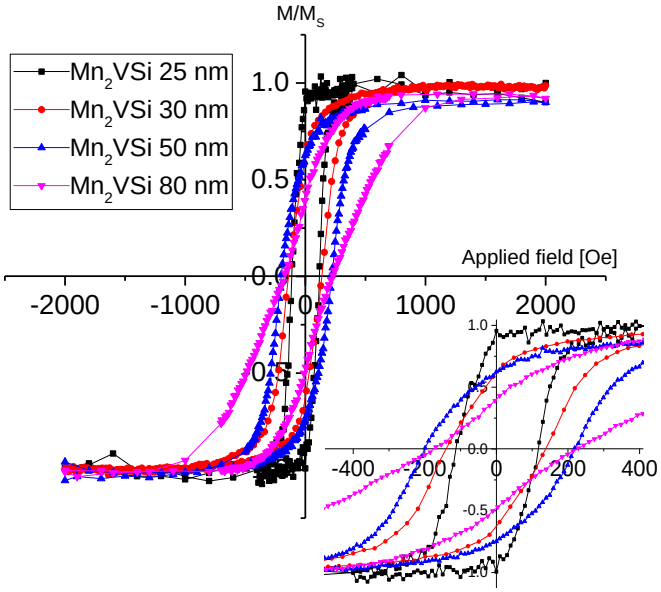

Figure 7.6 Magnetisation loops of Mn_2VSi/CoFe (3 nm) layers with different Mn_2VSi layer thicknesses grown at 723 K.

The activation temperature (T_{ACT}) is also measured to determine the blocking temperature (T_B), where the exchange bias becomes zero. In polycrystalline systems, individual grains have their own T_B and hence the average T_B is measured using the York Protocol [14]. The samples are uniformly set by thermal activation to the same setting state as described above (498 K for 90 minutes) before being cooled to T_{NA} (a temperature at which no thermal activation occurs), thereby removing any magnetic history. By using a saturating magnetic field (20 kOe) at a setting temperature (T_{SET}) that is above T_N of the AF Mn_2VSi film (estimated to be below 498 K) [131] but below the Curie temperature (T_C) of the F CoFe film (1273 K). A period of 90 minutes would reverse any activated grains to their original 'set' state. This period also negate any thermal activation that may occur during the temperature rise and fall [14]. The sample is then cooled down to T_{NA}. T_{NA} is set to 100 K because this is the lowest temperature the VSM can achieve. The magnetisation orientation of the F layer is then reversed. The sample is then heated for 30 minutes to an activation temperature T_{ACT}, followed by cooling back to T_{NA}. A revered field is applied so that can remove the first loop training effect (as discussed in Chapter 6) and measuring at T_{NA} ensures that slow thermal training does not occur. The average exchange bias is measured to be 34 Oe at 100 K as shown in Figure 7.7. Here, the exchange bias does not go to zero as

temperature changes. This result indicates that the blocking temperature is below 100 K. These characteristic temperatures can be engineered by substituting some constituent atoms in Mn_2VSi with other atoms as similarly demonstrated in ferromagnetic Heusler alloy [132] which may increase the anisotropy of AF layer.

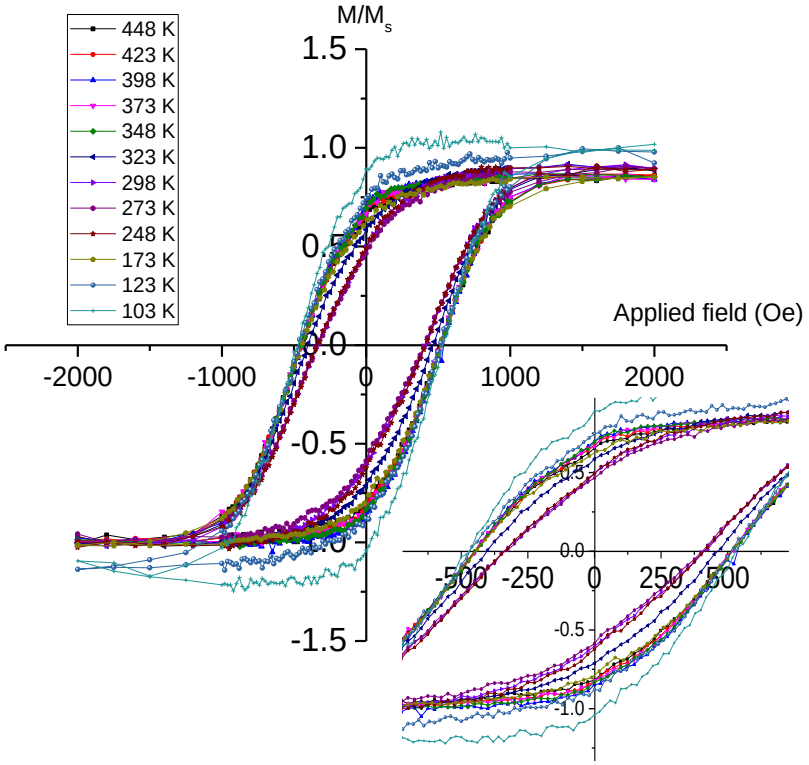

Figure 7.7 Magnetisation curves for the 80-nm-thick $Mn_2VSi/Co_{0.6}Fe_{0.4}$ film for different activation temperatures between 103 K and 448 K.

Mn_2VSi is confirmed to be antiferromagnetic, where the corresponding exchange bias of 34 Oe at 100 K is measured when a 3 nm ferromagnetic CoFe layer is deposited on the top of the Mn_2VSi layer. The film with an 80 nm thick AF layer is found to be optimised for the growth at 723 K. Post-annealed samples provided large surface roughness and causing the diffusion at the interface between each layers, resulting in no exchange bias induced at the Mn_2VSi/CoFe interfaces. The blocking temperature of Mn_2VSi grown at 723 K is estimated to be below 100 K. These magnetic properties can also be improved by substituting the constituent atoms with the other elements, suggesting a potential of Mn_2VSi to be used as an antiferromagnet in a spintronic device.

The experimental results for polycrystalline Mn_2VSi were compared with epitaxial Mn_2VAl film reported by T. Tsuchiya *et al*. [60] Similar to Mn_2VSi film, the *A*2-type Mn_2VAl films deposited at 673 K also showed no spontaneous magnetisation indicating antiferromagnetic behaviour. The exchange bias of both antiferromagnetic Heusler alloys is small (34 Oe at 100 K for polycrystalline Mn_2VSi film and 120 Oe at 10 K for epitaxial Mn_2Val film). The estimation of low blocking temperature for Mn_2VSi also agrees with that of Mn_2VAl (approximately 200 K [133]).

7.4 Structural Characterisation of Polycrystalline Mn_3Ga

20 nm Mn_3Ga films were initially grown directly on Si(001) single crystal substrates with a 5 nm of Pt capping layer under various bias voltages ranging from 300 V to 900 V at room temperature. As shown in Figure 7.8(a), there is a large possibility that Mn_3Ga(0002) peak is overlapped with Pt(111) and no change in crystallisation can be observed by changing the bias voltage during the growth. When the growth temperature increases from room temperature to 673 K, the crystallisation still remains unchanged as shown in Figure 7.8(b). Therefore, the crystallisation of Mn_3Ga has a relatively weak relationship to temperature and bias voltage as compared with the other Heusler alloys.

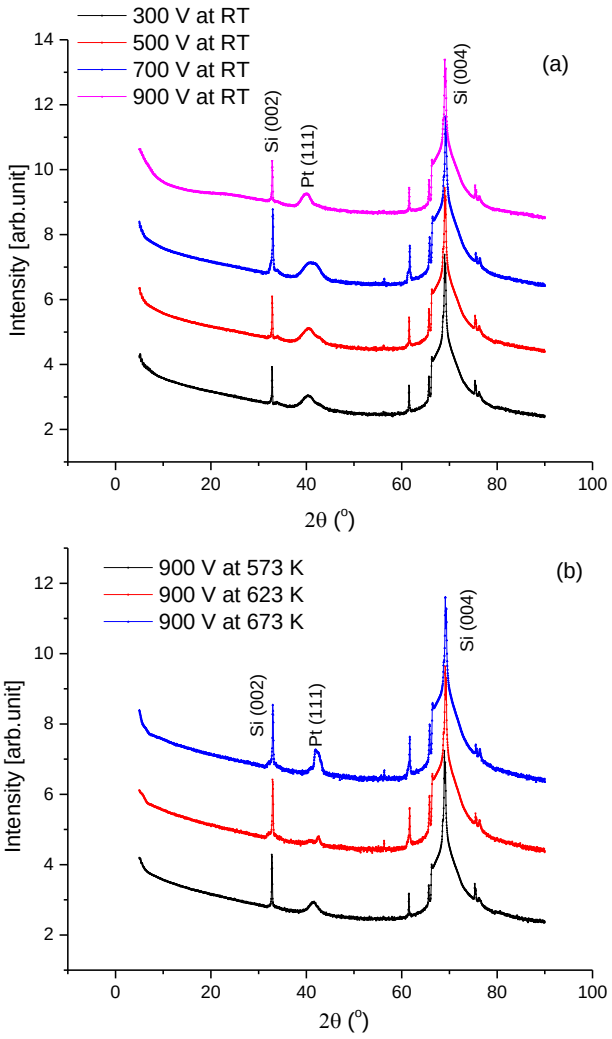

Figure 7.8 (a) XRD scans for the 20 nm Mn_3Ga samples deposited under different bias voltage. (b) XRD scans for the 20 nm Mn_3Ga samples deposited under elevating growth temperature.

The samples for detailed study were grown on 16×16 mm^2 Si(001) substrates at room temperature with a Ta (5 nm) and Pt (35 nm) as a seed layer and were capped with a Ta layer (5 nm) to prevent oxidation using a HiTUS system with a base pressure of 5×10^{-7} mbar. The plasma was generated by a radio frequency (RF) field of 13.56 MHz in an Ar atmosphere of 3×10^{-3} mbar [109]. As mentioned in Chapter 3, the crystallisation of Heusler antiferromagnetic films are strongly dependent on the seed layer and substrate. Platinum was used as a seed layer due to its good lattice match to Mn_3Ga [77]. The (0001) plane of Mn_3Ga aligns the (111) plane of Pt with a small lattice mismatch of 2%, as shown in Figure 7.9 (a) and (c).

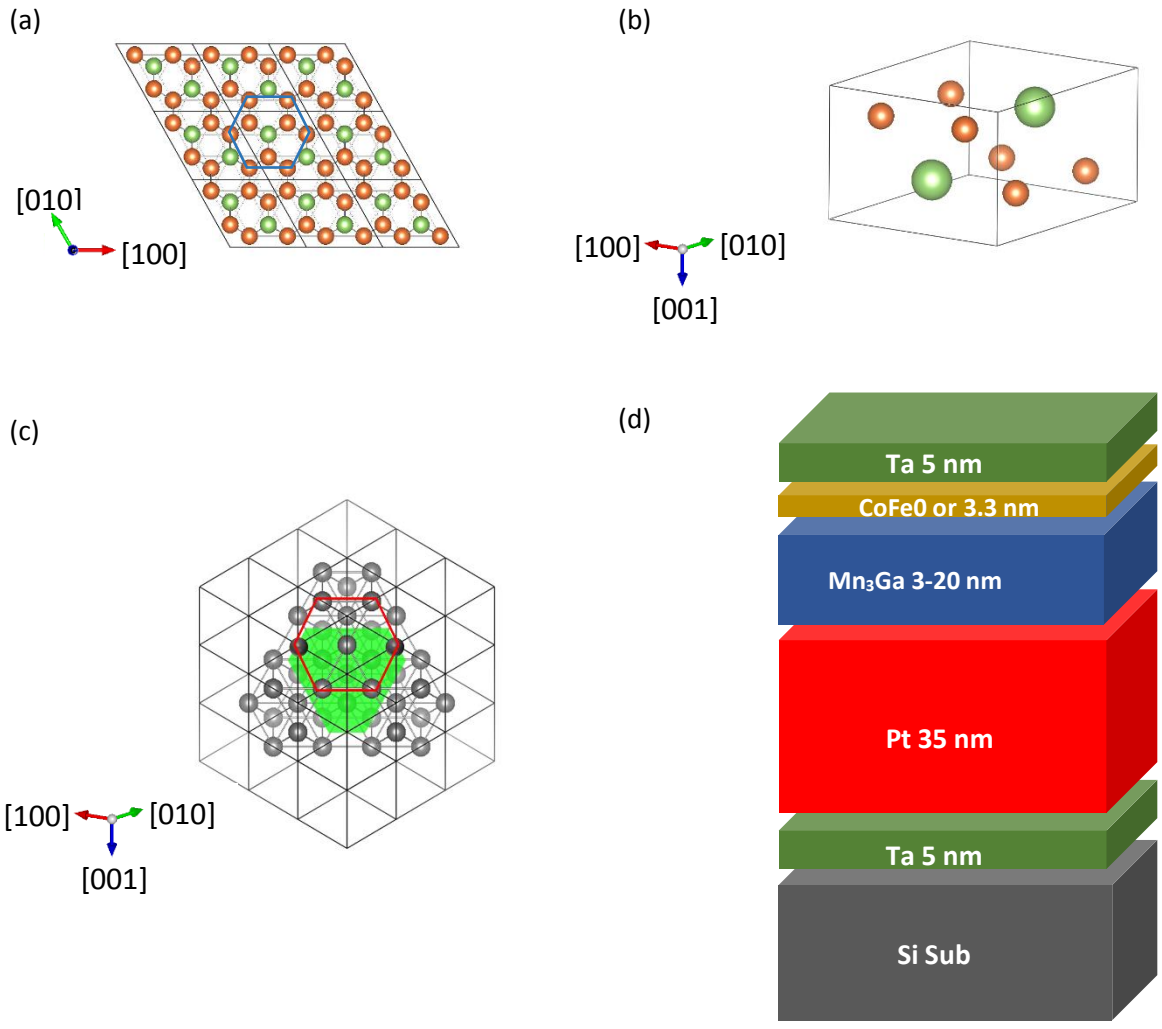

Figure 7.9 (a) projection of $D0_{19}$ hexagonal Mn_3Ga along the (0001) plane, (b) schematic diagram of Mn_3Ga unit cell, (c) schematic diagram of cubic Pt along the (111) plane and (d) schematic diagram of the Mn_3Ga film deposited.

The 16 × 16 mm^2samples were first characterised by XRD in order to confirm the crystal structure of the Mn_3Ga layers. A Rigaku SmartLab X-ray diffractometer was used in this study. This apparatus employs the use of a high intensity 9 kW rotating anode X-ray generator. It operates with a voltage of 45 kV and a current of 200 mA. A Cu target was used as the X-ray source which generates a beam with $K\alpha_1$ and $K\alpha_2$ X-rays whose wavelengths are 1.541Å and 1.544 Å, respectively. Germanium is used in the incident monochromater crystal system, which allows for the diffraction of X-rays. Ge(220)×2 crystals were fitted to produce monochromatic X-rays by diffracting them twice by the Ge(220) lattice planes. Passing X-rays through this crystal makes it possible to use only $K_{\alpha 1}$ X-rays with approximately 0.003° divergence. Large sample size is used in order for the X-ray diffractometer to increase the signal to noise ratio. A comparison between two sets of samples with different substrate size measured using different conditions is shown in Figure 7.10.

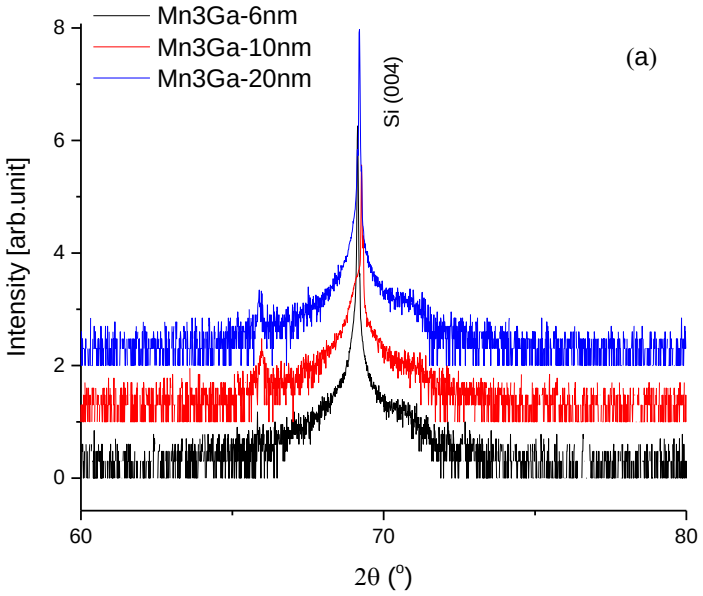

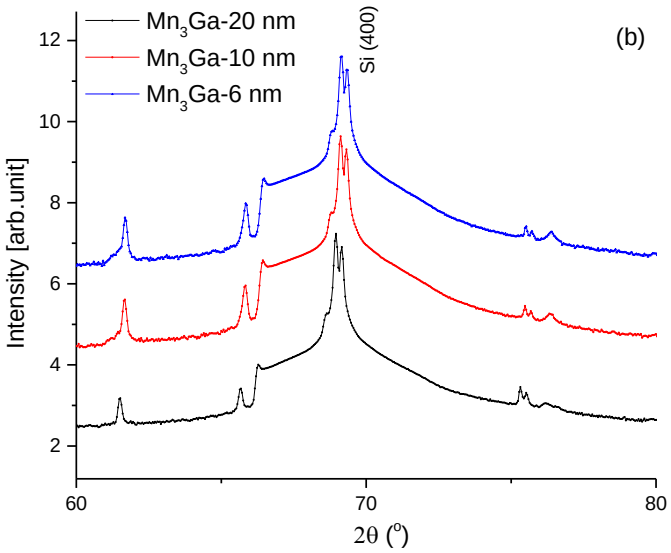

Figure 7.10 (a) 16 × 16 mm^{2}samples measured using Ge(220)×2 crystals monochromater. (b) 5 × 5 mm^{2}samples measured without Ge(220)×2 crystals monochromater.

The multi peaks around Si(400) in Figure 7.10(b) are the reflection peak of Si(400) from the X-ray sources with different wavelength. When the Ge(220)×2 crystals monochromater is used as shown in Figure 7.10(a), the multi reflection peaks are filtered leaving a clean Si(004) single peak. The red line from Figure 7.10(b) is shifted slightly to the left due to misalignment during the measurement.

The samples grown at room temperature at a 900 V bias voltage are measured in air. θ-2θ XRD scans indicate the variation in the degree of the crystallisation with respect to different thicknesses of the Mn_3Ga layers from 6 nm to 20 nm as shown in Figure 7.11.The XRD spectra show that, as the thickness of Mn_3Ga layer increases, the (0002) and (0004) peaks become more intense and sharper. This is because thicker Mn_3Ga layers provide stronger signals. The 20 nm thick Mn_3Ga film shows a clear (0002) peak at 41.3° as shown in Figure 7.11. By splitting Pt(111) and Mn_3Ga(0002) peak, it is clear that as the AF thickness decrease from 20 nm to 6 nm the FWHM of the peaks linearly increase from 0.62° to 0.943°as shown in Figure 7.11 (b). Hence the average grain size decrease from 15.2 nm to 10.0 nm using Scherrer analysis. When the Mn_3Ga layer thickness is reduced to 6 nm the signal is too weak to distinguish the (0002) peak from the Pt(111) peak. A pole figure scan is required for to confirm the crystallinity

as shown in Figure 7.11(c) for the 6 nm Mn_3Ga film. From the pole figure scan for the 6-nm-thick Mn_3Ga film, the central peak confirms the presence of $Mn_3Ga(0002)$ peak at 41.3°, corresponding to the hexagonal $D0_{19}$ phase. According to the distance from the outer ring to the centre spot, the in-plane rotation angle alpha is found to be 19.0° which indicates the outer ring represents the Pt(111) with polycrystalline nature. It should be noted that the central $Mn_3Ga(0002)$ peak is well separated from that of the Pt(111).

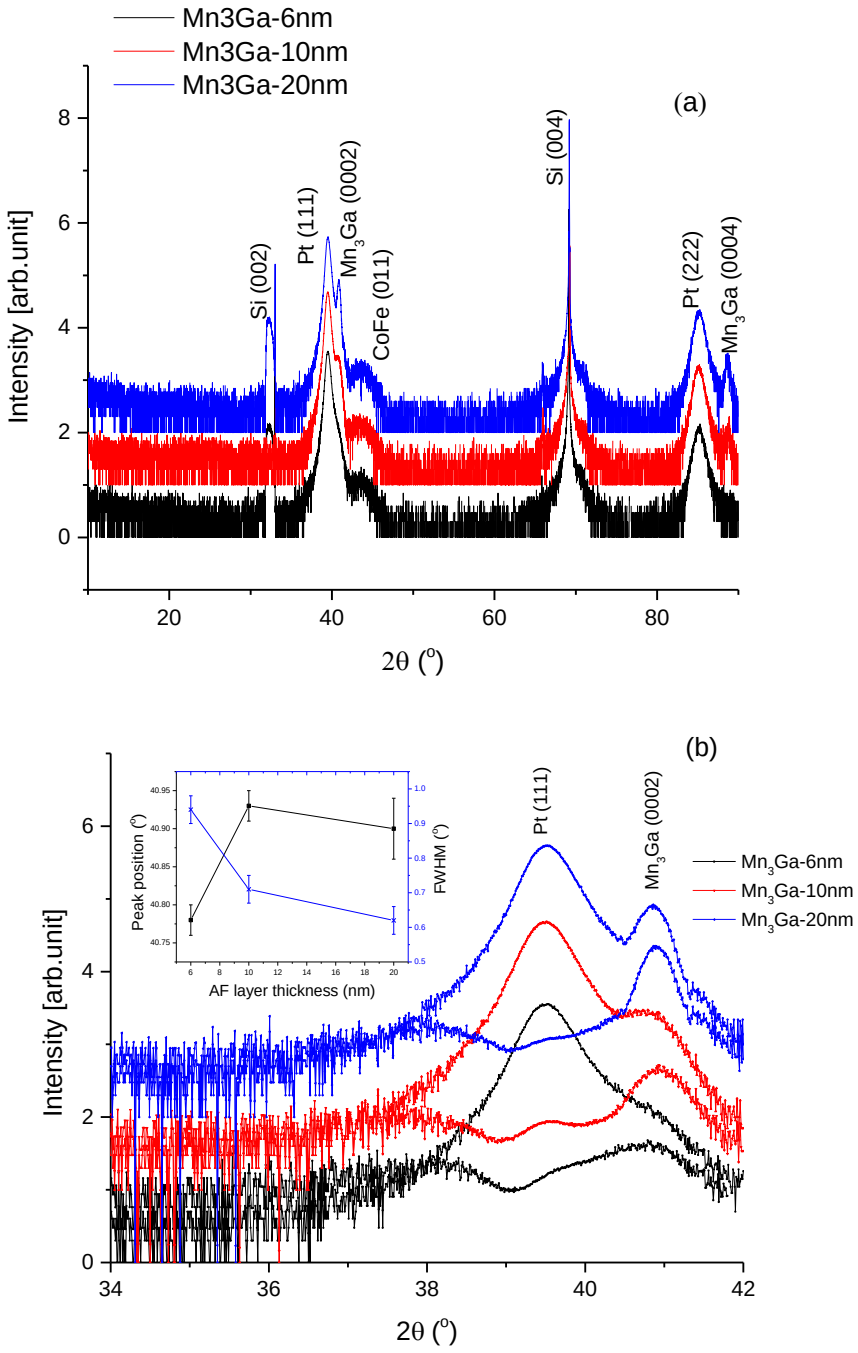

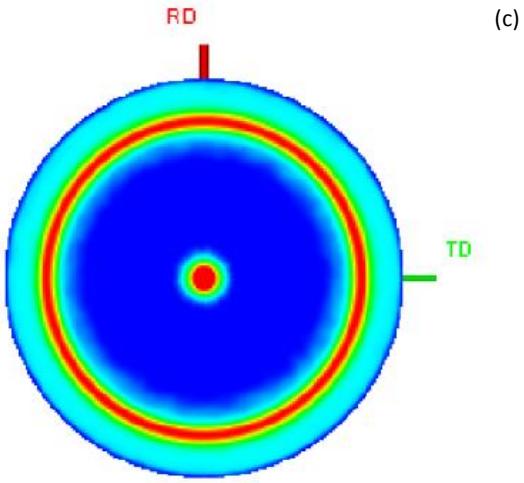

Figure 7.11 (a) XRD scans for the Mn_3Ga samples with different thicknesses (CoFe thickness of 3.3 nm). (b) Separated Mn_3Ga (0002) peak intensities. (c) Pole figure scan at 41.45° for the 6-nm-thick Mn_3Ga film.

The Mn_3Ga layer has been reported to be stabilised in a hexagonal $D0_{19}$ crystal structure ε-Mn_3Ga with antiferromagnetic behaviour [41]. The lattice parameters of the Mn_3Ga films in the $D0_{19}$ and $D0_{22}$ phases are listed in Table 7.3. From the XRD scan, it is proved that the sample has purely $D0_{19}$ antiferromagnetic phase. For comparison with Mike Coey's paper on epitaxial Mn_3Ga films grown at high temperature [77], the polycrystalline Mn_3Ga film grown at room temperature in our work shows similar degree of crystallinity. The lattice parameter c calculated using XRD scan in this work is 0.441 nm which agrees with the value calculated by Kurt *et al*, [77].

Table 7.3 Comparison between the $D0_{19}$ and $D0_{22}$ phases of Mn_3Ga.

Structure	Hexagonal $D0_{19}$	Tetragonal $D0_{22}$
Magnetic phase	Antiferromagnetic	Ferrimagnetic
Lattice parameter	a = 0.540, c = 0.436 nm [77]	a = 0.391, c = 0.712 nm [72]
2θ observed	41.30° (0002) 89.9° (0004)	N/A

According to Meiklejohn and Bean [52] (see Chapter 4.1.2) exchange coupling is induced at the sharp interface between AF/F layers. X-ray reflectivity (XRR) measurements are carried out for the 6-nm-thick-Mn_3Ga film confirming the presence of a sharp interface between the Mn_3Ga and FeCo layers as shown in Figure 7.12. Using the GenX software [114] to fit the data, the estimated thicknesses are: Ta (6.0±0.4) nm/Pt (34±2) nm/Mn_3Ga (5.8±0.9) nm/CoFe (4±1) nm/Ta (4±1) nm.

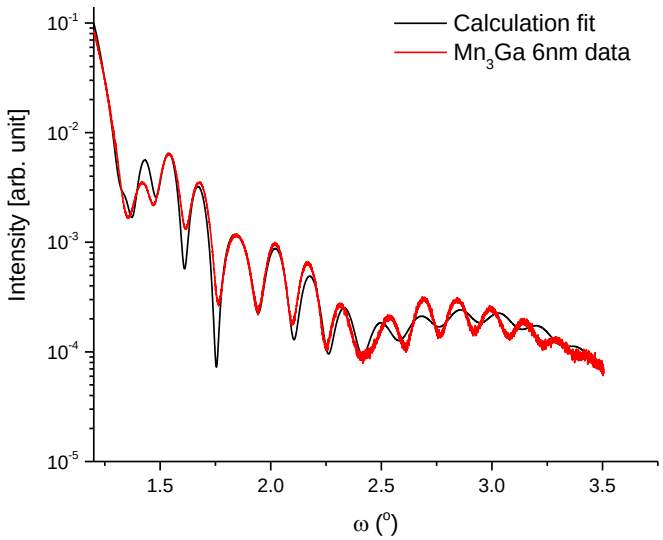

Figure 7.12 XRR scan for the 6-nm-thick Mn_3Ga/3.3-nm-thick CoFe film.

To ascertain the role of the grain size, we carried out grain size analyses using TEM (JEOL JEM-2011 TEM). A Lanthanum hexaboride (LaB_6) filament is fitted at the top of the apparatus which is operated under high vacuum of 10^{-8} Pa. The 6 nm thick Mn_3Ga was deposited on a carbon coated copper TEM grids using a HiTUS sputtering system. More than 500 individual grains were measured which followed a lognormal distribution as shown in Figure 7.13. The mean grain size was measured to be 13.2 nm with a standard deviation of 0.4.

(a)

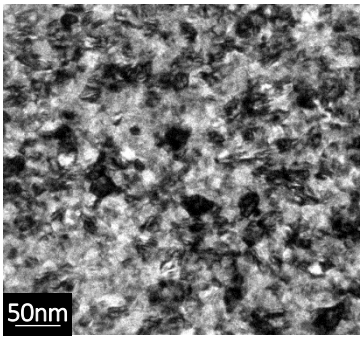

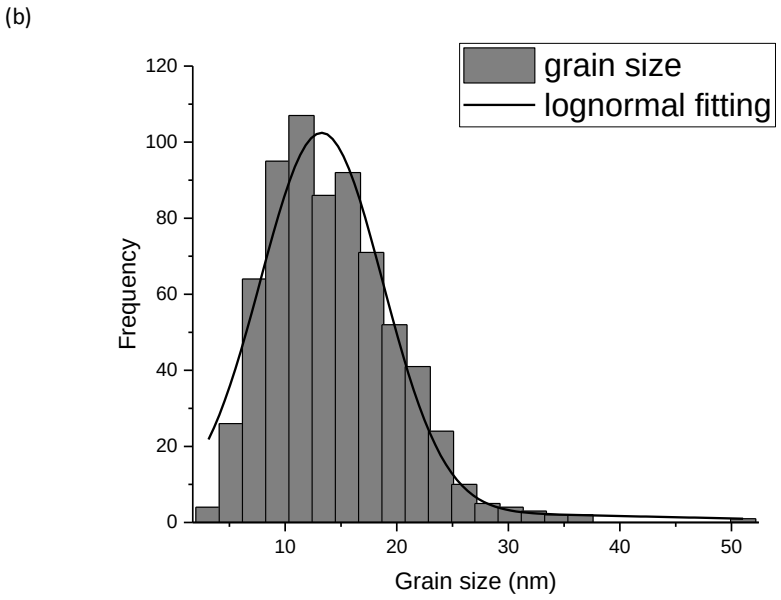

Figure 7.13 (a) Plan-view TEM image for grain size analysis for the 6 nm thick Mn_3Ga thin film. (b) Grain size distribution for the 6 nm thick Mn_3Ga thin film sample.

7.5 Magnetic Characterisation of Polycrystalline Mn_3Ga

The magnetic characteristics of the Mn_3Ga samples were measured using a Model 10 Microsense VSM, and X-ray photoemission electron microscopy (XPEEM). The 20-

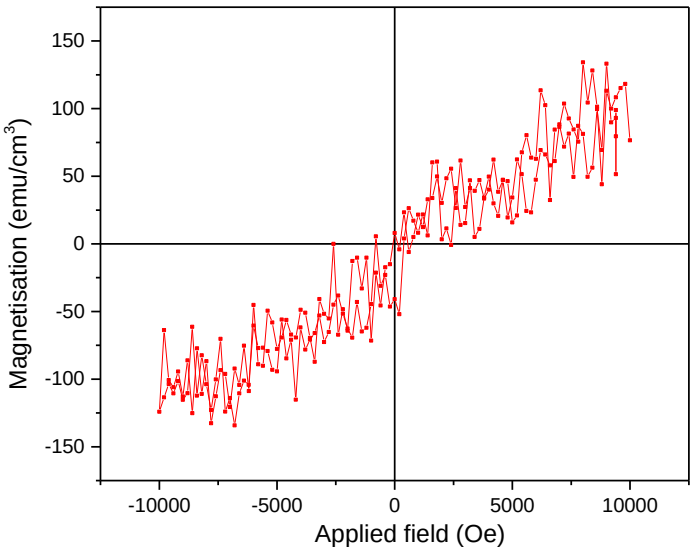

Figure 7.14 Magnetisation curve for polycrystalline Mn_3Ga (20 nm)/Pt (5 nm) films measured at room temperature.

nm-thick Mn_3Ga film with a 5-nm-thick Pt capping layer grown at elevated temperatures showed weak paramagnetic behaviour at room temperature.

As shown in Figure 7.14, no hysteresis loop is found which indicates that the paramagnetic behaviour observed is likely produced by the Pt layer and hence Mn_3Ga layer is confirmed to be antiferromagnetic.

As mentioned in Chapter 5, exchange bias is the consequence of an interfacial exchange interaction between the AF and F materials. Hence a ferromagnetic layer was deposited above the Mn_3Ga. Two ferromagnetic Co and $Co_{0.6}Fe_{0.4}$ alloys are used and compared. The magnetisation curves are shown in Figure 7.15. It is very clear that the sample with CoFe layer exhibits larger coercivity and exchange bias compared to that with the Co layer.

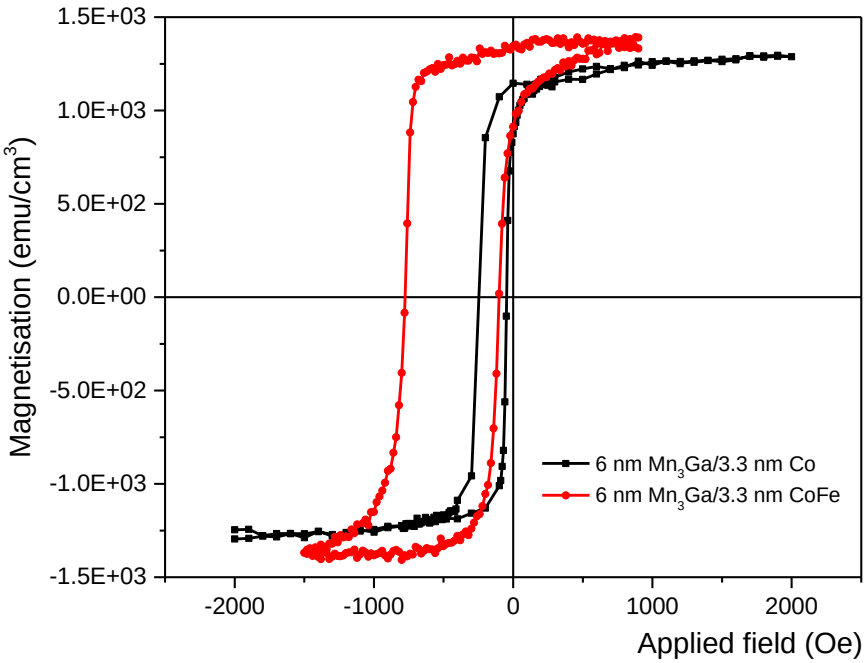

Figure 7.15 Magnetisation curves for the polycrystalline Mn_3Ga (6 nm)/$Co_{0.6}Fe_{0.4}$ (3.3 nm) (red line) and Mn_3Ga (6 nm)/Co (3.3 nm) (black line) films measured at 120 K.

The magnetisation curves for the $Mn_3Ga/Co_{0.6}Fe_{0.4}$ samples measured at 120 K after setting at 500 K under an applied magnetic field of 20 kOe are shown in Figure 7.16. As can be seen, all *M-H* curves are shifted horizontally, which demonstrates the presence of exchange bias in the system. In order to achieve the largest exchange bias, the AF/F layer thicknesses have been optimised.

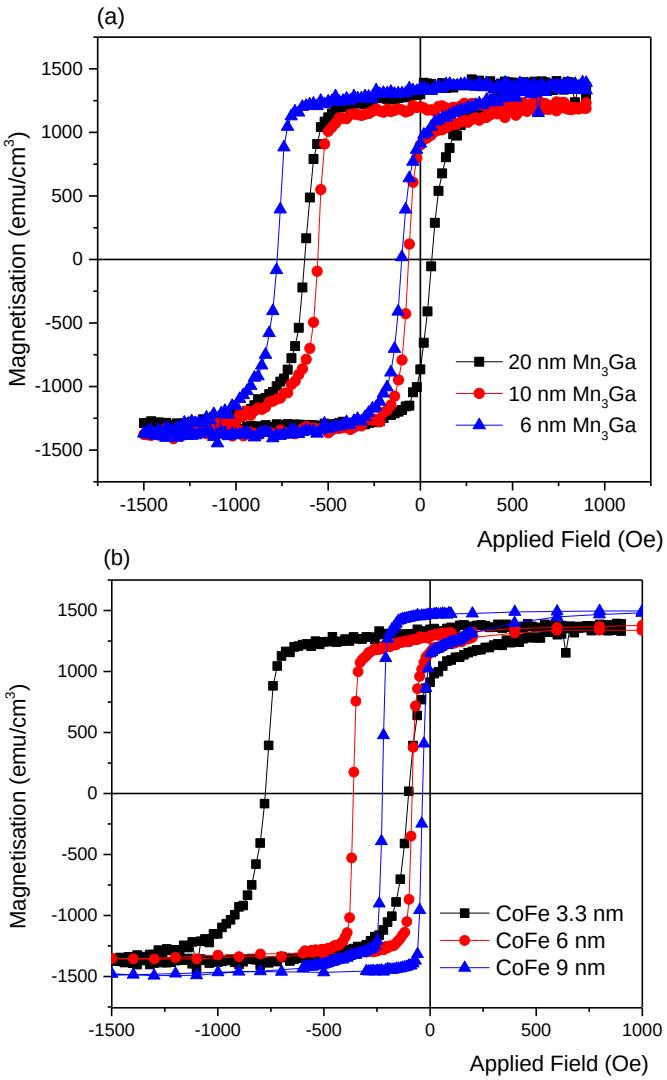

Figure 7.16 (a) Magnetisation curves for the polycrystalline $Mn_3Ga/Co_{0.6}Fe_{0.4}$(3.3 nm) films with different Mn_3Ga thicknesses of 6 (blue line), 10 (red line) and 20 nm (black line) measured at 120 K. (b) Magnetisation curves for the polycrystalline Mn_3Ga (6 nm)/$Co_{0.6}Fe_{0.4}$ films with different CoFe thicknesses of 3.3 (black line), 6 (red line) and 9 nm (blue line) measured at 120 K.

The 6-nm-thick Mn_3Ga film shows the largest exchange bias of 430 Oe at 120 K. The saturation magnetisation of the $Mn_3Ga/Co_{0.6}Fe_{0.4}$ sample, (1300 ± 100) emu/cm^3, arises from the 3.3-nm-thick ferromagnetic $Co_{0.6}Fe_{0.4}$ layer, since the individual Mn_3Ga layer shows no magnetisation between 100 and 300 K. Hence the observed magnetisation can be attributed to that of the $Co_{0.6}Fe_{0.4}$ layer only, which is very close to the bulk value for $Co_{0.6}Fe_{0.4}$ (1450 emu/cm^3) [21]. For the 10- and 20-nm-thick films, the exchange bias is measured to be 299 and 270 Oe, respectively. By increasing the Mn_3Ga thickness, the exchange bias is found to decrease. Such effect can be due to a combinations of factors: on the one hand, at small thicknesses, one may expect a larger seed-layer-induced strain, which may lead to an increased magnetocrystalline anisotropy in Mn_3Ga. At larger thicknesses, strain relaxation sets in, leading to rougher interfaces and possible reduction in the anisotropy, hence to a smaller exchange bias. In addition, the grain volume also has strong impact. As the results shown from XRD measurement, thicker AF films have larger grain volume which cannot be set by the setting, hence the exchange bias goes down [14]. For a fixed Mn_3Ga thickness (6 nm), it is found that, as the thickness of $Co_{0.6}Fe_{0.4}$ increase from 3.3 nm to 9 nm, the exchange bias decreases significantly from (430 ± 5) Oe to (130 ± 5) Oe, as seen in Figure 7.16(b). This is in agreement with other studies, where a thin ferromagnetic layer attached to an AF layer with good crystalline ordering maximises the interfacial exchange coupling $H_{ex} \propto \frac{1}{t_F}$ [134]. Table 7.4 summarises the values of the exchange bias for all samples studied. The error of the results in Table 7.4 comes from the measurement step size, 10 Oe, was used during the measurement hence the error was considered to be half of the step size, *i.e.*, 5 Oe.

Table 7.4 Values of exchange bias with different layer thicknesses.

$Mn_3Ga/Co_{0.6}Fe_{0.4}$	Exchange bias ($\pm$ 5 Oe)
3 nm/3.3 nm	47
6 nm/3.3 nm	430
10 nm/3.3 nm	299
20 nm/3.3 nm	270
6 nm/2 nm	385
6 nm/3.3 nm	430
6 nm/ 6 nm	223
6 nm/ 9 nm	130

In order to determine the blocking temperature (T_B), *i.e.*, the point at which the exchange bias vanishes, the activation temperature must be considered. This is usually carried out by raising the activation temperature until the loop shift becomes zero. In polycrystalline systems a single grain has a unique T_B. Figure 7.17 illustrates T_B measured using the York Protocol [17]. In order to ensure that no magnetic history affects the measurements, the sample temperature is set to T_{SET} = 500 K (lower than T_N) for 90 minutes under an external field of 20 kOe, and then cooled to T_{NA} = 100 K. The external field is then reversed to -20 kOe, and the samples are then thermally activated at a temperature between 100 K and 350 K for 30 minutes. The sample is then cooled down to 100 K and the hysteresis loop is measured. The result of a sequence of such measurements for the 6-nm-thick Mn_3Ga sample is shown in Figure 7.17. The data clearly shows the evolution of the loop shift from a negative magnetic field shift of -430 Oe to a positive field value of 500 Oe by increasing the activation temperature from 100 K to 350 K. The loop shift is caused by the reorientation of the magnetisation of the Mn_3Ga/CoFe bilayer with the individual Mn_3Ga grains due to the thermal activation in a negative field. By increasing the activation temperature, the magnetisation in smaller grains can be reversed [19]. Therefore, the temperature where

the exchange bias becomes zero represents the equilibrium state between the total volume of the grains aligned along the initial magnetic field and that of the grains reversed by the thermal energy induced by the increase in temperature. This is the

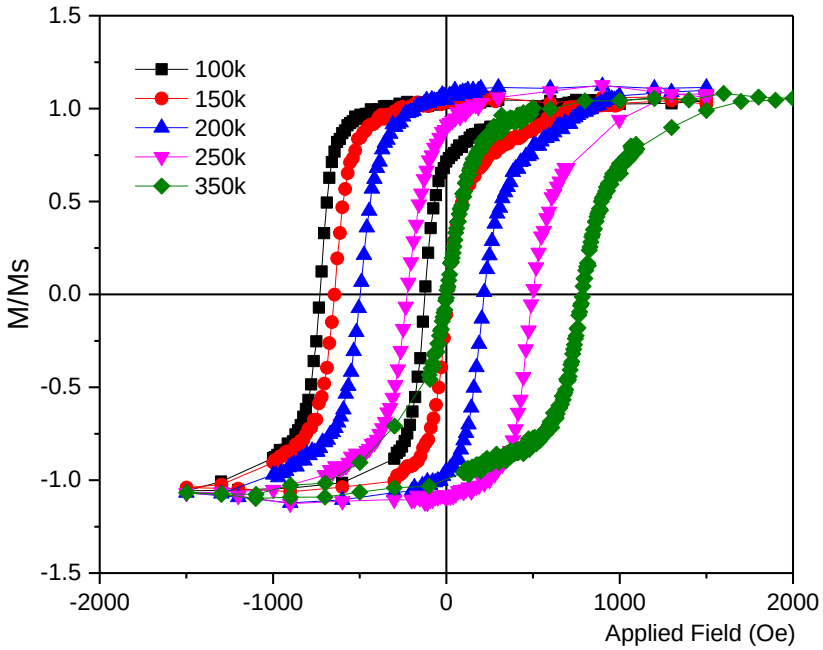

Figure 7.17 Magnetisation curves for the 6-nm-thick $Mn_3Ga/Co_{0.6}Fe_{0.4}$ film for different activation temperatures between 100 K and 350 K.

definition of the median blocking temperature of an antiferromagnetic material. $<T_B>$ for the 6-nm-thick Mn_3Ga sample is estimated to be (225 ± 5) K.

The blocking temperature for the other thickness films are also measured as shown in Figure 7.18. Noteworthy, there is an artefact at zero field for the 10 nm sample in Figure 7.18(a). This is because of the sample surface contamination during the measurement. The artefact is disappeared after placing the sample in acetone acid clean for 30 minutes and then washing the acetone residual using isopropanol efficiently removed the contamination from the sample. The sample was re-measured at activation temperature 125 K, the results are shown in Figure 7.18(c). It is worth to note that, the artefact near zero field does not affect the magnitude of exchange bias and saturation magnetisation, hence the results are still reliable.

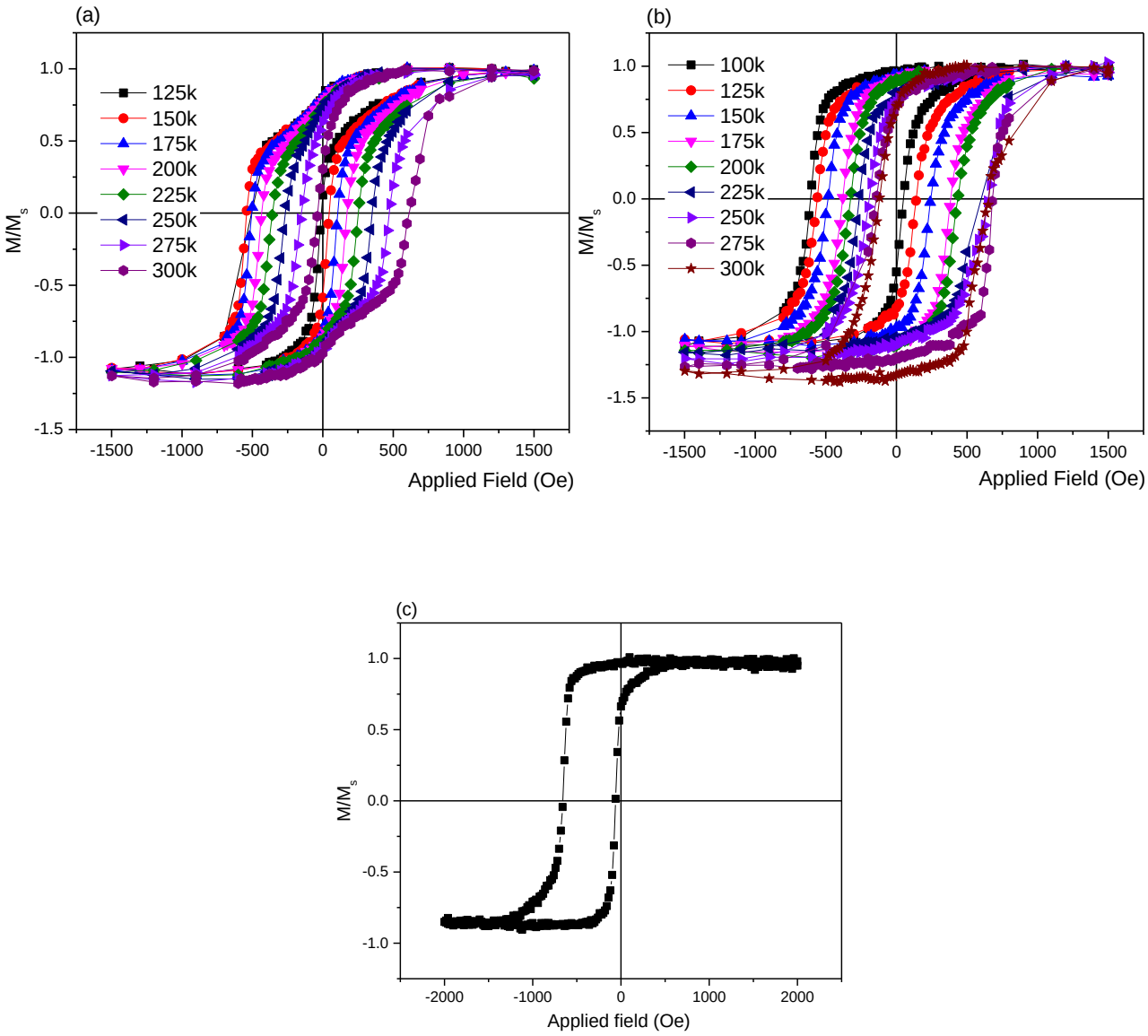

Figure 7.18 Magnetisation curves for the (a) 10-nm-thick and (b) 20-nm-thick $Mn_3Ga/Co_{0.6}Fe_{0.4}$ films for different activation temperatures between 100 K and 300 K. (c) Magnetisation curve for the 10-nm thick $Mn_3Ga/Co_{0.6}Fe_{0.4}$ film after cleaning in acetone for 30 minutes and measured with activation temperature set to be 125 K.

Figure 7.19 shows that the exchange bias varied monotonically as a function of the thermally activating temperature. Interestingly, the blocking temperature is found to decrease when the Mn_3Ga thickness is increased, from (235±5) K for the 10-nm-thick film to (175±5) K for the 20-nm-thick film. A possible explanation is that this may be attributed to the larger textured strain by the Pt buffer layer (as shown in the embedded

graph within Figure 7.11 (b), the peak position shifts as the AF thickness decreases) and a smoother interface at smaller Mn_3Ga thicknesses. These results indicate that the quality of the $Mn_3Ga/Co_{0.6}Fe_{0.4}$ interface controls the exchange bias. For the 6-nm-thick Mn_3Ga, a reduction in the blocking temperature is found, which is attributed to reduction in the total magnetic anisotropy of the Mn_3Ga due to the reduced thickness [14]. Nevertheless, the 6-nm-thick Mn_3Ga induces the largest exchange bias of 430 Oe at 120 K.

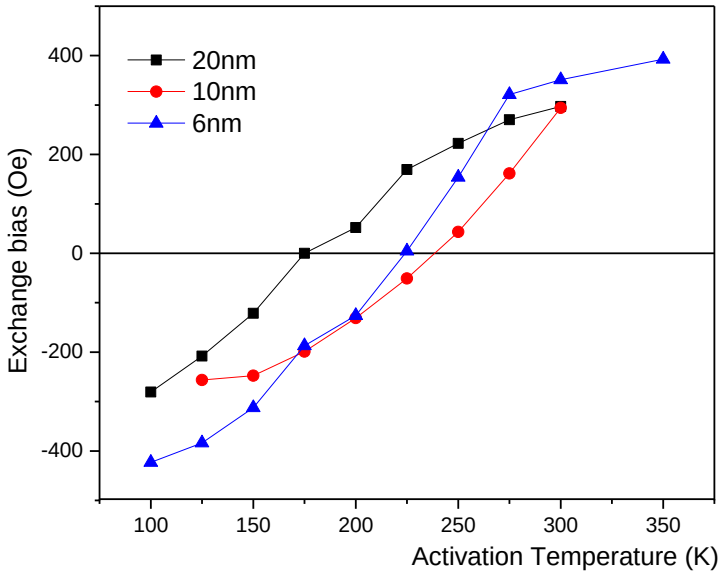

Figure 7.19 Temperature dependence of exchange bias determined for the $Mn_3Ga/Co_{0.6}Fe_{0.4}$ films with the Mn_3Ga thickness of 6, 10 and 20 nm.

It is worth noting that there is a large difference between the Néel temperature (470 K) [65] and measured blocking temperature $<T_B>$ of Mn_3Ga, which may be related to the weak anisotropy and a small grain size. Combining the grain size analysis showed in the previous section 7.1 and the blocking temperature value, the magneto-crystalline anisotropy K_{AF} can be estimated.

As mentioned in Chapter 6, for the case when the sample is thermally stable at the temperature of measurement and has been fully set, the magneto-crystalline anisotropy can estimated using the expression [90]:

$$K_{AF}(< T_B >) = \frac{ln(1800 f_0) k T_B}{< V >} \qquad (7\text{-}2)$$

where K_{AF} indicates the magneto-crystalline anisotropy, $< T_B >$ is the median blocking temperature, f_0 is an attempt frequency generally taken to be 10^9 s^{-1} and V is the median grain volume. In reality, not all the sample is thermally stable at the measurement temperature (100 K) hence those grains will not be taken into account during the calculation. The anisotropy value was calculated to be $9 \times 10^4 J/m^3$. For comparison, the value for IrMn is almost two orders of magnitude higher. This leads to lower the blocking temperature for the Mn_3Ga samples.

For comparison with the paper on epitaxial hexagonal Mn_3Ga films grown at high temperature by Kurt *et al.* [77], the 20-nm-thick Mn_3Ga film shows an exchange bias of 240 Oe at 300 K; whereas in our work an exchange bias of 430 Oe was observed at 100 K with much thinner AF layer thickness (6 nm). Similar coercive field about 500 Oe is also observed in both works.

In addition, X-ray photoemission electron microscopy (XPEEM) measurements were carried out at the SIM beamline at the Paul Scherrer Institute (PSI). In this technique, fully polarised X-ray light illuminates the sample homogeneously, and high resolution images of the local photo-emitted electron intensity of the sample, which is proportional to the X-ray absorption, are recorded. Using circularly-polarised light and the X-ray circular magnetic dichroic effect and the elemental sensitivity of X-rays, separate magnetic contrast images of different layers can be obtained sequentially on the very same region of the sample. Magnetic contrast images of a Mn_3Ga (6 nm)/CoFe (2nm) sample were obtained at the Co and Mn L_3 edges at 150 K to probe the CoFe and Mn_3Ga layers simultaneously. As shown in the Figure 7.20, strong magnetic contrast in the CoFe layer is found, as expected for such a ferromagnetic material. The different black and white regions correspond to areas with opposite magnetisation, showing the presence of a multi-domain state. When probing the Mn L_3 edge, the presence of a clear magnetic contrast is found which correlates exactly to that of the CoFe layer, showing the presence of a spin-polarised Mn_3Ga layer at the interface. This suggests the formation of an uncompensated Mn_3Ga interface spin layer in these films which agrees with the large exchange-bias effects observed in this system.

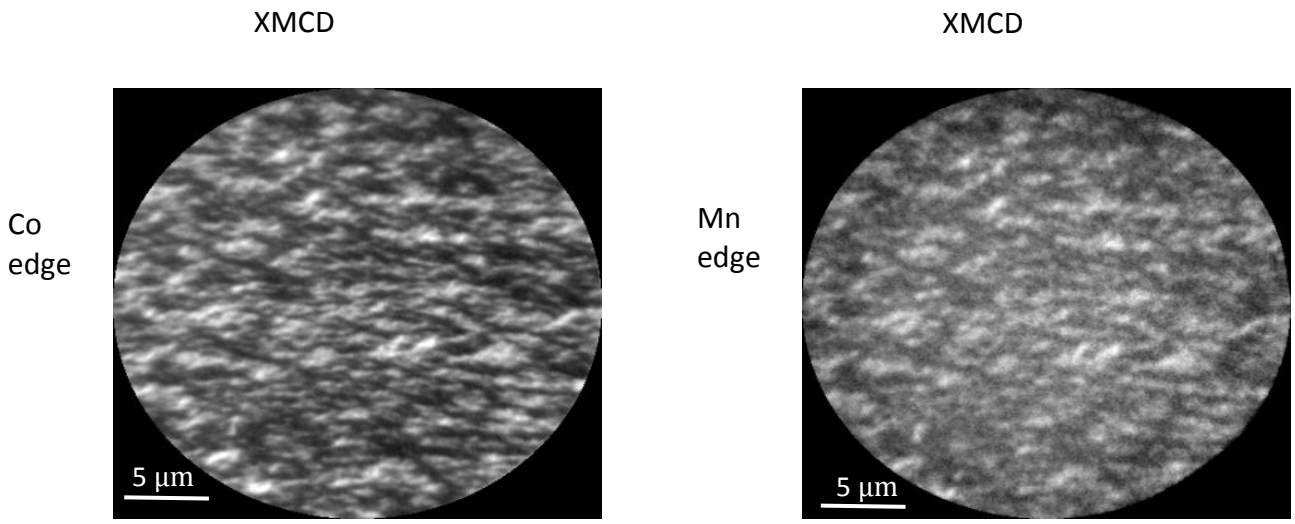

Figure 7.20 Magnetic contrast images of the Mn_3Ga (6 nm)/CoFe (2 nm)/Al (2nm) sample taken at the Co edge and Mn edge at 150 K (The image field of view is 25µm).

We also acquired detailed X-ray absorption spectroscopy (XAS) spectra at room temperature using both right and left circularly-polarised light, from which we can obtain local XMCD spectra can be obtained at a single domain region on the Mn_3Ga (6 nm)/CoFe (2 nm)/Al (2nm) sample. The capping layer was replace with Al because Ta has high atomic number which absorbs electrons quite strongly. Figures 7.21(a) and (b) show the XAS spectra taken at the Mn and Co edge with right (C+) and left (C-) circular polarisations. Figure 7.21(a) indicates the L_3 photon energy of Co is around 782.2 eV. Figure 7.21(b) indicates the L_3 photon energy of Mn is around 642.6 eV. The subtraction of these two signals provide XMCD spectra as shown in Figure 7.21(c) and (d). For the Co spectrum, one can clearly see the domain structure using right-circularly-polarised light at L_3 and L_2 edges as shown in Figure 7.21(e). An example of spectra at C+ and C- for the region marked with a blue circle is given in Figure 7.21(c). For the Mn spectrum, the domain structure is also available at the L_3 edge and the corresponding XMCD spectrum can also be observed.

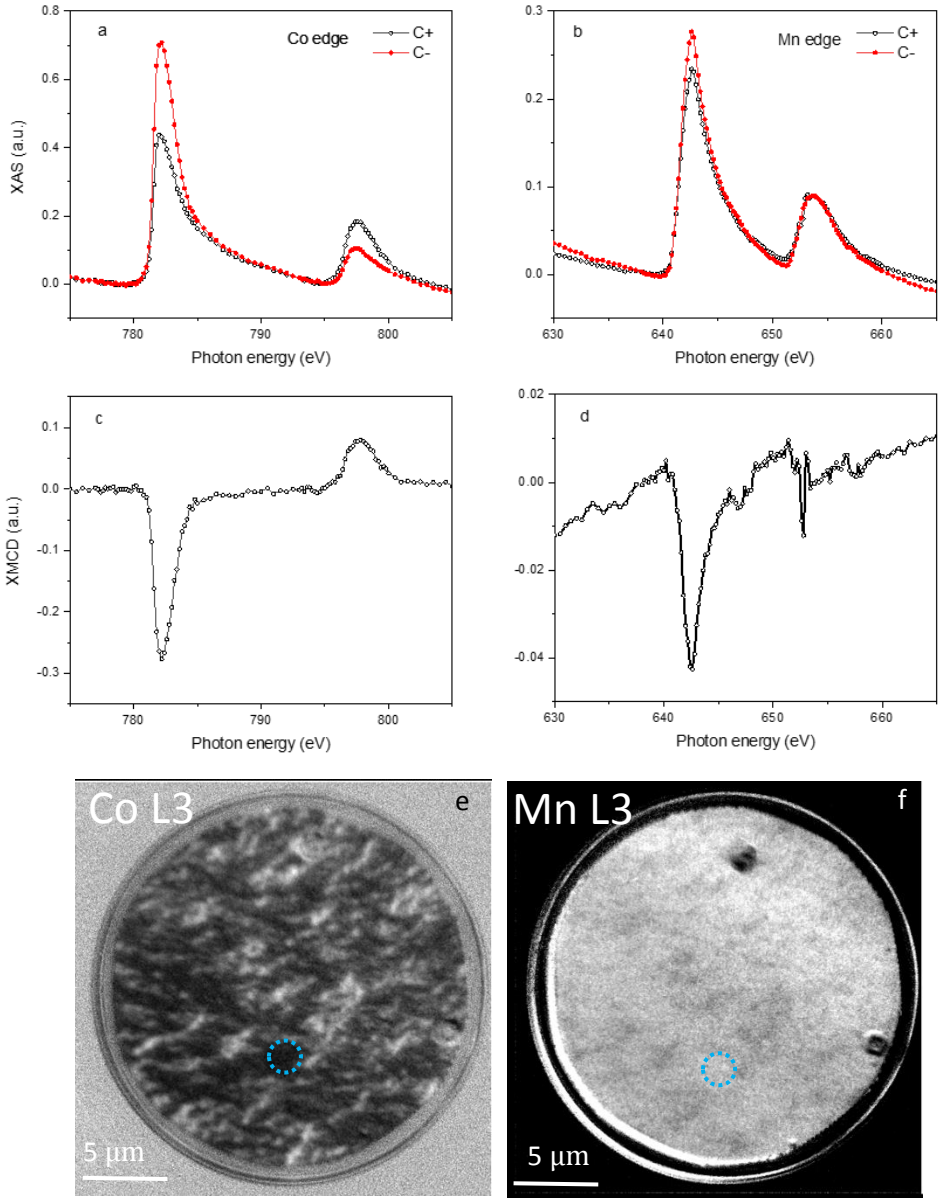

Figure 7.21 (a) and (b) XAS, and (c) and (d) XMCD spectra of the Co and Mn edges in the Mn_3Ga (6 nm)/CoFe (2 nm) sample, respectively. The corresponding XMCD images of (e) Co L_3 and (f) Mn L_3 edges (The image field of view is 25µm).

In the Mn_3Ga (6 nm)/CoFe (2 nm)/Al (2 nm) orbital (m_{orb}) and spin (m_{spin}) magnetic moments of Mn and Co can be estimated from XMCD spectra using the Sum Rules [127].

$$m_{orbital} = -\frac{4q}{3r}(10 - n_{3d}) \qquad (7\text{-}3)$$

$$m_{spin} = -\frac{6p - 4q}{r}(10 - n_{3d})(1 + \frac{7 < T_z >}{2 < S_z >})^{-1} \quad (7\text{-}4)$$

$$m_{total} = m_{orbital} + m_{spin} \quad (7\text{-}5)$$

As it has been discussed in Chapter 6, m_{total}, $m_{orbital}$ and m_{spin} are the total magnetic moment, orbital magnetic moment and spin magnetic moment respectively. $< T_z >$ is the expectation value of the magnetic dipole operator and $< S_z >$ is equal to a half of m_{spin} in Hartree atomic unit. The sum rule constant, *p*, *q*, and *r* are determined from Figure 7.22 which correspond to the integral of the dichroism spectra for the L_3 edge, the integral of the dichroism spectra over both the L_3 and L_2 edges and the area of the summed XAS signal after removal of a stepped background respectively. In this work, we have used the n_{3d} values from C. T. Chen *et al*. [126], 5.0 for Mn and 7.51 for Co, are used to calculate the spin and orbital moment. The results are shown in Table 7.5. The orbital and spin moments of Co are estimated to be (0.299$\pm$0.005) μ_B /atom and (1.268 $\pm$ 0.005) μ_B /atom respectively. The total moment of Co is calculated to be (1.57$\pm$0.01) μ_B/atom which agrees with the theoretical value of 1.60 μ_B /atom [135]. The orbital and spin moments of Mn are also estimated to be (0.270$\pm$0.005) μ_B/atom and (0.320$\pm$0.005) μ_B/atom respectively. The total moment of Mn is calculated to be (0.59$\pm$0.01) μ_B/atom which is within the literature value of (0.5-2.8) μ_B /atom [63]. These estimated values represent those in the vicinity of Mn_3Ga/CoFe interface, confirming that the magnetic properties of these layers are not affected by their neighbouring layers.

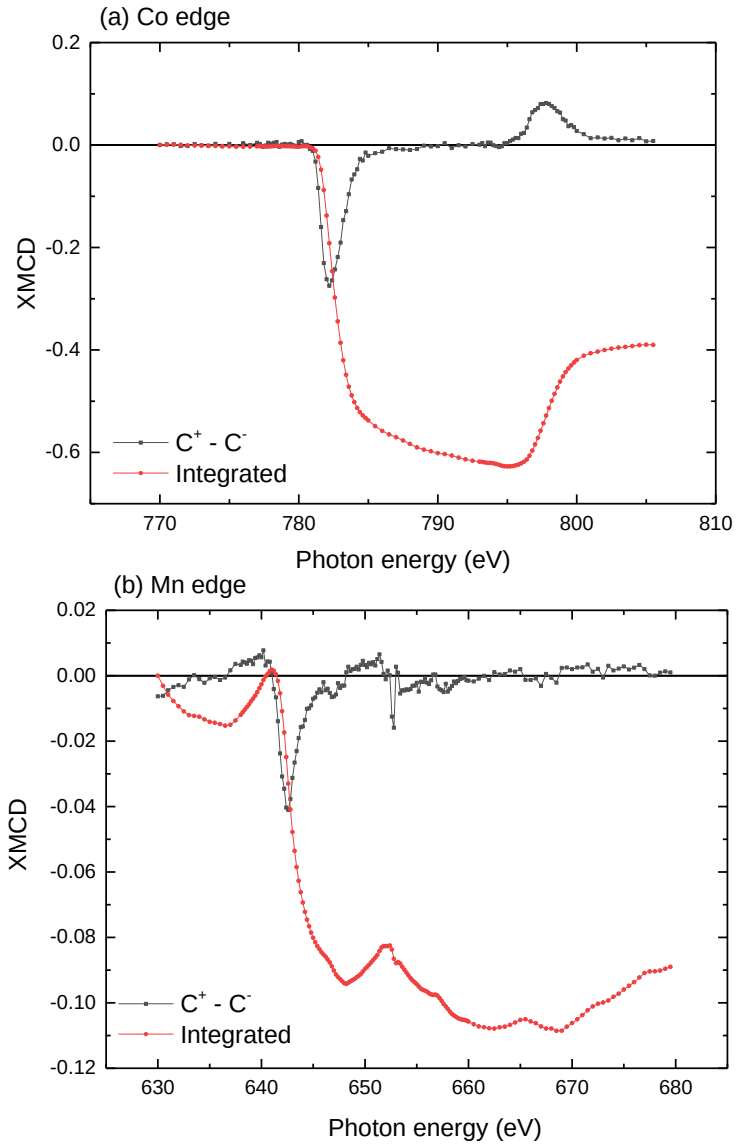

Figure 7.22 XMCD spectra of the (a) Co and (b) Mn edges in the Mn_3Ga (6 nm)/CoFe (2 nm) sample.

Table 7.5 Orbital moments, spin moments and total moment of the Co and Mn from $Mn_3Ga/Co_{0.6}Fe_{0.4}$ bilayer samples in units of μ_B/atom.

Element	Orbital moment (μ_B/atom)	Spin moment (μ_B/atom)	Total moment (μ_B/atom)
Co	0.299±0.005	1.268±0.005	1.57±0.01
Mn	0.27±0.005	0.32±0.005	0.59±0.01

7.6 Structural Characterisation of Polycrystalline Mn_3Ge

Mn_3Ge has very similar physical properties compared with Mn_3Ga as shown in Table 7.6. The XRD scan estimated the lattice constant for $D0_{19}$ Mn_3Ge which resulted a=0.541 nm and c=0.433 nm which agrees with the results reported in Felser's paper [79]. Due to the similarity, the Mn_3Ge samples were grown using the same seed layer and optimised condition as those for the Mn_3Ga samples. Samples with Ta (5 nm)/Pt (35 nm)/Mn_3Ge (3-25 nm)/Ta (5 nm) layer stacks were deposited using HiTUS system at room temperature. As shown in Figure 7.23, as the thickness of AF layer increase from 3 to 25 nm there is no crystallisation in Mn_3Ge observed. Hence, in order to improve the crystallisation samples were deposited under high temperature.

Table 7.6 Comparison between the $D0_{19}$ and $D0_{22}$ phases of Mn_3Ga and Mn_3Ge.

Structure	Hexagonal $D0_{19}$		Tetragonal $D0_{22}$	
Material	Mn_3Ga	Mn_3Ge	Mn_3Ga	Mn_3Ge
Magnetism	Antiferromagnetic	Ferrimagnetic	Antiferromagnetic	Ferrimagnetic
Lattice parameter	a = 0.540 nm, c = 0.436 nm [72]	a = 0.534 nm, c = 0.433 nm [79]	a = 0.391 nm, c = 0.712 nm [72]	a = 0.382 nm, c = 0.726 nm [80]
2θ	41.30 º (0002) 89.9 º (0004)	41.7 º (0002) 44.3 º (201)	-	-
Néel temperature	470 K	390 K	-	-
Currie temperature	-	-	770 K	895 K

It was found that during deposition process, the way samples were annealed strongly effect the crystallisation of the film. The results are compared in Figure 7.24, in sample A consisting of Ta (5 nm)/Pt (35 nm)/Mn_3Ge (100 nm)/Ta (5 nm) all the layers were grown under 500 ℃; whereas in sample B consisting of Ta (5 nm)/Pt (35 nm)/Mn_3Ge (100 nm)/Ta (5 nm) all layers were grown at room temperature except the AF layer was grown at 500 ℃. θ-2θ XRD scans indicate both 100-nm-thick Mn_3Ge samples show a strong $D0_{19}$ hexagonal Mn_3Ge(201) peak around 44°. More interestingly, sample B indicates hexagonal phases with much sharper full width half maximum

(FWHM) than sample A. Single AF layer annealing provides better crystallisation because it effectively avoid the interlayer diffusion due to high temperature annealing. It is shown in Figure 7.24, the left hand side of the $D0_{19}$ (201) peak for sample A is slightly stretched as compared to the theoretical value due to the lattice stretching during high temperature annealing. The theoretical 2θ value can be calculated using the following equations:

For hexagonal structure:

$$d = \frac{1}{\sqrt{\frac{4}{3a^2} \times (h^2 + k^2 + hk) + \frac{l^2}{c^2}}} \tag{7-6}$$

$$\lambda = 2d\sin\theta \tag{7-7}$$

where d is the lattice spacing, a and c are the lattice constants in the plane and perpendicular to the plane, *h,k and l* are the Miller indices and λ is the wavelength of the X-ray source. Using equation (7-6) and (7-7), the bulk 2θ value for $D0_{19}$ Mn_3Ge (0002) peak is calculated to be 41.7°.

For tetragonal structure:

$$d = \frac{a^2}{\sqrt{h^2 + k^2 + l^2}} \tag{7-8}$$

Table 7.7 summarises the observed angle and the corresponding FWHM. In addition, by using the Scherrer grain size analysis, the grain size for Mn_3Ge is estimated (see Table 7.7). Noteworthy, the average grain size for the Mn_3Ge increases significantly from 14 nm to 33 nm, when a single AF layer is heated during deposition. This result indicates that the crystallinity of Mn_3Ge is strongly controlled by the growth temperature and growth method.

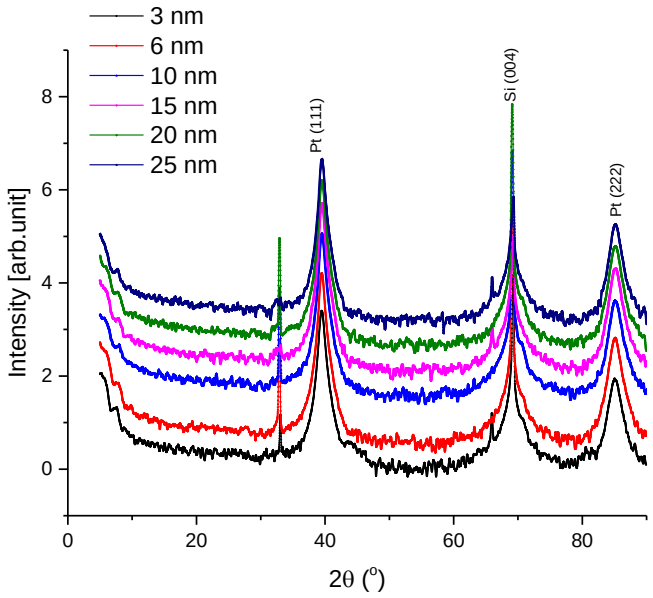

Figure 7.24 XRD scans for the Mn_3Ge samples with different AF thicknesses.

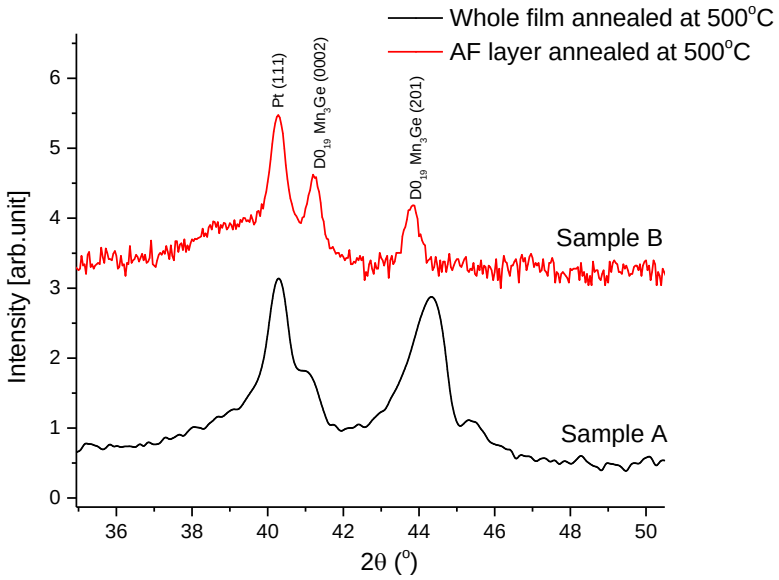

Figure 7.23 XRD scans for sample A consisting of Ta (5 nm)/Pt (35 nm)/Mn_3Ge (100 nm)/Ta (5 nm) grown at 500℃. Sample B consisting of the same structure but only the 100-nm-thick Mn_3Ge layer grown at 500℃ .

Table 7.7 List of FWHM for Mn_3Ge peaks.

	Sample A		Sample B	
2θ observed	40.93° (0002)	44.36° (222)	41.2° (0002)	43.81° (222)
FWHM	0.93°	0.49°	0.24°	0.29°
Grain size	9.5±0.2 nm	18.3±2 nm	36.2±0.2 nm	30.5±0.2 nm

7.7 Magnetic Characterisation of Polycrystalline Mn_3Ge

The magnetic characteristics of the Mn_3Ge samples are measured using a Microsense VSM. To begin with, a sample with a single layer of 100-nm-thick Mn_3Ge and 5-nm-thick Ta capping layer is measured at room temperature.

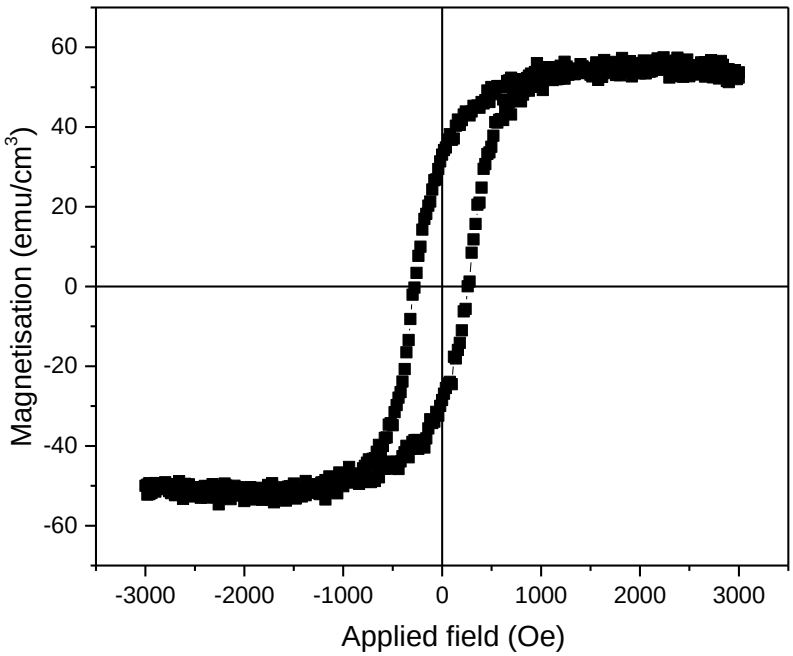

Figure 7.25 Magnetisation curve for the polycrystalline Mn_3Ge (100 nm)/Ta (5 nm) film measured at room temperature.

Figure 7.25 shows that the film exhibits partial ferrimagnetic behaviour with a saturation magnetisation value of 54 emu/cm^3. Noteworthy, the saturation magnetisation value for a single layer Mn_3Ge film from literature is about 100 emu/cm^3 [136]. Although there is approximately 54% of the film is in the ferrimagnetic phase, such a large proportion of the ferrimagnetic phase is not been detected by XRD. One possible explanation may be that the antiferromagnetic phase is affected by the neighbouring ferrimagnetic and exhibit a small magnetic moment, hence effectively increased the ferrimagnetic volume.

Figure 7.26 indicates the magnetisation curves of Ta (5 nm)/Pt (35 nm)/Mn_3Ge (6-40 nm)/CoFe (3.3 nm)/Ta (5 nm) multilayer system grown at room temperature. Samples were field set at 500 K using the same procedure as Mn_3Ga for 90 minutes in a field of 20 kOe in order to saturate the ferromagnetic phase according to the York Protocol discussed in Chapter 5. The samples were then field cooled to 100 K in order to reduce thermal fluctuation. As shown in Figure 7.26, the change in AF thickness does not make much impact on its magnetic properties and there is no loop shift can be found. It may be due to the poor crystallisation of AF layer during the deposition. From the data extracted from Figure 7.26 the saturation magnetisation of the Mn_3Ge (6 nm)/$Co_{0.6}Fe_{0.4}$ (3.3 nm) sample was calculated to be (1020$\pm$10) emu/cm^3 which is dominated by the 3.3 nm $Co_{0.6}Fe_{0.4}$ layer, as the individual Mn_3Ge layer shows a small magnetisation of (54$\pm$5) emu/cm^3. By increasing the Mn_3Ge thickness, the saturation magnetisation of $Co_{0.6}Fe_{0.4}$ was found to decrease. For the 25- and 40-nm thick films, the saturation magnetisation from $Co_{0.6}Fe_{0.4}$ component dropped from (746$\pm$10) to (610$\pm$10) emu/cm^3. This decrease suggests that the Mn_3Ge/$Co_{0.6}Fe_{0.4}$ interface may suffer from intermixing by annealing introducing magnetically dead layers [137].

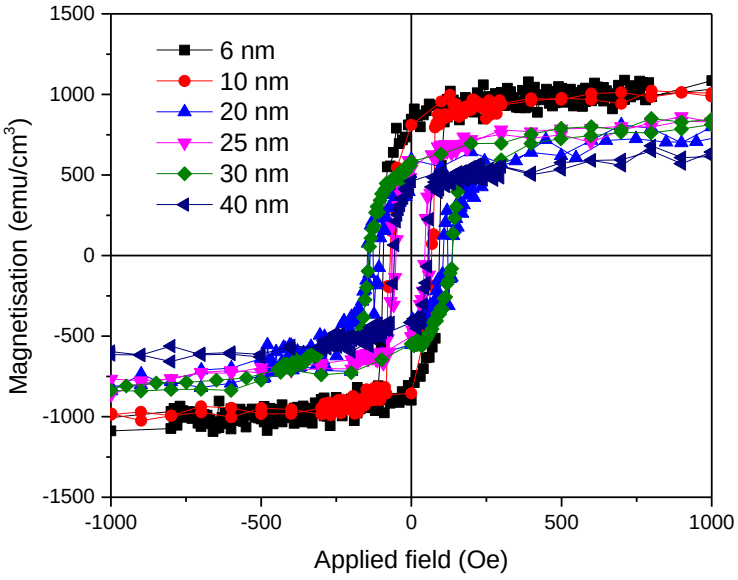

Figure 7.27 Magnetisation curves for the polycrystalline $Mn_3Ge/Co_{0.6}Fe_{0.4}$ (3.3 nm) with various AF thickness from 6 nm to 40 nm grown at room temperature and measured at 100 K.

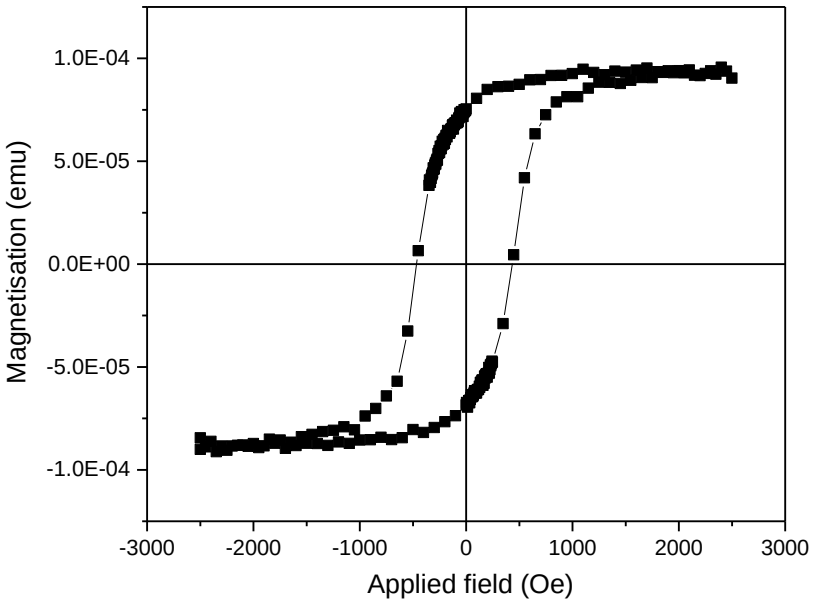

Figure 7.26 Magnetisation curves for the polycrystalline Mn_3Ge (100 nm)/$Co_{0.6}Fe_{0.4}$ (3.3 nm) film measured at 100 K.

In addition, the results for heated growth samples show a significant difference in coercivity compared with films grown at room temperature. As shown in Figure 7.27, the AF layer in the sample was heated to 500℃ during the deposition, the coercivity

of the film was increased to 466 Oe however the exchange bias cannot still be observed. The unobserved exchange bias from the film is due to pool interfacial exchange coupling between the F/AF layers. By improving the growth condition, it is possible to observe the exchange bias.

However, in the study conducted by C. Felser *et al*, [79] exchange bias is observed in the bulk hexagonal Mn_3Ge material. The exchange bias arised from the exchange interaction between the antiferromagnetic host and ferromagnetic clusters of Mn_3Ge materials. The maximum exchange bias observed is 620 Oe measured at 2 K and can still be seen at room temperature.

Due to the limited time to make further investigation on Mn_3Ge Heusler alloys, a systematic study of this material cannot be accomplished. It would be interesting to see samples with different Mn_3Ge layer thickness grown at elevating temperature. A list of samples growth plan is shown in Table 7.8.

Table 7.8 List of samples growth plan for future work.

Sample structure	**Growth Temperature (℃)**
Ta (5nm)/Pt (35 nm)/Mn_3Ge (10 nm)/CoFe (3.3 nm)/Ta (5 nm)	100-500
Ta (5nm)/Pt (35 nm)/Mn_3Ge (20 nm)/CoFe (3.3 nm)/Ta (5 nm)	100-500
Ta (5nm)/Pt (35 nm)/Mn_3Ge (30 nm)/CoFe (3.3 nm)/Ta (5 nm)	100-500
Ta (5nm)/Pt (35 nm)/Mn_3Ge (40 nm)/CoFe (3.3 nm)/Ta (5 nm)	100-500
Ta (5nm)/Pt (35 nm)/Mn_3Ge (50 nm)/CoFe (3.3 nm)/Ta (5 nm)	100-500
Ta (5nm)/Pt (35 nm)/Mn_3Ge (60 nm)/CoFe (3.3 nm)/Ta (5 nm)	100-500
Ta (5nm)/Pt (35 nm)/Mn_3Ge (70 nm)/CoFe (3.3 nm)/Ta (5 nm)	100-500

Chapter 8

8.1 Conclusion

The main objective of this work is to develop a new antiferromagnetic (AF) Heusler alloy (HA) which could replace IrMn applied in a variety of electronic and magnetic random-access memory. After comparing three Heusler alloys Mn_2VSi, Mn_3Ga and Mn_3Ge, the conclusion is drawn below.

Mn_2VSi sample used in this study is confirmed to be antiferromagnetic, where the corresponding exchange bias of (34 ± 5) Oe at 100 K is measured when a 3 nm ferromagnetic CoFe layer is deposited on top of Mn_2VSi layer. The film with 80 nm thick AF layer is found to be optimised for the growth at 723 K. Post-annealed samples provided large surface roughness and causing the diffusion at the interface between these layers, resulting in no exchange bias induced at the Mn_2VSi/CoFe interfaces. The blocking temperature of Mn_2VSi grown at 723 K is estimated to be below 100 K. These magnetic properties can be improved by substituting the constituent atoms with the other elements, suggesting a potential of Mn_2VSi to be used as an antiferromagnet in a spintronic device.

Mn_3Ge sample grown at 773 K shows a hexagonal $D0_{19}$ crystal structure Mn_3Ge with antiferromagnetic behaviour from θ -2 θ XRD scans. However, the magnetic measurement indicates that there is approximately 54% of the film is in the ferrimagnetic phase, such a large amount of the ferrimagnetic phase have not been detected by XRD. One possible explanation may be that the antiferromagnetic phase is affected by the neighbouring ferrimagnetic and exhibit a small magnetic moment, hence effectively increased the ferrimagnetic volume. Unfortunately no exchange bias is observed at the Mn_3Ge/CoFe interfaces due to the potential interfacial diffusion at high temperature.

Polycrystalline Mn_3Ga films grown by high target utilisation sputtering system are confirmed to crystallise in the $D0_{19}$ antiferromagnetic hexagonal structure. By coupling to a CoFe layer, it shows a large exchange-bias fields, of up to 430 ± 5 Oe at 120 K for a 3.3 nm ferromagnetic CoFe layer is deposited on the top of a 6 nm Mn_3Ga layer. The blocking temperature for 6-nm-thick Mn_3Ga is found to be 225 ± 5 K. The blocking temperature of Mn_3Ga decreases as the thickness of Mn_3Ga layer increases. The magnetocrystalline anisotropy of Mn_3Ga films was calculated to be $9 \times 10^4 J/m^3$. XPEEM measurement was also carried out, when probing the Mn L_3 edge, a clear

magnetic contrast which correlates exactly to that of the CoFe layer is observed, showing the presence of a spin-polarised Mn_3Ga layer at the interface. This indicates an uncompensated Mn_3Ga interface spin layer in these films which agrees with the large exchange-bias effects observed in this system. Furthermore the XAS spectra was taken at the Paul Scherrer Institut (PSI), the Mn_3Ga (6 nm)/CoFe (2 nm)/Al (2 nm) orbital and spin magnetic moments of Mn and Co was therefore estimated from XMCD spectra using the Sum Rules. The orbital and spin moments of Co are estimated to be $(0.299 \pm 0.005)\ \mu_B$ and $(1.268 \pm 0.005)\ \mu_B$ respectively. The total moment of Co is calculated to be $(1.57 \pm 0.01)\ \mu_B$ which agrees with the theoretical value of 1.60 μ_B[135]. The orbital and spin moments of Mn are also estimated to be $(0.270 \pm 0.005)\ \mu_B$ and $(0.320 \pm 0.005)\ \mu_B$ respectively. The total moment of Mn is calculated to be $(0.59 \pm 0.01)\ \mu_B$ which is within the literature magnetic moment of Mn (0.5-2.8) μ_B [63]. These estimated values represent those in the vicinity of Mn_3Ga/CoFe interface, confirming that the quality of these layers is not affected by their neighbouring layers.

Overall, from the experimental results observed in my study polycrystalline Mn_3Ga (due to its low cost for production and large exchange bias) is a more promising potential candidate to replace IrMn for application in spintronic devices. The value of the exchange bias and the blocking temperature can be further increased by substituting some of the Mn and/or Ga atoms with the other elements as reported by Nayak *et al.*[138], which warrants the possibility of Mn_3Ga being used in a future antiferromagnetic spintronic devices.

8.2 Future Work

There is a potential application for Mn-Ga thin films, exchange bias. Since the $D0_{19}$ hexagonal Mn_3Ga demonstrated a large exchange bias, it is becoming a promising candidate in spintronic devices. Exchange-bias is applied in giant magnetoresistance (GMR) and magnetic tunnel junction (MTJ) spin valve sensors and magnetic random access memories (MRAMs) to pin the magnetisation direction of the ferromagnetic layer. The strength of the exchange bias is significantly affected by the magnetic structure, anisotropy, crystalline order, and layer thickness of the antiferromagnet for a given system. In this work, large exchange bias for triangular antiferromagnetic hexagonal Mn_3Ga sample was observed at 100 K. The next step is to optimise the

growth condition and stack layer structure so that room temperature exchange bias can be observed. According to Nayak *et al.*[138], by doping Fe into Mn-Ga compounds the temperature dependence of the exchange bias for Mn-Fe-Ga compounds show a large exchange bias (more than 1 T) at 2 K which is still observable up to room temperature.

In addition, it is also possible to observe exchange bias up to room temperature in antiferromagnetic hexagonal Mn_3Ge Heulser alloys [79]. In this work, due to the limited research time no exchange bias was found in Mn_3Ge samples. However, according to Qian *et al*. [79], by high temperature annealing the bulk $Mn_{3.04}Ge_{0.96}$ material, it can be stabilised and shows a antiferromagnetic hexagonal crystal structure with a small fraction of ferromagnetic component with less than 0.1 μ_B. In this ordered phase exchange bias is observed up to room temperature.

Acronyms

Alternating gradient force magnetometer (AGFM)

Anisotropic magnetoresistance (AMR)

Charge-couple device (CCD)

Compensated ferrimagnetic (CF)

Complementary metal–oxide–semiconductor (CMOS)

Current in the plane (CIP)

Current perpendicular to the plane (CPP)

Density of states (DOS)

Direct current (DC)

Energy dispersive X-ray (EDX)

Face centred cubic (fcc)

Face centred tetragonal (fct)

Full width half maximum (FWHM)

Giant magnetoresistance (GMR)

Hard disk drives (HDDs)

Heusler alloy (HA)

High Target Utilisation Sputtering (HiTUS)

In plane magnetic tunnel junction (iMTJ)

Inorganic crystal structure database (ICSD)

Left circular polarisations (C-)

Magnetic random access memory (MRAM)

Magnetic tunnel junctions (MTJ)

Molecular beam epitaxy (MBE)

Paul Scherrer Institute (PSI)

Perpendicular magnetic tunnel junction (pMTJ)

Programmable Logic Controller (PLC)

Right circular polarisations (C+)

Ruderman-Kittel-Kasuya-Yoshida (RKKY)

Scanning electron microscope (SEM)

Spin dependent scattering (SDS)

Spin transfer torque (STT)

Surfaces/Interfaces: microscopy (SIM)

Synthetic antiferromagnet (SAF)

Transmission electron microscopy (TEM)

Tunnelling magnetoresistance (TMR)

Vibrating sample magnetometer (VSM)

X-ray absorption spectra (XAS)

X-ray diffraction (XRD)

X-ray magnetic circular dichroism (XMCD)

X-ray photoemission electron microscopy (XPEEM)

X-ray reflectivity (XRR)

List of Symbol

A	Area
AF	Antiferromagnetic
$A2$	Fully disordered Heusler structure
B_M	Magnetic flux density
$B2$	Partially disordered Heusler structure
C	Stiffness of the interfacial coupling between the AF and F layers
D	Grain diameter
D_m	Median grain diameter
d	Lattice spacing
E_{C}	Critical value of energy barrier
E_{int}	Interfacial energy
E_P	Field potential energy
E_k	Anisotropy energy
E_F	Fermi energy
F	Ferromagnetic
f_0	Attempt frequency
f_q	Uncoated resonant frequency
H	Applied field
H_{ex}	Exchange field
H_c	Coericivity
H_n	Nucleation field
H_k	Anisotropy field
J_{int}	Interfacial coupling constant
J_{c}	Write current density
K	Anisotropy constant
K_{AF}	Anisotropy constant of antiferromagnet
K_{F}	Anisotropy constant of ferromagnet
K_u	Material anisotropy

$L2_1$	Fully ordered full Heusler structure
M	Magnetisation
M_f	Change in mass due to the deposition
M_q	Original mass of the quartz crystal
M_r	Remnant magnetisation
M_s	Saturation magnetisation
M_t	Total spin magnetic moment
m	Magnetic moment
m_{spin}	Spin magnetic moment
$m_{orbital}$	Orbital magnetic moment
m_{total}	Total magnetic moment
N_c	Number of turns in Coil
N_q	Frequency constant of the quartz crystal
$n_{3\mathrm{d}}$	The electron occupation of the respective transition metal atom in 3d states
P_s	Saturation value of the order of the antiferromagnetic
R_{AP}	Resistance when spins antiparallel
R_P	Resistance when spins parallel
R^*	Refractive index of the view medium
R_z	Z-Factor of the film material
S	Magnetic viscosity coefficient
S_z	Half of m_{spin} in Hartree atomic unit
T	Temperature
T_C	Curie temperature
T_g	Growth temperature
T_N	Neel Temperature
T_B	Blocking temperature
T_{NA}	Non-thermal activation temperature
T_{act}	Thermal activation temperature
T_{set}	Setting temperature
$T_{measure}$	Measurement temperature

T_z	Expectation value of the magnetic dipole operator
t	Time
$t_{measure}$	Measurement time
t_{film}	Thickness of the film
t_{AF}	Antiferromagnet thickness
t_F	Ferromagnet thickness
V	Particle volume
V_c	Minimum grain volume
V_{set}	Maximum grain volume
V_{act}	Activation volume
Z_t	Number of valence electrons
θ_s	Angle between magnetisation and easy axis
λ_R	Wavelength of the radiation
λ_{x-ray}	X-ray wavelength.
ρ_f	Density of material
ρ_q	Density of the quartz
σ_{lnD}	Standard deviation of lnD
<V>	Median gran volume
Δf	Change in resonance frequency
a	Lattice constant
c	Lattice constant
emf	Electromagnetic force
h	Miller indices
k	Miller indices
	l Miller indices
f	Coated resonant frequency
β	Semi-angle of collection of the magnifying lens
δ	Minimum resolution per radian
ε	Induced electromagnetic force

θ	Angle between the incident and the scattering from the sample surface
μ	Mean of lnD
φ	Magnetic flux
τ	Relaxation time

Reference

[1] "We're Johnson Matthey | Johnson Matthey." [Online]. Available: https://matthey.com/. [Accessed: 10-Apr-2018].

[2] "PGM MARKET REPORT MAY 2016 Summary of Platinum SUPPLY & DEMAND IN 2015."

[3] W. Thomson, "On the Electro-Dynamic Qualities of Metals:--Effects of Magnetization on the Electric Conductivity of Nickel and of Iron," *Proc. R. Soc. London*, vol. 8, no. 0, pp. 546–550, Jan. 1856.

[4] T. McGuire and R. Potter, "Anisotropic magnetoresistance in ferromagnetic 3d alloys," *IEEE Trans. Magn.*, vol. 11, no. 4, pp. 1018–1038, Jul. 1975.

[5] H. H. Potter, "On the Change of Resistance of Nickel in a Magnetic Field," *Proc. R. Soc. A Math. Phys. Eng. Sci.*, vol. 132, no. 820, pp. 560–569, Aug. 1931.

[6] N. F. Mott, "The Electrical Conductivity of Transition Metals," *Proc. R. Soc. A Math. Phys. Eng. Sci.*, vol. 153, no. 880, pp. 699–717, Feb. 1936.

[7] A. Fert and I. A. Campbell, "Two-Current Conduction in Nickel," *Phys. Rev. Lett.*, vol. 21, no. 16, pp. 1190–1192, Oct. 1968.

[8] A. Fert and I. A. Campbell, "Electrical resistivity of ferromagnetic nickel and iron based alloys," *J Phys. F Met. Phys*, vol. 6, no. 5, 1976.

[9] S. M. Thompson, "The discovery, development and future of GMR: The Nobel Prize 2007," *J. Phys. D. Appl. Phys.*, vol. 41, no. 9, p. 93001, May 2008.

[10] J. F. Gregg, I. Petej, E. Jouguelet, and C. Dennis, "Spin electronics a review," *J. Phys. D. Appl. Phys.*, vol. 35, no. 18, pp. R121–R155, Sep. 2002.

[11] B. Dieny, "Giant magnetoresistance in spin-valve multilayers," *J. Magn. Magn. Mater.*, vol. 136, no. 3, pp. 335–359, Sep. 1994.

[12] B. Dieny *et al.*, "Magnetotransport properties of magnetically soft spin-valve structures (invited)," *J. Appl. Phys.*, vol. 69, no. 8, pp. 4774–4779, Apr. 1991.

[13] H. N. Fuke, K. Saito, Y. Kamiguchi, H. Iwasaki, and M. Sahashi, "Spin-valve giant magnetoresistive films with antiferromagnetic Ir-Mn layers," *J. Appl. Phys.*, vol. 81, no. 8, p. 4004, Jun. 1998.

[14] K. O'Grady, L. E. Fernandez-Outon, and G. Vallejo-Fernandez, "A new paradigm for exchange bias in polycrystalline thin films," *J. Magn. Magn. Mater.*, vol. 322, no. 8, pp. 883–899, Apr. 2010.

[15] A. Moser *et al.*, "Magnetic recording: advancing into the future," *J. Phys. D. Appl. Phys.*, vol. 35, no. 19, pp. R157–R167, Oct. 2002.

[16] L. Berger, "Emission of spin waves by a magnetic multilayer traversed by a current," *Phys. Rev. B*, vol. 54, no. 13, pp. 9353–9358, Oct. 1996.

[17] J. C. Slonczewski, "Current-driven excitation of magnetic multilayers," *J.*

Magn. Magn. Mater., vol. 159, no. 1–2, pp. L1–L7, Jun. 1996.

[18] J. A. Katine, F. J. Albert, R. A. Buhrman, E. B. Myers, and D. C. Ralph, "Current-Driven Magnetization Reversal and Spin-Wave Excitations in Co / Cu / Co Pillars," *Phys. Rev. Lett.*, vol. 84, no. 14, pp. 3149–3152, Apr. 2000.

[19] M. Julliere, "Tunneling between ferromagnetic films," *Phys. Lett. A*, vol. 54, no. 3, pp. 225–226, Sep. 1975.

[20] T. Miyazaki and N. Tezuka, "Giant magnetic tunneling effect in Fe/Al2O3/Fe junction," *J. Magn. Magn. Mater.*, vol. 139, no. 3, pp. L231–L234, Jan. 1995.

[21] J. S. Moodera, L. R. Kinder, T. M. Wong, and R. Meservey, "Large Magnetoresistance at Room Temperature in Ferromagnetic Thin Film Tunnel Junctions," *Phys. Rev. Lett.*, vol. 74, no. 16, pp. 3273–3276, Apr. 1995.

[22] D. J. Monsma and S. S. P. Parkin, "Spin polarization of tunneling current from ferromagnet/Al2O3 interfaces using copper-doped aluminum superconducting films," *Appl. Phys. Lett.*, vol. 77, no. 5, p. 720, Jul. 2000.

[23] W. H. Butler, X.-G. Zhang, T. C. Schulthess, and J. M. MacLaren, "Spin-dependent tunneling conductance of Fe | MgO | Fe sandwiches," *Phys. Rev. B*, vol. 63, no. 5, p. 54416, Jan. 2001.

[24] J. Mathon and A. Umerski, "Theory of tunneling magnetoresistance of an epitaxial Fe/MgO/Fe(001) junction," *Phys. Rev. B*, vol. 63, no. 22, p. 220403, May 2001.

[25] S. S. P. Parkin *et al.*, "Giant tunnelling magnetoresistance at room temperature with MgO (100) tunnel barriers," *Nat. Mater.*, vol. 3, no. 12, pp. 862–867, Dec. 2004.

[26] D. D. Djayaprawira *et al.*, "230% room-temperature magnetoresistance in CoFeB/MgO/CoFeB magnetic tunnel junctions," *Appl. Phys. Lett.*, vol. 86, no. 9, p. 92502, Feb. 2005.

[27] J. Hayakawa, S. Ikeda, F. Matsukura, H. Takahashi, and H. Ohno, "Dependence of Giant Tunnel Magnetoresistance of Sputtered CoFeB/MgO/CoFeB Magnetic Tunnel Junctions on MgO Barrier Thickness and Annealing Temperature," *Jpn. J. Appl. Phys.*, vol. 44, no. No. 19, pp. L587–L589, Apr. 2005.

[28] S. Ikeda *et al.*, "Tunnel magnetoresistance of 604% at 300K by suppression of Ta diffusion in CoFeB/MgO/CoFeB pseudo-spin-valves annealed at high temperature," *Appl. Phys. Lett.*, vol. 93, no. 8, p. 82508, Aug. 2008.

[29] M. Yoshikawa *et al.*, "Tunnel Magnetoresistance Over 100% in MgO-Based Magnetic Tunnel Junction Films With Perpendicular Magnetic L10-FePt Electrodes," *IEEE Trans. Magn.*, vol. 44, no. 11, pp. 2573–2576, Nov. 2008.

[30] K. Yakushiji *et al.*, "High Magnetoresistance Ratio and Low Resistance–Area Product in Magnetic Tunnel Junctions with Perpendicularly Magnetized Electrodes," *Appl. Phys. Express*, vol. 3, no. 5, p. 53003, May 2010.

[31] S. Ikeda *et al.*, "A perpendicular-anisotropy CoFeB--MgO magnetic tunnel junction," *Nat. Mater.*, vol. 9, 2010.

[32] Z. G. Zhi Gang Wang and Y. Nakamura, “Spin tunneling random access memory (STram),” *IEEE Trans. Magn.*, vol. 32, no. 5, pp. 4022–4024, 1996.

[33] S.-W. Chung *et al.*, “4Gbit density STT-MRAM using perpendicular MTJ realized with compact cell structure,” in *2016 IEEE International Electron Devices Meeting (IEDM)*, 2016, p. 27.1.1-27.1.4.

[34] S. Yakata *et al.*, “Enhancement of Thermal Stability Using Ferromagnetically Coupled Synthetic Free Layers in MgO-Based Magnetic Tunnel Junctions,” *IEEE Trans. Magn.*, vol. 46, no. 6, pp. 2232–2235, Jun. 2010.

[35] F. Heusler, W. Starck, and E. Haupt, “Verhandlungen der Deutschen Physikalischen Gesellschaft.,” *Verh. DPG*, vol. 5, p. 220, 1903.

[36] F. Heusler and F. Richarz, “Studien über magnetisierbare Manganlegierungen,” *Zeitschrift für Anorg. Chemie*, vol. 61, no. 1, pp. 265–279, Feb. 1909.

[37] T. Graf, C. Felser, and S. S. P. Parkin, “Simple rules for the understanding of Heusler compounds,” *Prog. Solid State Chem.*, vol. 39, no. 1, pp. 1–50, May 2011.

[38] S. Chadov, X. Qi, J. Kübler, G. H. Fecher, C. Felser, and S. C. Zhang, “Tunable multifunctional topological insulators in ternary Heusler compounds,” *Nat. Mater.*, vol. 9, no. 7, pp. 541–545, Jul. 2010.

[39] F. Casper, T. Graf, S. Chadov, B. Balke, and C. Felser, “Half-Heusler compounds: novel materials for energy and spintronic applications,” *Semicond. Sci. Technol.*, vol. 27, no. 6, p. 63001, Jun. 2012.

[40] G. E. Bacon and J. S. Plant, “Chemical ordering in Heusler alloys with the general formula A2BC or ABC,” *J. Phys. F Met. Phys.*, vol. 1, no. 4, p. 325, Jul. 1971.

[41] B. Balke, G. H. Fecher, J. Winterlik, and C. Felser, “Mn3Ga, a compensated ferrimagnet with high Curie temperature and low magnetic moment for spin torque transfer applications,” *Appl. Phys. Lett.*, vol. 90, no. 15, p. 152504, Apr. 2007.

[42] J. Winterlik *et al.*, “Structural, electronic, and magnetic properties of tetragonal $Mn_{3-x}Ga$: Experiments and first-principles calculations,” *Phys. Rev. B*, vol. 77, no. 5, p. 54406, Feb. 2008.

[43] J. C. Slater, “The Ferromagnetism of Nickel. II. Temperature Effects,” *Phys. Rev.*, vol. 49, no. 12, pp. 931–937, Jun. 1936.

[44] L. Pauling, “The Nature of the Interatomic Forces in Metals,” *Phys. Rev.*, vol. 54, no. 11, pp. 899–904, Dec. 1938.

[45] J. Kübler and J., “First principle theory of metallic magnetism,” *Phys. B+C*, vol. 127, no. 1–3, pp. 257–263, Dec. 1984.

[46] I. Galanakis, P. Mavropoulos, and P. H. Dederichs, “Electronic structure and Slater–Pauling behaviour in half-metallic Heusler alloys calculated from first principles,” *J. Phys. D. Appl. Phys.*, vol. 39, no. 5, pp. 765–775, Mar. 2006.

[47] X. Hu, “Half-Metallic Antiferromagnet as a Prospective Material for Spintronics,” *Adv. Mater.*, vol. 24, no. 2, pp. 294–298, Jan. 2012.

[48] I. Galanakis and P. Mavropoulos, “Spin-polarization and electronic properties of half-metallic Heusler alloys calculated from first principles,” *J. Phys. Condens. Matter*, vol. 19, no. 31, p. 315213, Aug. 2007.

[49] M. N. Baibich *et al.*, “Giant Magnetoresistance of (001)Fe/(001)Cr Magnetic Superlattices,” *Phys. Rev. Lett.*, vol. 61, no. 21, pp. 2472–2475, Nov. 1988.

[50] T. Jungwirth, X. Marti, P. Wadley, and J. Wunderlich, “Antiferromagnetic spintronics,” *Nat. Nanotechnol.*, vol. 11, no. 3, pp. 231–241, Mar. 2016.

[51] L. Néel, “Magnetism and the local molecular field,” *Nobel Lecture*, 1970. .

[52] W. H. Meiklejohn and C. P. Bean, “New Magnetic Anisotropy,” *Phys. Rev.*, vol. 102, no. 5, pp. 1413–1414, Jun. 1956.

[53] D. P. Oxley, R. S. Tebble, C. T. Slack, and K. C. Williams, “An Anti-ferromagnetic Heusler Alloy, Cu2MnSb,” *Nature*, vol. 194, no. 4827, pp. 465–465, May 1962.

[54] J. Kübler, A. R. William, and C. B. Sommers, “Formation and coupling of magnetic moments in Heusler alloys,” *Phys. Rev. B*, vol. 28, no. 4, pp. 1745–1755, Aug. 1983.

[55] K. U. Neumann, J. Crangle, R. K. Kremer, N. K. Zayer, and K. R. A. Ziebeck, “Magnetic order in Pd2TiIn: A new itinerant antiferromagnet?,” *J. Magn. Magn. Mater.*, vol. 127, no. 1–2, pp. 47–51, Oct. 1993.

[56] T. Moriya, “Physical Properties of Weakly and Nearly Ferro- and Antiferromagnetic Metals,” 1985, pp. 82–108.

[57] K. Ozdogan, I. Galanakis, E. Sasioglu, and B. Aktas, “Search for half-metallic ferrimagnetism in V-based Heusler alloys Mn2VZ (Z=Al, Ga, In, Si, Ge, Sn),” Dec. 2005.

[58] I. Galanakis, K. Ozdogan, E. Sasioglu, and B. Aktas, “Doping of Mn2VAl and Mn2VSi Heusler alloys as a route to half-metallic antiferromagnetism,” Jan. 2007.

[59] B. Deka, A. Srinivasan, R. K. Singh, B. S. D. C. S. Varaprasad, Y. K. Takahashi, and K. Hono, “Effect of Co substitution for Mn on spin polarization and magnetic properties of ferrimagnetic Mn2VAl,” *J. Alloys Compd.*, vol. 662, pp. 510–515, Mar. 2016.

[60] Tomoki, “Mn 2 VAl Heusler alloy thin films: appearance of antiferromagnetism and exchange bias in a layered structure with Fe,” *J. Phys. D Appl. Phys*, vol. 51, 2018.

[61] X. Y. Dong *et al.*, “Growth temperature controlled magnetism in molecular beam epitaxially grown Ni2MnAl Heusler alloy,” *J. Cryst. Growth*, vol. 254, no. 3–4, pp. 384–389, Jul. 2003.

[62] V. Sliwko, P. Mohn, and K. Schwarz, “The electronic and magnetic structures of alpha - and beta -manganese,” *J. Phys. Condens. Matter*, vol. 6, no. 32, pp.

6557–6564, Aug. 1994.

[63] J. M. D. Coey, *Magnetism and magnetic materials*. Cambridge University Press, 2009.

[64] S. Wurmehl, H. C. Kandpal, G. H. Fecher, and C. Felser, "Valence electron rules for prediction of half-metallic compensated-ferrimagnetic behaviour of Heusler compounds with complete spin polarization," *J. Phys. Condens. Matter*, vol. 18, no. 27, pp. 6171–6181, Jul. 2006.

[65] E. Krén and G. Kádár, "Neutron diffraction study of Mn3Ga," *Solid State Commun.*, vol. 8, no. 20, pp. 1653–1655, Oct. 1970.

[66] H. Niida, T. Hori, Y. Yamaguchi, and Y. Nakagawa, "Crystal distortion and weak ferromagnetism of $Mn_{3+\delta}Ga_{1-x}Ge_{x}$ alloys," *J. Appl. Phys.*, vol. 73, no. 10, pp. 5692–5694, May 1993.

[67] H. Kurt, K. Rode, H. Tokuc, P. Stamenov, M. Venkatesan, and J. M. D. Coey, "Exchange-biased magnetic tunnel junctions with antiferromagnetic ε-Mn_3Ga," *Appl. Phys. Lett.*, vol. 101, no. 23, p. 232402, Dec. 2012.

[68] L. Szunyogh, B. Lazarovits, L. Udvardi, J. Jackson, and U. Nowak, "Giant magnetic anisotropy of the bulk antiferromagnets IrMn and $IrMn_3$ from first principles," *Phys. Rev. B*, vol. 79, no. 2, p. 20403, Jan. 2009.

[69] D. Zhang *et al.*, "First-principles study of the structural stability of cubic, tetragonal and hexagonal phases in Mn_3Z (Z=Ga, Sn and Ge) Heusler compounds," *J. Phys. Condens. Matter*, vol. 25, no. 20, p. 206006, May 2013.

[70] J. Winterlik *et al.*, "Structural, electronic, and magnetic properties of tetragonal $Mn_{3-x}Ga$: Experiments and first-principles calculations," *Phys. Rev. B*, vol. 77, no. 5, p. 54406, Feb. 2008.

[71] H.-W. Bang *et al.*, "Perpendicular magnetic anisotropy properties of tetragonal Mn3Ga films under various deposition conditions," *Curr. Appl. Phys.*, vol. 16, no. 1, pp. 63–67, 2016.

[72] S. Khmelevskyi, A. V Ruban, and P. Mohn, "Magnetic ordering and exchange interactions in structural modifications of Mn 3 Ga alloys: Interplay of frustration, atomic order, and off-stoichiometry," *Phys. Rev. B*, vol. 93, no. 184404, 2016.

[73] S. Mizukami *et al.*, "Long-Lived Ultrafast Spin Precession in Manganese Alloys Films with a Large Perpendicular Magnetic Anisotropy," *Phys. Rev. Lett.*, vol. 106, no. 11, p. 117201, Mar. 2011.

[74] L. Zhu and J. Zhao, "Perpendicularly magnetized Mn x Ga films: promising materials for future spintronic devices, magnetic recording and permanent magnets," *Appl. Phys. A*, vol. 111, no. 2, pp. 379–387, May 2013.

[75] S. Mizukami *et al.*, "Composition dependence of magnetic properties in perpendicularly magnetized epitaxial thin films of Mn-Ga alloys," *Phys. Rev. B*, vol. 85, no. 1, p. 14416, Jan. 2012.

[76] H. Kurt, K. Rode, M. Venkatesan, P. Stamenov, and J. M. D. Coey, "High spin polarization in epitaxial films of ferrimagnetic Mn_3Ga," *Phys.*

Rev. B, vol. 83, no. 2, p. 20405, Jan. 2011.

[77] H. Kurt, K. Rode, M. Venkatesan, P. Stamenov, and J. M. D. Coey, "Mn3−xGa ($0 \leq x \leq 1$): Multifunctional thin film materials for spintronics and magnetic recording," *Phys. status solidi*, vol. 248, no. 10, pp. 2338–2344, Oct. 2011.

[78] G. T. Woods *et al.*, "Analysis of point-contact Andreev reflection spectra in spin polarization measurements," *Phys. Rev. B*, vol. 70, no. 5, p. 54416, Aug. 2004.

[79] J. F. Qian, A. K. Nayak, G. Kreiner, W. Schnelle, and C. Felser, "Exchange bias up to room temperature in antiferromagnetic hexagonal Mn_3Ge," *J. Phys. D. Appl. Phys.*, vol. 47, no. 30, p. 305001, Jul. 2014.

[80] H. Kurt *et al.*, "Magnetic and electronic properties of D022-Mn3Ge (001) films Magnetic and electronic properties of D0 22 -Mn 3 Ge (001) films," *Cit. Appl. Phys. Lett.*, vol. 101, 2012.

[81] F. Bloch, "Zur Theorie des Austauschproblems und der Remanenzerscheinung der Ferromagnetika," *Zeitschrift fr Phys.*, vol. 74, no. 5–6, pp. 295–335, May 1932.

[82] E. C. Stoner and E. P. Wohlfarth, "A Mechanism of Magnetic Hysteresis in Heterogeneous Alloys," *Philos. Trans. R. Soc. A Math. Phys. Eng. Sci.*, vol. 240, no. 826, pp. 599–642, May 1948.

[83] R. C. O'Handley, *Modern magnetic materials : principles and applications*. Wiley, 2000.

[84] W. Heisenberg, "Zur Theorie des Ferromagnetismus," *Zeitschrift fr Phys.*, vol. 49, no. 9–10, pp. 619–636, Sep. 1928.

[85] M. A. Ruderman and C. Kittel, "Indirect Exchange Coupling of Nuclear Magnetic Moments by Conduction Electrons," *Phys. Rev.*, vol. 96, no. 1, pp. 99–102, Oct. 1954.

[86] T. Kasuya, "A Theory of Metallic Ferro- and Antiferromagnetism on Zener's Model," *Prog. Theor. Phys.*, vol. 16, no. 1, pp. 45–57, Jul. 1956.

[87] K. Yosida, "Magnetic Properties of Cu-Mn Alloys," *Phys. Rev.*, vol. 106, no. 5, pp. 893–898, Jun. 1957.

[88] F. Radu and H. Zabel, "Exchange Bias Effect of Ferro-/Antiferromagnetic Heterostructures," in *Magnetic Heterostructures*, Berlin, Heidelberg: Springer Berlin Heidelberg, 2008, pp. 97–184.

[89] L. Néel, "Étude théorique du couplage ferro-antiferromagnétique dans les couches minces," *Ann. Phys. (Paris).*, vol. 14, no. 2, pp. 61–80, Apr. 1967.

[90] E. Fulcomer and S. H. Charap, "Thermal fluctuation aftereffect model for some systems with ferromagnetic-antiferromagnetic coupling," *J. Appl. Phys.*, vol. 43, no. 10, pp. 4190–4199, Oct. 1972.

[91] M. Grimsditch, A. Hoffmann, P. Vavassori, H. Shi, and D. Lederman, "Exchange-Induced Anisotropies at Ferromagnetic-Antiferromagnetic

Interfaces above and below the Néel Temperature," *Phys. Rev. Lett.*, vol. 90, no. 25, p. 257201, Jun. 2003.

[92] K. Nishioka, C. Hou, H. Fujiwara, and R. D. Metzger, "Grain size effect on ferro-antiferromagnetic coupling of NiFe/FeMn systems," *http://oasc12039.247realmedia.com/RealMedia/ads/click_lx.ads/www.aip.org/pt/adcenter/pdfcover_test/L-37/386502181/x01/AIP-PT/JAP_ArticleDL_092017/scilight717-1640x440.gif/434f71374e315a556e61414141774c75?x*, Jun. 1998.

[93] H. Xi, "Theoretical study of the blocking temperature in polycrystalline exchange biased bilayers," *J. Magn. Magn. Mater.*, vol. 288, pp. 66–73, Mar. 2005.

[94] W. F. Brown, "Thermal Fluctuations of a Single-Domain Particle," *Phys. Rev.*, vol. 130, no. 5, pp. 1677–1686, Jun. 1963.

[95] G. Vallejo-Fernandez, B. Kaeswurm, L. E. Fernandez-Outon, and K. O'Grady, "Effect of the Ferromagnetic Layer Thickness on the Blocking Temperature in IrMn/CoFe Exchange Couples," *IEEE Trans. Magn.*, vol. 44, no. 11, pp. 2835–2838, Nov. 2008.

[96] R. Street and J. C. Woolley, "A Comparison of Magnetic Viscosity in Isotropic and Anisotropic High Coercivity Alloys," *Proc. Phys. Soc. Sect. B*, vol. 69, no. 12, pp. 1189–1199, Dec. 1956.

[97] P. Gaunt, "Magnetic viscosity and thermal activation energy," *J. Appl. Phys.*, vol. 59, no. 12, pp. 4129–4132, Jun. 1986.

[98] G. Vallejo-Fernandez, N. P. Aley, L. E. Fernandez-Outon, and K. O 'grady, "Control of the setting process in CoFe/IrMn exchange bias systems," *J. Appl. Phys. Appl. Phys. Lett. J. Appl. Phys. Appl. Phys. Lett. J. Appl. Phys. J. Appl. Phys.*, vol. 104, no. 3097, pp. 152405–72409, 2008.

[99] G. Vallejo-Fernandez, L. E. Fernandez-Outon, and K. O'Grady, "Measurement of the anisotropy constant of antiferromagnets in metallic polycrystalline exchange biased systems," *Appl. Phys. Lett.*, vol. 91, no. 21, p. 212503, Nov. 2007.

[100] W. J. Gong, W. Liu, J. N. Feng, D. S. Kim, C. J. Choi, and Z. D. Zhang, "Effect of antiferromagnetic layer thickness on exchange bias, training effect, and magnetotransport properties in ferromagnetic/antiferromagnetic antidot arrays," *J. Appl. Phys.*, vol. 115, no. 13, p. 133909, Apr. 2014.

[101] Q.-F. Zhan, W. Zhang, and K. M. Krishnan, "Antiferromagnetic layer thickness dependence of the magnetization reversal in the epitaxial MnPd/Fe exchange bias system," *Phys. Rev. BJk*, vol. 8360, no. 94404, 2011.

[102] C. Gritsenko, I. Dzhun, N. Chechenin, G. Babaytsev, and V. Rodionova, "Dependence of the Exchange Bias on the Thickness of Antiferromagnetic Layer in the Trilayered NiFe/IrMn/NiFe Thin-films," *Phys. Procedia*, vol. 75, pp. 1066–1071, Jan. 2015.

[103] H. Sang, Y. W. Du, and C. L. Chien, "Exchange coupling in bilayer: Dependence on antiferromagnetic layer thickness Exchange coupling in Fe 50

Mn 50 /Ni 81 Fe 19 bilayer: Dependence on antiferromagnetic layer thickness," *J. Appl. Phys. J. Appl. Phys. J. Appl. Phys. J. Appl. Phys. J. Appl. Phys. Appl. Phys. Lett. J. Appl. Phys.*, vol. 851, no. 10, 1999.

[104] T. Ambrose and C. L. Chien, "Dependence of exchange coupling on antiferromagnetic layer thickness in NiFe/CoO bilayers," *J. Appl. Phys.*, vol. 83, no. 6822, 1998.

[105] G. Vallejo-Fernandez, L. E. Fernandez-Outon, and K. O'Grady, "Antiferromagnetic grain volume effects in metallic polycrystalline exchange bias systems," *J. Phys. D. Appl. Phys.*, vol. 41, no. 11, p. 112001, Jun. 2008.

[106] M. Kizilyalli, J. Corish, and A. R. Metselaar, "INTERNATIONAL UNION OF PURE AND APPLIED CHEMISTRY INORGANIC CHEMISTRY DIVISION DEFINITIONS OF TERMS FOR DIFFUSION IN THE SOLID STATE," *Pure Appl. Chem. Prof. A. V. Chadwick N. E. Walso Reca Prof. J.H. Choy (Korea Dr L. Tichy (Czech Repub. Dr P. Echequt (France Prof. O. L. Alves (Brazil Prof. F. M. Costa (Portugal Prof. B.G. Hyde (Australia*, vol. 71, no. 7, pp. 1307–1325, 1999.

[107] M. Vopsaroiu, G. V. Fernandez, M. J. Thwaites, J. Anguita, P. J. Grundy, and K. O'Grady, "Deposition of polycrystalline thin films with controlled grain size," *J. Phys. D. Appl. Phys.*, vol. 38, no. 3, pp. 490–496, Feb. 2005.

[108] M. Vopsaroiu, M. J. Thwaites, S. Rand, P. J. Grundy, and K. O 'grady, "Novel Sputtering Technology for Grain-Size Control," *IEEE Trans. Magn.*, vol. 40, no. 4, 2004.

[109] J. Sagar *et al.*, "Over 50% reduction in the formation energy of Co-based Heusler alloy films by two-dimensional crystallisation," *Appl. Phys. Lett.*, vol. 105, no. 3, p. 32401, Jul. 2014.

[110] J. Sagar, "Optimisation of Heusler Alloy Thin Films for Spintronic Devices," 2013.

[111] G. Sauerbrey, "Wagung dunner Schichten mit Schwingquarzen," *Angewandte Chemie : International Edition in English.,* 1957. [Online]. Available: http://openurl.york.ac.uk/primo_library/libweb/action/openurl?date=1957&aulast=Sauerbrey&issue=23&isSerivcesPage=true&spage=761&title=Angewandte+Chemie+international+edition&dscnt=2&auinit=G&atitle=Wagung+dunner+Schichten+mit+Schwingquarzen&url_ctx_fmt=nu. [Accessed: 31-Oct-2017].

[112] C. Lu and O. Lewis, "Investigation of film-thickness determination by oscillating quartz resonators with large mass load," *J. Appl. Phys.*, vol. 43, no. 11, pp. 4385–4390, Nov. 1972.

[113] "Automated Multipurpose X-ray Diffractometer Instruction Manual."

[114] "GenX - Home." [Online]. Available: http://genx.sourceforge.net/. [Accessed: 07-Nov-2017].

[115] D. B. (David B. Williams and C. B. Carter, *Transmission electron microscopy : a textbook for materials science*. Springer, 2009.

[116] K. O'Grady and A. Bradbury, "Particle size analysis in ferrofluids," *J. Magn.*

Magn. Mater., vol. 39, no. 1–2, pp. 91–94, Nov. 1983.

[117] G. Vallejo-Fernandez, N. P. Aley, J. N. Chapman, and K. O'Grady, "Measurement of the attempt frequency in antiferromagnets," *Appl. Phys. Lett.*, vol. 97, no. 22, p. 222505, Nov. 2010.

[118] S. Foner, "Versatile and Sensitive Vibrating-Sample Magnetometer*," *Rev. Sci. Instrum.*, vol. 30, no. 7, 1959.

[119] D. O. Smith, "Development of a Vibrating-Coil Magnetometer," *Rev. Sci. Instrum.*, vol. 27, no. 5, pp. 261–268, May 1956.

[120] K. Dwight, N. Menyuk, and D. Smith, "Further Development of the Vibrating-Coil Magnetometer," *J. Appl. Phys.*, vol. 29, no. 3, pp. 491–492, Mar. 1958.

[121] V. Koval, G. Viola, and Y. Tan, "Biasing Effects in Ferroic Materials," in *Ferroelectric Materials - Synthesis and Characterization*, InTech, 2015.

[122] B. D. Paccard, C. Schlenker, R. Montmory, and A. Yelon, "A New Property of Ferromagnetic-Antiferromagnetic Coupling')," *phys. stat. sol*, vol. 16, 1966.

[123] J. Stöhr, "Symmetry and Molecular Orbitals," in *NEXAFS Spectroscopy*, Springer Berlin Heidelberg, 1992, pp. 48–78.

[124] B. T. Thole, P. Carra, F. Sette, and G. van der Laan, "X-ray circular dichroism as a probe of orbital magnetization," *Phys. Rev. Lett.*, vol. 68, no. 12, pp. 1943–1946, Mar. 1992.

[125] P. Carra, B. T. Thole, M. Altarelli, and X. Wang, "X-ray circular dichroism and local magnetic fields," *Phys. Rev. Lett.*, vol. 70, no. 5, pp. 694–697, Feb. 1993.

[126] C. T. Chen *et al.*, "Experimental Confirmation of the X-Ray Magnetic Circular Dichroism Sum Rules for Iron and Cobalt," *Phys. Rev. Lett.*, vol. 75, no. 1, pp. 152–155, Jul. 1995.

[127] B. Cui, C. Song, Y. Y. Wang, W. S. Yan, F. Zeng, and F. Pan, "Tuning of uniaxial magnetic anisotropy in amorphous CoFeB films," *J. Phys. Condens. Matter*, vol. 25, no. 10, p. 106003, Mar. 2013.

[128] O. S. Whear, "The Growth and Crystallisation of Polycrystalline Heusler Alloy Thin Films," 2014.

[129] F. T. L. Muniz, M. A. R. Miranda, C. Morilla dos Santos, and J. M. Sasaki, "The Scherrer equation and the dynamical theory of X-ray diffraction," *Acta Crystallogr. Sect. A Found. Adv.*, vol. 72, no. 3, pp. 385–390, May 2016.

[130] H. Endo, A. Hirohata, J. Sagar, L. R. Fleet, T. Nakayama, and K. O'Grady, "Effect of grain size on exchange-biased Heusler alloys," *J. Phys. D. Appl. Phys.*, vol. 44, no. 34, p. 345003, Aug. 2011.

[131] C. Paduani *et al.*, "Ferromagnetism and antiferromagnetism in Ni2+x+yMn1−xAl1−y alloys," *Solid State Commun.*, vol. 141, no. 3, pp. 145–149, Jan. 2007.

[132] A. Hirohata *et al.*, "Structural and magnetic properties of epitaxial L21-structured Co2(Cr,Fe)Al films grown on GaAs(001) substrates," *J. Appl. Phys.*, vol. 97, no. 10, p. 103714, May 2005.

[133] A. Hirohata *et al.*, "Development of antiferromagnetic Heusler alloys for the replacement of iridium as a critically raw material Topical Review," *J. Phys. D. Appl. Phys.*, vol. 50, no. 50, p. aa88f4, 2017.

[134] C. N. T. Yu, A. J. Vick, N. Inami, K. Ono, W. Frost, and A. Hirohata, "Exchange bias induced at a $Co_2FeAl_{0.5}Si_{0.5}$/Cr interface," *J. Phys. D. Appl. Phys.*, vol. 50, no. 12, p. 125004, Mar. 2017.

[135] B. D. Cullity and C. D. Graham, *Introduction to magnetic materials*. IEEE/Wiley, 2009.

[136] A. Sugihara, K. Suzuki, S. Mizukami, and T. Miyazaki, "Structure and magnetic properties of tetragonal Heusler $D0_{22}$-Mn_3Ge compound epitaxial films with high perpendicular magnetic anisotropy," *J. Phys. D. Appl. Phys.*, vol. 48, no. 16, p. 164009, Apr. 2015.

[137] K. Oguz, P. Jivrajka, M. Venkatesan, G. Feng, and J. M. D. Coey, "Magnetic dead layers in sputtered Co40Fe40B20 films," *J. Appl. Phys.*, vol. 103, no. 7, p. 07B526, Apr. 2008.

[138] A. K. Nayak *et al.*, "Design of compensated ferrimagnetic Heusler alloys for giant tunable exchange bias," *Nat. Mater.*, vol. 14, no. 7, pp. 679–684, Mar. 2015.

[139] "Historical Iridium Prices and Price Chart - InvestmentMine." [Online]. Available: http://www.infomine.com/investment/metal-prices/iridium/all/. [Accessed: 10-Apr-2018].

[140] "Perpendicular Magnetic Recording Technology," 2007.

[141] H. Gu, X. Zhang, H. Wei, Y. Huang, S. Wei, and Z. Guo, "An overview of the magnetoresistance phenomenon in molecular systems," *Chem. Soc. Rev.*, vol. 42, no. 13, p. 5907, Jun. 2013.

[142] I. Galanakis, P. H. Dederichs, and N. Papanikolaou, "Slater-Pauling behavior and origin of the half-metallicity of the full-Heusler alloys," *Phys. Rev. B*, vol. 66, no. 17, p. 174429, Nov. 2002.

[143] "The RKKY Interaction." [Online]. Available: http://www.cmp.liv.ac.uk/frink/thesis/thesis/node71.html. [Accessed: 23-Nov-2017].

[144] S. P. Pati, D. Das-, and R. L. Stamps, "Mechanisms for exchange bias," *J. Phys. D Appl. Phys. Top. Rev. J. Phys. D Appl. Phys. J. Phys. D Appl. Phys*, vol. 33, no. 3300, pp. 247–268, 2000.

[145] "NIDetector.png (2941×735)." [Online]. Available: https://upload.wikimedia.org/wikipedia/commons/2/2d/NIDetector.png. [Accessed: 31-Oct-2017].